



CBPF - CENTRO BRASILEIRO DE PESQUISAS FÍSICAS

**Bohmian Rhapsody: From Quantum Harmonic Oscillator to the  
Unruh Effect**

MATHEUS MAIA DE ARAÚJO PAIXÃO

Supervisor: Nelson Pinto-Neto

RIO DE JANEIRO

2023

“BOHMIAN RHAPSODY: FROM QUANTUM HARMONIC OSCILLATOR  
TO THE UNRUH EFFECT”

**MATHEUS MAIA DE ARAÚJO PAIXÃO**

Tese de Doutorado em Física apresentada no  
Centro Brasileiro de Pesquisas Físicas do  
Ministério da Ciência Tecnologia e Inovação.  
Fazendo parte da banca examinadora os seguintes  
professores:

Documento assinado digitalmente  
 **NELSON PINTO NETO**  
Data: 18/11/2023 19:51:56-0300  
Verifique em <https://validar.iti.gov.br>

Nelson Pinto Neto - Orientador/CBPF

Documento assinado digitalmente  
 **ALVARO LUIS MARTINS DE ALMEIDA NOGUEIRA**  
Data: 16/11/2023 20:13:51-0300  
Verifique em <https://validar.iti.gov.br>

Álvaro Luis Martins de Almeida Nogueira – CEFET - RJ

Documento assinado digitalmente  
 **JULIO CESAR FABRIS**  
Data: 17/11/2023 12:12:37-0300  
Verifique em <https://validar.iti.gov.br>

Júlio César Fabris – UFES

Documento assinado digitalmente  
 **SANDRO DIAS PINTO VITENTI**  
Data: 18/11/2023 12:24:26-0300  
Verifique em <https://validar.iti.gov.br>

Sandro Dias Pinto Vitenti – UEL

Documento assinado digitalmente  
 **WELLISSON BARBOSA DE LIMA**  
Data: 18/11/2023 15:01:54-0300  
Verifique em <https://validar.iti.gov.br>

Wellisson Barbosa de Lima – UFRJ

Rio de Janeiro, 13 de novembro de 2023.

# Abstract

This work consist of two parts. In the first one, we will introduce the de Broglie-Bohm interpretation of quantum mechanics, giving examples of how to compute the called Bohmian trajectories and introducing a numerical method for this purpose. We plan to show the validity of the Ehrenfest theorem within this approach, analysing the driven quantum harmonic oscillator for different types of force and finding numerical solutions of the associated Schrödinger equation and the guidance equation for different sets of initial conditions. After we compute average properties over the trajectories, finding a classical trajectory law that depends on the quantum number of initial states considered. In this same part we demonstrate how this quantum-classical treatment of quantum systems can facilitate the study of complex subjects like quantum chaos, presenting the two-dimensional quantum harmonic oscillator and the coupled quantum anharmonic oscillator as examples.

In the second part, we investigate the behavior of the Minkowski ground state associated with a massless scalar field in Rindler space according to this interpretation. We use the Schrödinger picture to obtain the wave functional associated with the Minkowski vacuum and write it in terms of Rindler coordinates. Then we calculate the Bohmian averages of each energy component present in the Hamilton-Jacobi equation, reproducing the Unruh temperature, and analyzing their behavior in low and high temperature regimes. Finally, we find a set of Bohmian trajectories with astonishing properties and obtain the power spectrum. This study encompasses both the right-wedge problem and its extension to the left side as well.

**Key Words:** Bohmian mechanics, Unruh effect, Bohmian trajectories, quantum chaos

# Resumo

Este trabalho consiste em duas partes. Na primeira delas, introduziremos a interpretação de de Broglie-Bohm da mecânica quântica, dando exemplos de como calcular as chamadas trajetórias Bohmianas e introduzindo um método numérico para esse propósito. Planejamos mostrar a validade do teorema de Ehrenfest dentro dessa abordagem, analisando o oscilador harmônico quântico impulsionado por diferentes tipos de força e encontrando soluções numéricas da equação de Schrödinger associada e das equações guias para diferentes conjuntos de condições iniciais. Depois, calculamos propriedades médias ao longo das trajetórias, encontrando uma lei de trajetória clássica que depende do número quântico dos estados iniciais considerados. Nessa mesma parte, demonstramos como esse tratamento quântico-clássico de sistemas quânticos pode facilitar o estudo de assuntos complexos, como o caos quântico, apresentando o oscilador harmônico quântico bidimensional e o oscilador quântico anarmônico acoplado como exemplos.

Na segunda parte, investigamos o comportamento do estado fundamental de Minkowski associado a um campo escalar sem massa no espaço de Rindler de acordo com essa interpretação. Utilizamos a representação de Schrödinger para obter o funcional de onda associado ao vácuo de Minkowski e escrevemo-lo em termos de coordenadas de Rindler. Em seguida, calculamos as médias de Bohm de cada componente de energia presente na equação de Hamilton-Jacobi, reproduzindo a temperatura de Unruh e analisando seu comportamento em regimes de baixa e alta temperatura. Por fim, encontramos um conjunto de trajetórias de Bohm com propriedades surpreendentes e obtemos o espectro de potência. Este estudo abrange tanto o problema da cunha direita quanto sua extensão para o lado esquerdo também.

**Palavras-Chave:** Mecânica Bohmiana, efeito Unruh, trajetórias Bohmianas, caos quântico

# Acknowledgements

This work is dedicated to my family, my main strength and my support.

In the pursuit of knowledge, I embark on a long journey to unravel the mysteries of the cosmos. The breathtaking beauty of the universe, along with the elegant laws of physics governing it, has been the driving force behind this endeavor. In light of this, I extend my heartfelt gratitude to all those who have played a part in this expedition.

First and foremost, as any devout Christian, I would like to thank God for the gift of life, which, though brief, is eternal while it last.

I would like to thank my parents, Giovanni and Terezinha, along with my brother Diego, who were there and supported me throughout every moment of my journey. There are no words that can describe my eternal gratitude.

I am grateful to all the staff and friends at CBPF, where I spent most of these past years. I would like to mention my comrades at Diracstão along with its associates (Philippe, Wellisson, Picanço, Caio, Jão, Henrique, Bernard, Herus, Rodrigo, Piero, Matheus e Mírian) for their friendship and support. I would also like to thank Professors Tião and Helayel for the numerous courses they taught while I was at CBPF. Professor Tião, in particular, assisted us in a technical part of this work.

I wish to express my gratitude to my collaborators, Piero and Olesya. In particular, I would like to acknowledge my friend Henrique Santos Lima for his unwavering support and invaluable contributions to the majority of the research presented in the first part of this thesis.

I extend my deepest appreciation to my advisor, Nelson Pinto Neto, whose guidance, wisdom, and unwavering support have been instrumental throughout this research.

This journey has reaffirmed my belief in the profound beauty of science and the infinite possibilities it holds. As I conclude this chapter of my academic life, I am excited about the new horizons that await, and I look forward to continuing the exploration of the universe's secrets wherever I go.

As a final comment, I would like to congratulate Clube Atlético Mineiro for winning the Brazilian football championship title in 2021.

*The author thanks the Brazilian scientific support agencies, Fundação Coordenação de Aperfeiçoamento de Pessoal de Nível Superior (CAPES) and Conselho Nacional de Desenvolvimento Científico e Tecnológico (CNPq), for financial support.*

## About the Ph.D. thesis

This Ph.D. thesis is structured into two parts, both referring to the de Broglie-Bohm interpretation of quantum mechanics. The first part is introductory, where we present the main features of Bohmian mechanics and study fundamental aspects of quantum systems, like the Ehrenfest theorem [1]. With the aim to comprehend the classical-quantum behavior of the Bohmian averages, we developed a full numerical approach to obtain the Bohmian trajectories with high precision, allowing to address systems without an analytical solution of the Schrödinger equation. The corresponding online file is available at [2]. In this part we also explore the subject of quantum chaos within this perspective, showing the possibility to approach this problem in the same manner as classical chaos. We review the main mechanism that leads to chaos in two-dimensional systems and consider the case of a quantum anharmonic membrane [3], exhibiting the conditions under we have an exponential deviation of neighboring trajectories.

In a second moment, we delve into the central part of this thesis, focusing on the study of the Unruh effect from the perspective of de Broglie-Bohm theory [4]. We initiate this part by showing that the Bohmian mechanics concepts can be expanded to the quantum field theory with the help of the functional formalism. Employing this approach, we derive the wave functional associated with the Minkowski vacuum in Rindler variables and compute critical factors such as energy, field trajectories, and power spectra. We make this analysis considering both, the single-wedge and the two-wedges problem.

In addition to these works, I have also published a paper on Chern-Simons gravity in which we examine the Hamiltonian dynamics of a gravitational model related to the  $C_5$  gauge algebra, an extension of the  $(a)dS_5$  algebra [5].

1. M. M. A. Paixão and H. S. Lima, *Numerical validation of Ehrenfest theorem in a Bohmian perspective for non-conservative systems*, Eur. Phys. J. Plus 138, 549 (2023).
2. M. M. A. Paixão and H. S. Lima, Wolfram Community, *Numerical validation of Ehrenfest theorem in a Bohmian perspective for non-conservative systems*, 2023, available at: <https://community.wolfram.com/groups/-/m/t/2954181>.
3. H. S. Lima, M. M. A. Paixão, and C. Tsallis, *de Broglie-Bohm analysis of a non-linear membrane: From quantum to classical chaos*, arXiv:2308.07178 [quant-ph], submitted for publication.
4. M. M. A. Paixão, O. Galkina, N. Pinto-Neto, *Unruh effect under the de Broglie-Bohm perspective*, Phys. Rev. D 108, 083514 (2023).
5. M. M. A. Paixão and O. Piguet, *Five dimensional Chern-Simons gravity for the expanded (anti)-de Sitter gauge group  $C_5$* . Eur. Phys. J. C 80, 138 (2020).

# Contents

<b>I General aspects of de Broglie-Bohm interpretation of quantum mechanics</b>	<b>1</b>
<b>1 Introduction</b>	<b>2</b>
<b>2 de Broglie-Bohm interpretation of quantum mechanics</b>	<b>4</b>
2.1 The pilot wave interpretation . . . . .	5
2.2 Measurements . . . . .	8
2.3 The 1D quantum harmonic oscillator . . . . .	10
2.3.1 The ground state . . . . .	12
2.3.2 The linear superposition of the excited states . . . . .	12
2.4 The Ehrenfest theorem . . . . .	16
2.4.1 Numerical validation of Ehrenfest theorem for the quantum harmonic oscillator . . . . .	20
2.4.2 Forced Harmonic Oscillator . . . . .	22
2.5 The Duffing Oscillator . . . . .	28
<b>3 Quantum Chaos and Bohmian Mechanics</b>	<b>31</b>
3.1 Nodal-Point-X-Point-Complex and vortices . . . . .	34
3.2 Anisotropic two-dimensional harmonic oscillator . . . . .	37
3.3 The quantum anharmonic membrane . . . . .	49
<b>4 Concluding Remarks</b>	<b>59</b>
<b>II Quantum Field Theory and the Unruh effect: A Bohmian approach</b>	<b>62</b>
<b>5 Introduction</b>	<b>63</b>
<b>6 The Unruh effect from a Bohmian perspective</b>	<b>66</b>
6.1 The Unruh effect in the standard approach . . . . .	66

6.2	The Schrödinger representation and the scalar field wave functional in Minkowski space	75
6.3	The Rindler wave functional and its Bohmian interpretation in the right-wedge	82
6.3.1	The de Broglie-Bohm approach	87
6.3.2	Mean values and Unruh temperature	89
6.3.3	Low and high temperature regimes	91
6.3.4	Field Trajectories	95
6.3.5	Power Spectrum	97
6.4	The complete manifold problem	100
6.4.1	The vacuum wave functional for the two-wedge problem	101
6.4.2	Bohmian interpretation for the two wedges	105
6.4.3	Mean values for the extended geometry	109
6.4.4	Low and high acceleration regimes	111
6.4.5	Extended field trajectories	115
6.4.6	Power Spectrum for the complete manifold problem	116
<b>7</b>	<b>Concluding Remarks</b>	<b>119</b>

## Part I

# General aspects of de Broglie-Bohm interpretation of quantum mechanics

# Chapter 1

## Introduction

The de Broglie-Bohm interpretation of quantum mechanics [6, 7, 8], also known as the pilot wave interpretation, has received considerable attention in recent decades. Its broad applicability and ability to dialogue with diverse areas of physics have been key factors driving its extensive interest. The study of quantum systems through a quantum-classical treatment allowed the exploration of topics like quantum chaos [9, 10, 11, 12, 13], quantum synchronization [14], quantum information [15], quantum hydrodynamics [16, 17, 18], molecular dynamics [19], and strong-field ionization [20], among others.

This view of quantum mechanics is based on the Hamilton-Jacobi formulation for classical systems, differing from it by the presence of a nonlinear effective potential of quantum origin, called the quantum potential. In this formulation, the wave function, besides its probabilistic character, described here in terms of the initial conditions (which are unknown and impossible to determine), also exhibits a dynamic nature, guiding the trajectories of quantum particles throughout their evolution via the guidance equations. When the quantum potential approaches zero, Bohmian trajectories tend towards their classical analog, so that, in this limit, Bohmian mechanics reproduces classical mechanics. Since this approach provides the same predictions as the usual interpretation, it appears to be a promising way to study the transition between quantum to classical regimes. One of the challenges of this approach, however, is the numerical difficulty in obtaining quantum trajectories that are, at the same time, precise and stable, which has been mitigated in recent decades with the use of increasingly faster computers.

While it has been a well-known topic, Bohmian mechanics remains a fertile field of research with several fundamental questions still open. For example, it is not yet clear how to fully explain the standard model of particles solely from Bohmian mechanics. Additionally, there is no clear consensus on how to handle fermionic degrees of freedom within this interpretation. Furthermore, technological application problems, such as entanglement, have been relatively underexplored in this context, with Bohmian mechanics offering a promising alternative due to its non-local nature. Lastly, questions arise regarding the possibility of this formulation leading to experimental predictions different from

the usual interpretation, which may occur in systems outside the quantum equilibrium hypothesis. For these reasons, in this first part, we will focus on general aspects of the Bohmian approach in non-relativistic quantum systems.

This part is divided into two main chapters. Firstly, we will provide a brief introduction to the Bohmian interpretation of quantum mechanics, drawing a parallel with the classical Hamilton-Jacobi theory. Guided by Schrödinger's work [21], we are going to show how to interpret quantum phenomena from a classical point of view. To accomplish this, we will derive, from Schrödinger equation, a quantum version of the Hamilton-Jacobi equation, besides a continuity equation where the velocity field of the quantum particles is identified. To illustrate the concepts being discussed, we will solve the one-dimensional quantum harmonic oscillator as an example, presenting a fully numerical approach to obtain the Bohmian trajectories. Also, we will study the Ehrenfest theorem [22] for non-conservative systems, where we will consider the effect of a driven force in the Bohmian trajectories of the harmonic oscillator. Despite being an important theme in traditional quantum mechanics, is a poorly explored subject in de Broglie-Bohm literature. The validity of such theorem provides a good understanding of the conservation of the phase space for a given system. In the Bohmian perspective, the mean values are computed over a set of initial positions distributed according to  $|\Psi(x, t = 0)|^2$ . By consequence, if we consider a simple one-dimensional harmonic oscillator, classically the position is  $x(t) = A \cos(\omega t + \phi)$ . Since in the Bohmian mechanics the trajectories of the particles have objective reality, we expect that the mean value of a considerable number of possible trajectories associated to quantum harmonic oscillator will follow this sinusoidal form, with the amplitude and the phase to be determined. We will explore how the quantum forces affects the Bohmian trajectories, then compute the averages and connect the results with the correspondent classical equations of motion. In addition, we intend to analyse the quantum Duffing oscillator as well.

In a second moment, we will show how the de Broglie-Bohm interpretation of quantum mechanics can facilitate the study of quantum chaos. By solving the quantum equations of motion, we obtain the quantum analogues of classical trajectories, allowing us to adopt the same techniques used to study classical chaos in quantum systems. In this scenario, nonlinearities are a quite common feature, being an indispensable component for chaotic dynamics. With this purpose, we plan to study two examples: the anisotropic quantum harmonic oscillator, where we will explain the main mechanism responsible for the exponential deviation of neighboring trajectories by computing the Lyapunov exponent, and the coupled quantum anharmonic oscillator featuring cubic and quartic potentials, exploring the importance of the coupling potential in inducing chaotic behavior and investigate the effect of explicitly consider the Planck's constant in the numerical simulations. We will present a numerical approach to solve the two-dimensional time-dependent Schrödinger equation, yielding stable and precise solutions.

## Chapter 2

# de Broglie-Bohm interpretation of quantum mechanics

The de Broglie-Bohm interpretation (dBB) of quantum mechanics has its roots in the analogy between geometric optics and classical mechanics, given in terms of Hamilton-Jacobi's formulation [23, 24, 25, 26, 27, 28, 29]. The main object in the Schrödinger representation of quantum mechanics is the wave function  $\Psi$ , obtained from the time-dependent Schrödinger equation  $i\hbar\partial_t\Psi = \hat{\mathcal{H}}\Psi$ , with  $\hat{\mathcal{H}}$  the Hamiltonian operator derived from the classical Hamiltonian  $\mathcal{H}$ .

In his seminal work [21], Schrödinger introduces a quantum theory based in wave mechanics, where the classical mechanics is considered a particular case. According to him, the classical physics fails to describe quantum process in the same amount that geometric optics fails to describe wave-like phenomena such as interference and diffraction. Therefore, a more fundamental theory is necessary, one that encompasses geometric optics as a limiting case, or in our case, classical mechanics. In this context, the quantum mechanics is more fundamental than classic mechanics, with the last one obtained from the first in the limit when the distance between the energy levels is close to zero, which is equivalent to have a continuous energy spectrum.

Based on this assumption, Schrödinger suppose a wave process expressed by a function  $\Psi$  in the following form [29]

$$\Psi = e^{i\frac{S}{\hbar}} = e^{\frac{i}{\hbar}(W-Et)}, \quad (2.1)$$

where  $E$  is the energy and  $W = W(x, y, z)$  is a function related to the particle momentum through  $\vec{p} = \vec{\nabla}W = \sqrt{2m(E-V)}\hat{n}$ , with  $V$  the classical potential and  $\hat{n}$  the unitary vector orthogonal to the constant surface  $S = c$ . It is plausible to assume that, in order to represent a undulatory process,  $\Psi$  should obey the wave equation

$$\nabla^2\Psi = \frac{1}{v^2}\frac{\partial^2\Psi}{\partial t^2}, \quad (2.2)$$

with  $v$  the phase velocity. Since the phase  $S = W - Et$ , the infinitesimal distance  $ds$  between two consecutive surfaces with constant  $S$  (Figure 2.1) is such that  $dW = E dt$ , with  $dW = |\vec{\nabla}W| ds$ . Consequently,

$$v = \frac{ds}{dt} = \frac{E}{\sqrt{2m(E - V)}}. \quad (2.3)$$

Using this expression for the phase velocity and explicitly computing the time derivatives of  $\Psi$ , from the wave equation we gain the time-independent Schrödinger equation  $\hat{\mathcal{H}}\Psi = E\Psi$ , with the Hamiltonian operator  $\hat{\mathcal{H}} = -\frac{\hbar^2}{2m}\nabla^2 + V$ . Given that  $i\hbar\partial_t\Psi = E\Psi$ , we obtain from this heuristic argumentation that  $i\hbar\partial_t\Psi = \hat{\mathcal{H}}\Psi$ , which is just the Schrödinger equation.

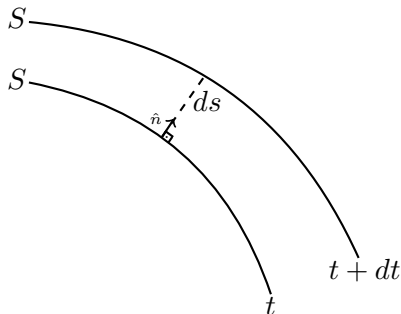


Figure 2.1: Infinitesimal distance  $ds$  between two consecutive wave fronts, which are assumed to have constant values of the parameter  $S = W - Et$ . The particle momentum is perpendicular to the surface  $S$ , along the direction defined by  $\hat{n}$ .

So, the quantum mechanics can be formulated based on the same classical framework used to describe the dynamics of objects at the macroscopic scale. However, there are crucial differences regarding both descriptions. First, we can cite that the results of experiments performed at submicroscopic levels are given in terms of probabilities, where the possible outcomes are the eigenvalues of Hermitian operators that represents the observables, obtained at rates proportional to the square modulus of the associated wave function representing the quantum system. There is no such analogue in classical mechanics. Concerning the mathematical structure, quantum mechanics is formulated in Hilbert space, while classical mechanics can be formulated in configuration space or in phase space, depending on the description being used.

## 2.1 The pilot wave interpretation

In the Bohmian interpretation of quantum mechanics, also known as pilot wave interpretation, the trajectories of the quantum particles have objective reality. The position at any time is guided by the wave function, which we assume can be written in the polar

form  $\Psi(\vec{x}, t) = R(\vec{x}, t)e^{iS(\vec{x}, t)/\hbar}$ . The velocity field is determined through the guidance equation

$$\frac{d\vec{x}}{dt} = \frac{\vec{\nabla}S}{m}, \quad (2.4)$$

where  $S(\vec{x}, t)$  is the phase of the wave function and  $m$  is the mass. Given a set of initial positions, we can integrate (2.4) to obtain the associated trajectories. Inserting  $\Psi(\vec{x}, t)$  into Schrödinger equation  $i\hbar\partial_t\Psi = \hat{H}\Psi$  and separating it into its real and imaginary parts, we arrive at two real equations. These are

$$\frac{\partial S}{\partial t} + \frac{(\vec{\nabla}S)^2}{2m} + V + Q = 0, \quad (2.5)$$

$$\frac{\partial R^2}{\partial t} + \vec{\nabla} \cdot \left( R^2 \frac{\vec{\nabla}S}{m} \right) = 0. \quad (2.6)$$

The first one can be seen as a Hamilton-Jacobi equation for  $S(\vec{x}, t)$ , where in addition to the classical potential  $V(\vec{x}, t)$  we have a supplementary quantum potential  $Q(\vec{x}, t)$  given by

$$Q(\vec{x}, t) = -\frac{\hbar^2}{2m} \frac{\nabla^2 R}{R}. \quad (2.7)$$

The second can be interpreted as a continuity equation, from which we can give a probabilistic interpretation for  $R(\vec{x}, t)^2$  as a probability density and understand  $\vec{\nabla}S/m$  as, in fact, a velocity field. As a consequence,  $(\vec{\nabla}S)^2/2m$  play the role of the kinetic energy, in such way that  $E = -\partial S/\partial t$  is the total energy of the system.

This view of quantum mechanics is completely different from Copenhagen interpretation (sometimes treated as usual interpretation). The first and most noticeable difference is the role of the wave function. In Bohmian mechanics  $\Psi$  admits a statistical interpretation because the possible initial positions are distributed according with  $|\Psi(\vec{x}, t = 0)|^2$ . Therefore, equation (2.6) guarantees that the position of the particles at any instant will be distributed with  $|\Psi(\vec{x}, t)|^2$ , according to Born's rule. Consequently, the statistical results are the same as in Copenhagen [30]. Furthermore,  $\Psi$  also has a dynamical meaning because it guides the particles through (2.4). Thus, the wave function is responsible for communicating to particles their interaction with other particles around them and with the environment.

This last statement is best formulated in terms of the quantum potential  $Q$ . Taking the time derivative of the guidance equation (2.4) and using (2.5), we find an acceleration equation:

$$m \frac{d^2\vec{x}}{dt^2} = -\vec{\nabla}V - \vec{\nabla}Q. \quad (2.8)$$

So, the quantum potential, expressed in terms of  $R(\vec{x}, t)$ , is responsible for a quantum force, supplementary to the classical one, that influences the particles in their trajectories. From equation (2.7), we can see that different initial conditions taken in the solution of the Schrödinger equation leads to different quantum potentials, and consequently, to different Bohmian trajectories. Also, eventual boundary conditions affect both the phase  $S(\vec{x}, t)$  and  $Q(\vec{x}, t)$ , implying that experimental conditions affects the quantum systems. Another aspect is the complexity of the initial conditions, in the sense that we can have trajectories quite different from their classical correspondents if we consider complicated initial wave functions. Additionally, near regions where the quantum potential is not well defined, it has a very fast spatial variation, implying in a significant amount of force that can attracts or repels particles of these points. In the limit when the quantum potential is negligible compared with the other quantities, we have a classical behavior.

These quantum-classical trajectories have two important properties worth mentioning. First, they do not intersect each other. Secondly, due the probabilistic interpretation of the wave function, the trajectories do not pass through points where  $|\Psi(\vec{x}, t)|^2 = 0$  (this is also true in nodal points where the phase  $S(\vec{x}, t)$  is not defined). The opposite is also true. In the vicinity of points where  $|\Psi(\vec{x}, t)|^2$  is maximum, the probability distribution of the particles is large, generating regions of agglomeration of positions. The existence of forbidden and most probably points, together to the first property, implies in an apparent squeezing of the trajectories, quite similar to hydrodynamics.

One last important feature of Bohmian mechanics is that is a non-local theory [31, 32]. For multiparticle states whose wave functional can be decomposed as the tensor products of individual states, that is,  $\Psi(\vec{x}_1, \dots, \vec{x}_N, t) = \Psi(\vec{x}_1, t) \otimes \dots \otimes \Psi(\vec{x}_N, t)$ , with  $N$  the total number of particles, the total phase and the quantum potential are the sum of its individual contributions. So,  $S(\vec{x}_1, \dots, \vec{x}_N, t) = \sum_{i=1}^N S_i(\vec{x}_i, t)$  and  $Q(\vec{x}_1, \dots, \vec{x}_N, t) = \sum_{i=1}^N Q_i(\vec{x}_i, t)$ . This means that each particle obeys a individual guidance equation

$$\frac{d\vec{x}_i}{dt} = \frac{\vec{\nabla}_i S_i(\vec{x}_i, t)}{m_i}, \quad i = 1, \dots, N. \quad (2.9)$$

On the other hand, for entangled states, the tensorial product decomposition hypothesis is not valid. Consequently, the phase cannot be expanded as before. Thus, the guidance equation for each particle is

$$\frac{d\vec{x}_i}{dt} = \frac{\vec{\nabla}_i S(\vec{x}_1, \dots, \vec{x}_N, t)}{m_i}, \quad i = 1, \dots, N, \quad (2.10)$$

which is fundamentally different from the previous one. Equation (2.9) states that each one of the quantum particles are guided by a phase that depends only on its individual coordinates. However, for the entangled state, the Bohmian trajectories of each particle depend on the coordinates of all the others. Therefore, we have a non-local theory, since

the dynamics of an individual particle depends on what happens in the regions where the other particles are.

## 2.2 Measurements

An important question to quantum mechanics as a whole is how to describe a measurement, which is a hard task that takes into account the knowledge of the quantum-classical frontier, since the quantum systems are observed by classical devices. One manner to avoid this controversial subject is to evoke the collapse postulate, which states that after a measurement process with an output that is an eigenvalue of some self-adjoint operator, the system collapses to the corresponding eigenstate, which is, indeed, the position of the orthodox interpretation. An effort to address the question of quantum measurements can be attributed to von Neumann [33, 34], yielding to important future developments, such as the decoherence phenomenon [35, 36, 37, 38].

For some quantum observable  $\hat{O}$  with eigenvalues  $O_i$  and eigenstates  $|O_i\rangle$ , we know that  $\hat{O}|O_i\rangle = O_i|O_i\rangle$ . Before an experimental process, when there is no interaction between the device and the measured system, the state corresponding to the quantum system+apparatus is  $|\Psi\rangle = |\psi_{QS}\rangle \otimes |\psi_A\rangle$ . The interaction introduces a correlation between these states in terms of the eigenstates of the position operator  $\hat{X}$  associated with the device pointer. As an example, consider that initially  $|\Psi^{\text{init}}\rangle = |s_i\rangle \otimes |x\rangle$ , with  $|s_i\rangle$  an eigenstate of the discrete operator  $\hat{S}$  and  $|x\rangle$  an eigenstate associated with  $\hat{X}$ . A measurement of  $\hat{S}$  do not change the correspondent eigenstate, but definitely changes the state of the apparatus in order to register  $s_i$ , being plausible to assume that  $|\Psi^{\text{init}}\rangle \rightarrow |\Psi^{\text{final}}\rangle = |s_i\rangle \otimes |x + \alpha s_i\rangle$ , with  $\alpha$  a real parameter.  $\square$

For a general state vector,  $|\psi_{QS}\rangle$  and  $|\psi_A\rangle$  are a linear combination of  $|s_i\rangle$  and  $|x\rangle$ , respectively, so that  $|\psi_{QS}\rangle = \sum_i c_i |s_i\rangle$  and  $|\psi_A\rangle = \int f(x) |x\rangle dx$ . Therefore, after a measurement,  $|\psi_A\rangle \rightarrow |\psi_A(s_i)\rangle \equiv \int f(x) |x + \alpha s_i\rangle dx = \int f(x - \alpha s_i) |x\rangle dx$ , which implies that  $|\Psi\rangle \rightarrow |\Psi^{\text{final}}\rangle = |\psi_{QS}\rangle \otimes |\psi_A(s_i)\rangle$ . If we assume that originally the pointer is centered in  $x = 0$ , what is possible to obtain with a Gaussian weight  $f(x) = \left(\frac{1}{\pi\Delta x^2}\right)^{1/4} \exp\left(-\frac{x^2}{2\Delta x^2}\right)$  such that the separation  $\Delta s$  of two adjacent values is much greater than the width  $\Delta x$  of the packet in order to obtain a readable result, which is mathematically expressed by  $\Delta s \gg \Delta x$ , than the product  $\langle \psi_A(s_i) | \psi_A(s_j) \rangle = e^{-\frac{\alpha^2}{4} \frac{(s_i - s_j)^2}{\Delta x^2}} \simeq \delta_{ij}$ . This shows that after a experimental procedure the final state of the device is a orthogonal superposition of states with the pointer centered in  $x = \alpha s_i$ , implying in a correlation between the apparatus and the observable eigenstates.

---

<sup>1</sup>This interaction can be expressed in terms of the Hamiltonian  $\hat{H} = -h(t)\hat{S} \otimes \hat{P}$ , where  $\hat{P}$  is the momentum operator of the pointer and  $h(t)$  is an impulsive function with weight such that this interaction overcomes all the others in a short period of time, being irrelevant for values of  $t$  not so distant from the maximum of  $h(t)$ .  $\square$

However, of all the possibilities contained in  $|\Psi^{final}\rangle$ , just one is manifested in the end of a measuring, namely the state correspondent to the observed value. This is a delicate issue that according to Copenhagen interpretation is explained by the collapse postulate, which claims that we just have access to the result of each measurement, not being explainable how such result is obtained. So, we are limited to statistical predictions. The Bohmian's view can handle this subject without using this new type of evolution for the wave function. Admitting that the degrees of freedom related to quantum system and to the apparatus have a real position defined in the phase space through the guidance equation (2.4), it is possible for us to explain how the devices record specific values of the observables without using the collapse of  $\Psi$ . Once the probability density is given by  $|\Psi|^2$ , the pointer variable  $x$ , which has a non-trivial correlation with the quantum system, must, in fact, be (and not to be found) in one of the packets, staying there thereafter, since the region between two consecutive packets has an almost zero probability [7]. To determine exactly what will be the branch of the wave function, we need to have access to the initial conditions, that is, we need to know the initial position (and consequently the momenta) of all the degrees of freedom. The evolution of the Bohmian trajectories will say to us in what branch we will end up. Unfortunately, we are not able to know this information with precision, but just the initial distribution given by the Born's rule. In this sense, the positions and momenta are considered as hidden variables in this interpretation, implying that the experimental results are given in terms of statistical descriptions involving these (unknown) variables.

Indeed, the probability  $\mathcal{P}_i$  that an interaction leads to a specific branch  $i$  is  $|c_i|^2$ . If we consider the wave function in coordinate representation, the associated probability is given by the integral of  $|\Psi^{final}|^2$  over the configuration space, with  $\Psi^{final} = (\langle x| \otimes \langle y|) (|\psi_{QS}\rangle \otimes |\psi_A(s_i)\rangle) = \psi_{QS}(y)\psi_A^i(x)$ , where for simplicity we assume the quantum system as a single particle of position  $y$  and general wave function  $\psi_{QS}(y) = \sum_j c_j \psi_j(y)$ . Here,  $\psi_j(y)$  are the eigenvectors related to  $s_j$ . For the apparatus, we have  $\psi_A^i(x) = \langle x| \int f(x' - \alpha s_i) |x'\rangle dx' = f(x - \alpha s_i)$ . So, the value of  $\mathcal{P}_i$  is given as follows:

$$\begin{aligned}
\mathcal{P}_i &= \int |\Psi^{final}|^2 dx dy \approx \int \sum_j |c_j|^2 |\psi_j(y)|^2 |f(x - \alpha s_j)|^2 dx dy \\
&\approx |c_i|^2 \int |\psi_i(y)|^2 dy \int |f(x - \alpha s_i)|^2 dx \\
&= |c_i|^2.
\end{aligned} \tag{2.11}$$

In this proof we made two assumptions. In the first approximation, we consider that all non-diagonal terms responsible for interference are negligible and do not contribute to  $\mathcal{P}_i$  [39], while in the second line we use the fact that given an initial condition, the only branch that has a non-null probability at  $(x, y)$  in the configuration space is the one

associated with the eigenvalue  $s_i$ . Therefore, according to this interpretation, an initial configuration will lead the system to a specific branch, without the necessity to invoke the collapse postulate. There is, however, an apparent collapse in Bohmian mechanics, as the other ramifications are considered empty waves, inaccessible to the representative particle. In fact, these waves will not be detected by any device [39].

In this sense, the Bohmian formulation of quantum mechanics allows us to understand how the outcome of a measurement depends not only on the state of the system being measured, but also on the context of other experiments being performed. While the position of particles may be independent of context, other quantities are obtained from the wave function, which has a clear dependence on the measurement-related context. For example, measuring the momentum of a particle changes the wave function phase, and consequently changes the momentum value due to the guidance equation (2.4). This issue is deeply connected with the entanglement between the quantum system and the apparatus. When an experiment is performed, it introduces a correlation between the quantum system and the experimental device, changing the wave function. For this reason the trajectory in the configuration space will be different of the trajectory of the unmeasured system, potentially leading to different experimental outcomes.

### 2.3 The 1D quantum harmonic oscillator

In order to illustrate some of the features explained so far, we will study the one-dimensional quantum harmonic oscillator from a Bohmian perspective since it is a very well-known system. So, in order to make the dBB interpretation a plausible theory, a thorough understanding of this system is essential. However, due to the non-linear aspect of the quantum potential, the trajectories do not have, in general, an analytical solution. Therefore, we choose to follow a complete numerical approach, including the solution of the Schrödinger equation.

The first step is to solve the Schrödinger equation  $i\hbar\partial_t\Psi = \hat{\mathcal{H}}\Psi$ , with the Hamiltonian  $\hat{\mathcal{H}}$  given by  $\hat{\mathcal{H}} = \frac{\hat{p}^2}{2m} + \frac{1}{2}m\omega^2\hat{x}^2$ , being  $\hat{x}$  and  $\hat{p}$  the position and momentum operators respectively. In order to make the numerical analysis we replace temporal and spatial variables by dimensionless ones, that is,  $t \rightarrow \omega t$  and  $x \rightarrow x/\sqrt{\hbar/m\omega}$ . Writing the wave function in the Cartesian form  $\Psi(x, t) = \Phi_r(x, t) + i\Phi_i(x, t)$  and inserting into Schrödinger equation, we have two coupled dimensionless equations

$$-\frac{1}{2}\frac{\partial^2\Phi_r}{\partial x^2} + \frac{1}{2}x^2\Phi_r = -\frac{\partial\Phi_i}{\partial t}, \quad (2.12)$$

$$-\frac{1}{2}\frac{\partial^2\Phi_i}{\partial x^2} + \frac{1}{2}x^2\Phi_i = \frac{\partial\Phi_r}{\partial t}. \quad (2.13)$$

The radial part of the wave function can be expressed as  $R(x, t) = \sqrt{\Phi_r^2 + \Phi_i^2}$ , while the

phase is  $S(x, t) = \arctan(\Phi_i/\Phi_r)$ .

To solve this system we use the Method of Lines [40], considering the Tensor-Product Grid technique to make the spatial discretization<sup>2</sup>[41]. We consider Dirichlet boundary conditions for  $\Psi$ , demanding that  $\Psi(-L, t) = \Psi(L, t) = 0$ , where we take  $L = 10$ . Also we consider the maximum time  $t_{max} = 100$ , which is good enough to evaluate averages and achieve good precision in our problem. As an initial condition we set  $\Psi(x, 0)$  as a combination of the eigenstates of the harmonic oscillator properly normalized, namely

$$\Psi(x, 0) = \frac{1}{\sqrt{n+1}} \sum_{\alpha=0}^n \psi_{\alpha}(x), \quad (2.14)$$

with  $\psi_{\alpha}(x)$  such that

$$\psi_{\alpha}(x) = \frac{1}{\sqrt{2^{\alpha}\alpha!}} \pi^{-1/4} H_{\alpha}(x) e^{-\frac{x^2}{2}}, \quad (2.15)$$

where  $H_{\alpha}(x)$  are the Hermite polynomials of order  $\alpha$ . Note that each initial wave function  $\Psi(x, 0)$  gives a different phase  $S(x, t)$  and, consequently, we have different associated trajectories.

In a second stage we integrate the guidance equation (2.4), which in terms of the dimensionless variables is

$$x(t)\hbar = \int_0^t \frac{\partial S(x, t')}{\partial x} dt'. \quad (2.16)$$

So, the quantum trajectories are given in unities of  $\hbar$ , which we can assume as 1. To perform this integration we use the Explicit Runge-Kutta method of order 8, with a fixed step size of 0.01. For the initial positions we set a total of 400 points randomly distributed according to  $|\Psi(x, 0)|^2$ , each one leading to a different trajectory.

A common alternative to the method presented here is to consider a semi-analytical approach. For systems with an analytical solution for the Schrödinger equation, we can skip step one. This is, in fact, the case of the harmonic oscillator. However, we just have an analytical wave function for a few number of examples which, in general, are too simple to describe real physical systems. Therefore, an advantage of obtaining the wave function numerically is that it allow us to solve more complex cases, since we do not have knowledge of exact expressions for  $\Psi(x, t)$ . However, the pure numerical approach of Bohmian trajectories has three sources of error: the first and most important is the solution of the Schrödinger equation. As the time evolves, the errors associated to the boundary effects starts to interfere with the wave function and becomes more and more

---

<sup>2</sup>The Method of Lines is a method of solving PDEs consisting in discretize all the dimensions except by one (typically the time), turning the problem into a system of ODEs, where we can apply the numerical techniques available.

relevant. We can control this error demanding that the integral of  $|\Psi(x, t)|^2$  inside the box must be 1 with an error of  $\sim 10^{-3}$ , what can be done choosing appropriately the size of the grid and the degree of the difference order. Grids of size 100 works well when we consider the sum of few eigenstates, while is necessary use a size of 400 for larger numbers. The degree of the difference taken was from 4 to 6.

The second source is the integration (2.16). Even though it is easy to control using an adequate stepsize, a complex expression for the phase can demand a big computational time, making hardy work with a large number of trajectories. This is intimately connected with the third cause of error, that is the random distribution of the initial positions according to  $|\Psi(x, 0)|^2$ . The more complicated the initial wave function, the more difficult is to obtain a histogram of initial conditions that reproduces this distribution. So, in order to minimize this error we need to consider a set with a larger number of initial points, implicating in compute more trajectories. Since one of our objectives is to calculate the dBB average of the  $x(t)$  over time, we need set a good initial distribution that approximately matches with  $|\Psi(x, 0)|^2$ . From a sample of 400 initial positions, we construct a smooth histogram and visually compare with  $|\Psi(x, 0)|^2$ . If it is not close enough, we randomly take a new set of starting positions until we get one that matches with the wave function distribution. In this way, we guarantee a good initial set of points without having to calculate a high number of trajectories.

### 2.3.1 The ground state

Let us consider the special case where the initial wave function is the ground state  $\Psi(x, 0) = \pi^{-1/4} e^{-x^2/2}$ . Since we start with an eigenstate of the harmonic oscillator, the wave function phase will not depend on  $x$ . As a consequence,  $\vec{\nabla}S = 0$ , implying in a null velocity field. Therefore, the trajectories are static, with  $x(t) = x(0)$ . This fact can be explained by examining the effective potential  $V_{eff} = V + Q$ . The quantum potential (2.7) is  $Q = (1 - x^2)/2$ , canceling the spatial contribution of  $V$ . As a result, the classical and quantum forces counterbalance each other, maintaining the particles in equilibrium. Thus, if a particle starts at a given position, it will remain there. While we demonstrate this phenomenon for the ground state of the quantum harmonic oscillator, it holds true in general within Bohmian mechanics. Initial wave functions that are eigenstates of any considered system will yield static trajectories.

### 2.3.2 The linear superposition of the excited states

Linear superpositions of excited states are quite interesting since they present more complicated trajectories. For example, for an initial condition that is a superposition of eigenstates of the harmonic oscillator, the general solution of the Schrödinger equation depends on time. From the usual quantum mechanics textbooks [42, 43, 44], we know

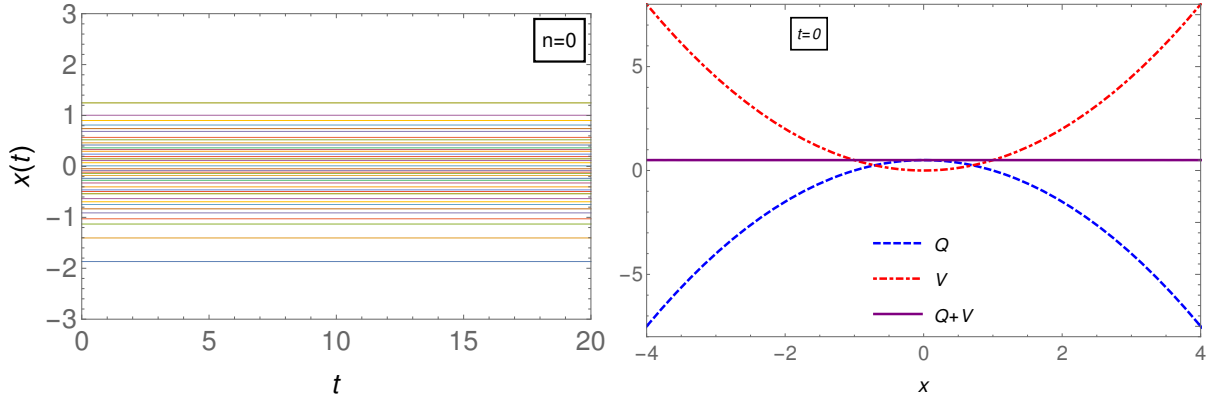


Figure 2.2: In the left, the bohmian trajectories for the quantum harmonic oscillator with  $\Psi(x, 0) = \psi_0(x)$ . In the right, the quantum and classical potential. The effective potential is constant, so its derivatives and, by consequence, the total force is null. Since neither  $Q$  and  $V$  depends on time, the quantum trajectories are static.

that an initial condition of the type  $\Psi(x, 0) = \frac{1}{\sqrt{n+1}}(\psi_0(x) + \psi_1(x) + \dots + \psi_n(x))$ , with the same weight for each individual contribution, leads to

$$\Psi(x, t) = \frac{1}{\sqrt{n+1}}(\psi_0(x)e^{-i\frac{E_0}{\hbar}t} + \psi_1(x)e^{-i\frac{E_1}{\hbar}t} + \dots + \psi_n(x)e^{-i\frac{E_n}{\hbar}t}), \quad (2.17)$$

with  $E_\alpha = (\alpha + \frac{1}{2}) \hbar\omega$  the energy of each eigenstate. In the polar form, this expression becomes

$$\Psi(x, t) = \frac{1}{\sqrt{n+1}} \left\{ \left( \sum_{\alpha=0}^n R_\alpha \cos S_\alpha \right)^2 + \left( \sum_{\alpha=0}^n R_\alpha \sin S_\alpha \right)^2 \right\}^{1/2} \times \exp \left\{ i \tan^{-1} \left( \frac{\sum_{\alpha=0}^n R_\alpha \sin S_\alpha}{\sum_{\alpha=0}^n R_\alpha \cos S_\alpha} \right) \right\}, \quad (2.18)$$

where  $R_\alpha(x) = \psi_\alpha(x)$  and  $S_\alpha(t) = -(\alpha + \frac{1}{2}) \omega t$  are the radial part and the phase of each mode. Therefore, for the total wave function we have that

$$R(x, t) = \frac{1}{\sqrt{n+1}} \left\{ \left( \sum_{\alpha=0}^n R_\alpha \cos S_\alpha \right)^2 + \left( \sum_{\alpha=0}^n R_\alpha \sin S_\alpha \right)^2 \right\}^{1/2} \quad (2.19)$$

and

$$S(x, t) = \tan^{-1} \left( \frac{\sum_{\alpha=0}^n R_\alpha \sin S_\alpha}{\sum_{\alpha=0}^n R_\alpha \cos S_\alpha} \right). \quad (2.20)$$

From these expressions, we can see that despite being a simple case, we will have complicated Bohmian trajectories, especially for larger values of  $n$ . Because of that, we

do not have an analytical solution for the Bohmian trajectories (2.16). Also, it is evident from (2.7) and (2.19) the non-linear character of the quantum potential.

**n=1**

Let us consider the case  $\Psi(x, 0) = \frac{1}{\sqrt{2}}(\psi_0(x) + \psi_1(x))$ . From the numerical solution of the equations (2.12) and (2.13), we obtain  $|\Psi(x, t)|^2 = R^2(x, t)$ . Since the initial state is not an eigenstate of the harmonic oscillator, but a combination of the ground state and the first excited state, the probability density, which in de Broglie-Bohm interpretation is associated with the probability of a particle actually be in a given position, changes with time.

The numerical solution of the system (2.12), (2.13) and (2.16) is represented in figure 2.3. The initial distribution is slightly inclined to the positive direction, near  $x = 1$ , because the choice of the initial wave function. As the time evolves, the trajectories tend towards the center until they reach the negative semi-axis up to values close to -1, staying there for a while until they cross the origin again and come back near to 1, completing the cycle.

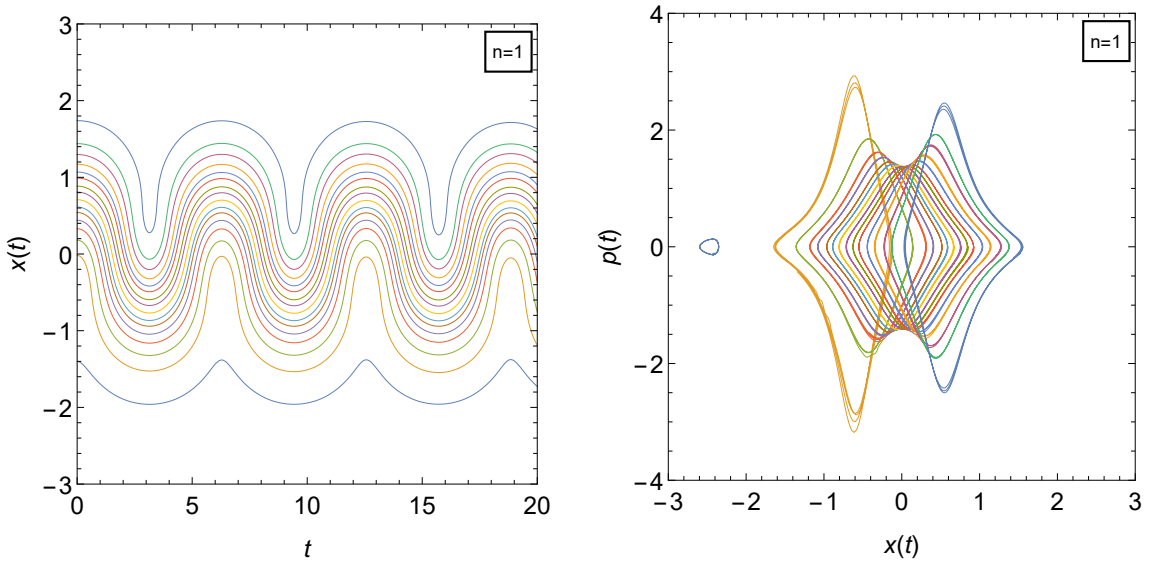


Figure 2.3: In the left, the Bohmian trajectories for the quantum harmonic oscillator with  $\Psi(x, 0) = \frac{1}{\sqrt{2}}(\psi_0(x) + \psi_1(x))$ . In the right, the phase space. Both, the positions in function of time and the phase space are completely different of the classical harmonic oscillator. This difference is due the quantum potential  $Q$ , which is relevant in this case.

As we said, this behavior can be explained through the graph of  $|\Psi(x, t)|^2$ . For  $t = 0$ , the major part of  $|\Psi|^2$  is in the positive semi-axis, with peak around 1. The evolution of the wave function makes the distribution go to the left, arriving a point of symmetry at  $t = \pi/2$ . For  $t = \pi$  we have the same initial distribution, but mirrored in relation to the vertical axis. Since we are dealing with a periodic system we eventually returns to the

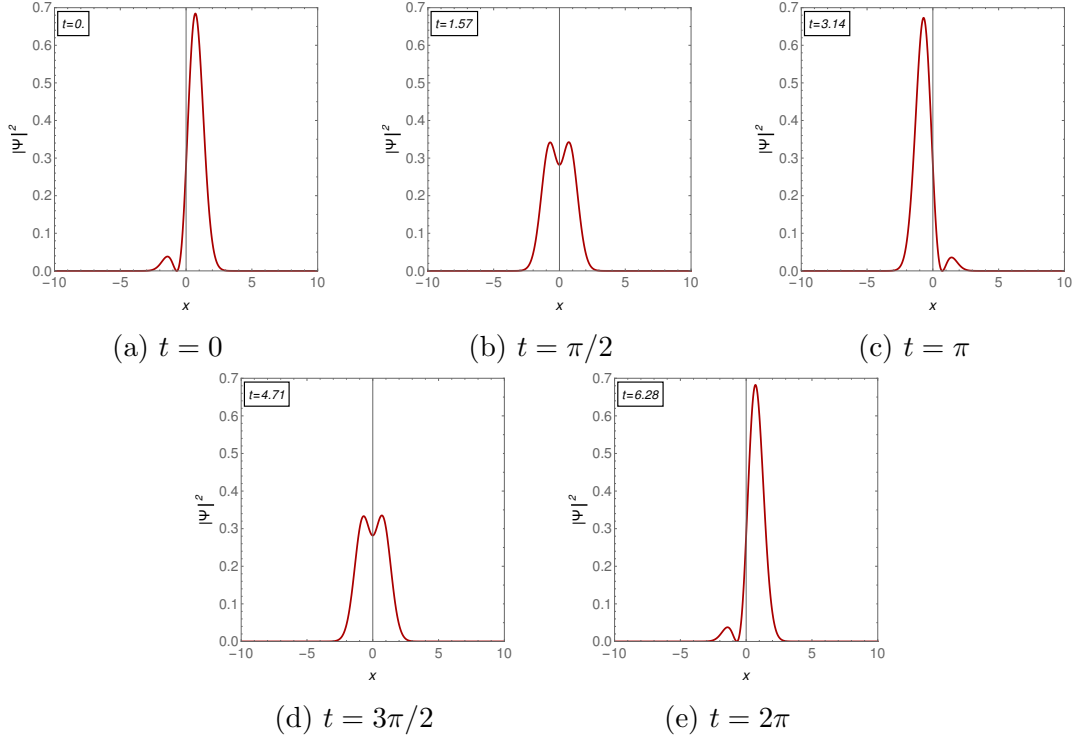


Figure 2.4: The evolution of  $|\Psi(x, t)|^2$  over time for  $n = 1$ . Initially the trajectories are concentrate in the positive part of the x-axis, where is the major contribution of  $|\Psi|^2$ . The temporal evolution shows that the probability distribution oscillates around the origin. This oscillation is translated in the trajectories oscillations in figure [2.3](#).

initial probability density, from where another cycle begins again (Fig. [2.4](#)). The reason behind this is the effective potential. Initially,  $V_{eff}$  has a positive inclination everywhere. So, the effective force that acts in all the particles is negative, causing them to move in to negative x direction. As a consequence,  $|\Psi|^2$  will follow the trajectories density. This force is stronger near the singularity (Fig. [2.5](#)), where  $V_{eff}$  varies very quickly. As the time passes, this singularly shrinks and becomes a small slope. At  $t = \pi/2$ , the effective potential is symmetric in relation to the x-axis. The particles on the right feel a negative force that accelerates them, until they eventually cross the origin, where the effective force becomes positive, slowing the particles down. Since the trajectories do not intersect each other, this generates an apparent squeezing of the trajectories near the origin. The slope grows until become a singularity at  $t = \pi$ , where the  $V_{eff}$  is negative everywhere, making  $|\Psi(x, t)|^2$  to return to its initial state at  $t = 2\pi$ .

**n = 2, 3, 4, ...**

The same analysis we made for  $n = 0$  and  $n = 1$  is valid when we consider more excited states. For this reason, we will content ourselves in just showing the numerical results of the trajectories and their respective phase spaces.

As we can see from Figure [2.6](#), the trajectories become more complicated as we increase

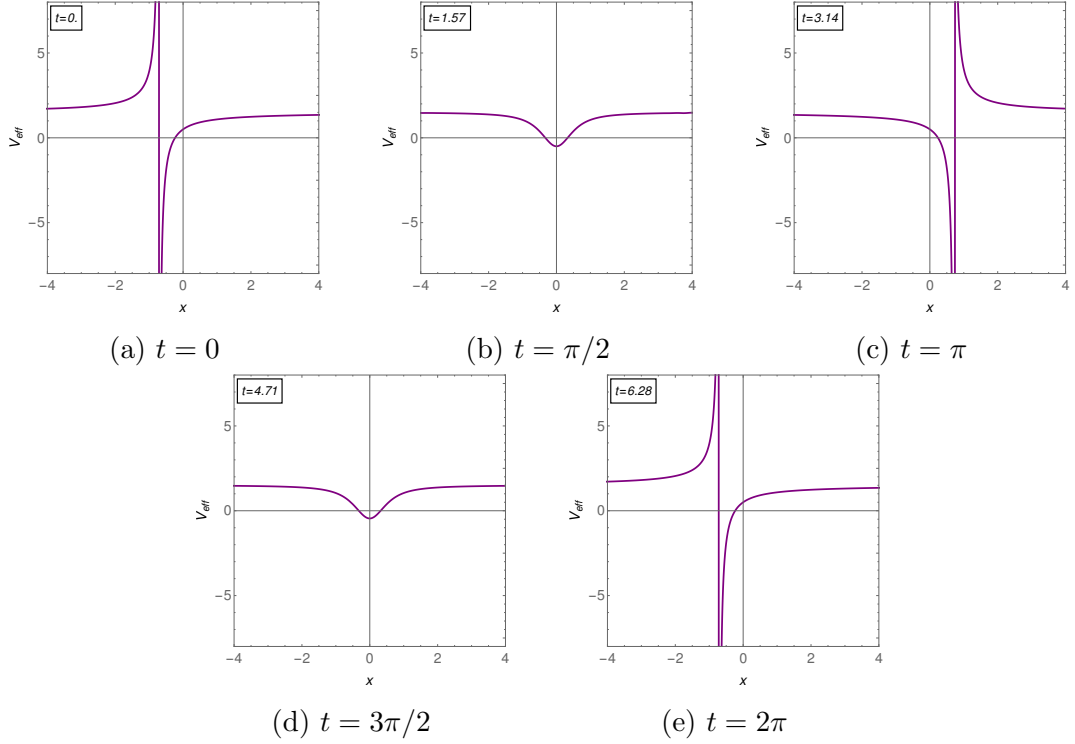


Figure 2.5: The evolution of  $V_{eff}$  over time for  $n = 1$ . Near the singularities the quantum potential varies very rapidly, implying in an immense amount of force. The changes in  $V_{eff}$  dictates the behavior of the Bohmian trajectories through the acceleration equation (2.8).

the number of initial states. Also, these quantum trajectories differ significantly from the classical case, even exhibiting master equations that allow us to understand the quantum systems based on classical mechanics. As mentioned earlier, this disparity arises from the presence of the quantum potential and its non-linear nature. Nevertheless, in consonance with the Ehrenfest theorem, we can speculate that a classical behavior could be achieved if we consider the mean values, since we have a quadratic classical potential. This is the primary objective of the next section.

## 2.4 The Ehrenfest theorem

In usual quantum mechanics, the temporal evolution of a Hermitian operator  $\hat{O}$  is given by the Heisenberg equation of motion

$$\frac{d\hat{O}}{dt} = \frac{\partial\hat{O}}{\partial t} + \frac{i}{\hbar}[\hat{H}, \hat{O}], \quad (2.21)$$

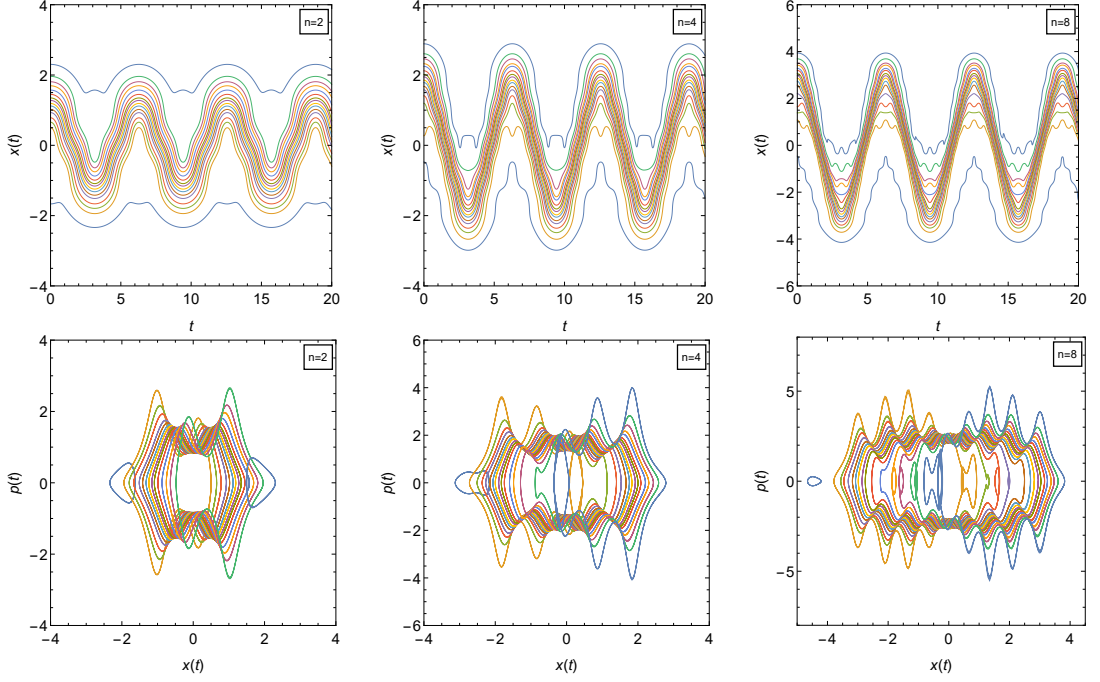


Figure 2.6: The Bohmian trajectories and the associated phase space for  $n = 2, 4, 8$ . As we increase the number of initial states, more complicated are the trajectories.

where  $\hat{H}$  is the Hamiltonian. In terms of expectation values we have that

$$\frac{d\langle\hat{\mathcal{O}}\rangle}{dt} = \left\langle \frac{\partial\hat{\mathcal{O}}}{\partial t} \right\rangle + \frac{i}{\hbar} \langle [\hat{H}, \hat{\mathcal{O}}] \rangle, \quad (2.22)$$

where the mean values in the usual interpretation are calculated via

$$\langle\hat{\mathcal{O}}\rangle = \int \Psi^*(\hat{\mathcal{O}}\Psi)dx. \quad (2.23)$$

For Hamiltonians which can be written as  $\hat{H} = \hat{p}^2/2m + V(\hat{x})$ , equation (2.22) provides for position and momentum operators the Ehrenfest theorem

$$m \frac{d\langle\hat{x}\rangle}{dt} = \langle\hat{p}\rangle, \quad (2.24)$$

$$\frac{d\langle\hat{p}\rangle}{dt} = -\langle\nabla V\rangle. \quad (2.25)$$

Since Bohmian mechanics and Copenhagen interpretation have the same statistical predictions, the mean values defined in both interpretations should be equal, that is,  $\langle\hat{\mathcal{O}}\rangle = \langle\mathcal{O}\rangle_{dBB}$ , where we denote  $\langle\mathcal{O}\rangle_{dBB}$  as the Bohmian average. However, in Bohmian Mechanics  $|\Psi|^2$  is interpreted as the probability density of an ensemble of positions. If at  $t = 0$  the initial positions are distributed with  $|\Psi(x_0, 0)|^2$ , each point will follow one individual trajectory so that, at a time  $t$ , the probability distribution of positions is

$|\Psi(x, t)|^2$ . Consequently,  $|\Psi(x, t)|^2 dx$  measure the probability of a particle being in an infinitesimal displacement  $dx$ . Hence,

$$\langle \mathcal{O}(t) \rangle_{dBB} = \int |\Psi(x, t)|^2 \mathcal{O}(x, t) dx \quad (2.26)$$

is the mean value of  $\mathcal{O}$ , where  $\mathcal{O}$  represents a physical property of the particles [32]. Despite the ensemble average in dBB be essentially different of the usual method of compute internal products of operators via the wave function (Equation (2.23)), the quantities from which we calculated the averages may have, beyond the classical part, contributions of quantum nature that should be considered. For instance, when computing the mean energy, we need to explicitly include the quantum potential contribution in addition to the kinetic and classical potential terms, according to Hamilton-Jacobi equation (2.5).

This fact is also true when we consider the Bohmian version of the Ehrenfest theorem. Taking the time derivative of the average position given in terms of Equation (2.26), we have that

$$\begin{aligned} \frac{d}{dt} \langle x \rangle_{dBB} &= \frac{d}{dt} \int R^2 x dx = \int \frac{\partial}{\partial t} (R^2 x) dx \\ &= -\frac{1}{m} \int x \frac{\partial}{\partial x} \left( R^2 \frac{\partial S}{\partial x} \right) dx \\ &= \frac{1}{m} \langle p \rangle_{dBB}, \end{aligned} \quad (2.27)$$

where, in this sequence of equations, we neglect the boundary terms and use the continuity equation (2.6) and guidance equation (2.4). Analogously, for the average momentum we have that

$$\begin{aligned} \frac{d}{dt} \langle p \rangle_{dBB} &= \frac{d}{dt} \int R^2 p dx = \int \frac{\partial}{\partial t} (R^2 p) dx \\ &= -\frac{1}{m} \int \frac{\partial}{\partial x} \left( R^2 \frac{\partial S}{\partial x} \right) \frac{\partial S}{\partial x} dx - \int R^2 \left[ \frac{1}{2m} \frac{\partial}{\partial x} \left( \frac{\partial S}{\partial x} \right)^2 + \frac{\partial V}{\partial x} + \frac{\partial Q}{\partial x} \right] dx \\ &= -\left\langle \frac{\partial V}{\partial x} \right\rangle_{dBB} - \left\langle \frac{\partial Q}{\partial x} \right\rangle_{dBB}, \end{aligned} \quad (2.28)$$

where, in addition to the previous considerations we also used the Hamilton-Jacobi equation (2.5). So, at first glance, beyond the classical force average, we have to consider the average of the quantum force as well. However, as we can verify, the contribution of the

second term vanishes, since

$$\begin{aligned}
\left\langle \frac{\partial Q}{\partial x} \right\rangle_{dBB} &= \int R^2 \frac{\partial Q}{\partial x} dx \\
&= -\frac{\hbar^2}{2m} \int R^2(x, t) \frac{\partial}{\partial x} \left( \frac{1}{R(x, t)} \frac{\partial^2 R(x, t)}{\partial x^2} \right) dx \\
&= \frac{\hbar^2}{m} \int \frac{\partial R(x, t)}{\partial x} \frac{\partial^2 R(x, t)}{\partial x^2} dx \\
&= -\frac{\hbar^2}{m} \int \frac{\partial^2 R(x, t)}{\partial x^2} \frac{\partial R(x, t)}{\partial x} dx.
\end{aligned} \tag{2.29}$$

Since the last two equations are equal, they should necessary be zero, and consequently  $\left\langle \frac{\partial Q}{\partial x} \right\rangle_{dBB} = 0$ . Therefore, the average of the quantum trajectories must obey

$$m \frac{d^2 \langle x \rangle_{dBB}}{dt^2} = - \left\langle \frac{\partial V}{\partial x} \right\rangle_{dBB}, \tag{2.30}$$

which can be identified as Newton's law if the average of the classical force is equal to the classical force applied to the average position, or in other words, if the relation  $\left\langle \frac{\partial V}{\partial x} \right\rangle_{dBB} = \frac{\partial V}{\partial x} \Big|_{x=\langle x \rangle_{dBB}}$  holds. For instance, considering potentials of the type  $V = \alpha x^n$ , in order to the averages obeys Newton's classical law we should have  $\langle x^{n-1} \rangle_{dBB} = \langle x \rangle_{dBB}^{n-1}$ , which is valid, for example, when  $n = 2$ . So, for the harmonic oscillator potential both quantities are equal, allowing us to see this ensemble of quantum particles collectively as one single classical particle. Yet, equation (2.30) can almost represent a classical law for  $\langle x \rangle_{dBB}$  in some cases, namely when we have a quadratic potential with small perturbations, or when the wave function is highly concentrate near to a single point during the Schrödinger evolution [45], being approximated by a delta function.

It is worth mentioning that in order to derive the equation (2.30), it was inherently necessary to use the fact that trajectories are distributed according to  $|\Psi|^2 = R^2$ , as shown in the sequence of equations (2.27), (2.28) and (2.29). Consequently, if we consider a distribution  $\mathcal{P}(x, t)$  that does not satisfy the quantum equilibrium hypothesis, specifically a  $\mathcal{P}(x, t)$  such that  $\mathcal{P}(x, t) \neq |\Psi(x, t)|^2$ , we must necessarily take into account the contribution due to the quantum force (Equation (2.28)), leading to a different result from the usual Ehrenfest theorem. As far as we know, this is a question that has not yet been explored.

### 2.4.1 Numerical validation of Ehrenfest theorem for the quantum harmonic oscillator

In the last section we saw how the Bohmian trajectories for the harmonic oscillator are completely different from the classical ones due the quantum effects, manifested by the presence of the quantum potential. This is true even in the case with  $n = 0$ . However, from the equation (2.30) and from the fact that for this specific case  $\left\langle \frac{\partial V}{\partial x} \right\rangle_{dBB} = \frac{\partial V}{\partial x} \Big|_{x=\langle x \rangle_{dBB}}$ , we expect that the Bohmian average of the quantum trajectories obeys a classical law.

Remembering that, according to classical mechanics, the classical harmonic oscillator position can be obtained integrating Newton's second law. The result is a sinusoidal function of the form  $x(t) = A \cos(\omega t + \phi)$ , implying that  $p = -mA\omega \sin(\omega t + \phi)$ , with  $A$  being the amplitude of the oscillations and  $\phi$  the phase. The energy is given by  $E = \frac{p^2}{2m} + V = \frac{1}{2}mA^2\omega^2$ . So, the ensemble of trajectories must, somehow, translate those properties.

Once we obtain the solution of equation (2.16) by distributing the initial positions according to the initial wave function used to solve Schrödinger equations (2.12) and (2.13), we guarantee that the probability distribution along the trajectories follows the wave function's evolution. So, for a relatively large number of trajectories, we can approximate the mean value of the positions by

$$\langle x(t) \rangle_{dBB} = \int |\Psi(x, t)|^2 x(t) dx \approx \frac{1}{N} \sum_{i=1}^N x_i(t), \quad (2.31)$$

where we perform a sum over the  $N = 400$  trajectories. We have a similar result for the momentum,

$$\langle p(t) \rangle_{dBB} = \int |\Psi(x, t)|^2 p(t) dx \approx \frac{1}{N} \sum_{i=1}^N p_i(t). \quad (2.32)$$

Thus, considering different initial wave functions given by (2.14), we compute the evolution of the average position and the average phase space. The results are plotted in Figure 2.7. The fit of all the curves results in the classical expression for  $x$ , but with a dependence on the quantum parameter  $n$ , that determines the number of eigenstates considered in the initial wave function. Specifically, we obtain that  $\langle x(t) \rangle_n = A_n \cos(\omega t)$ , with  $A_n$  the amplitude, depending on  $n$  according to a power law of the form  $A_n = \sqrt{n}$  (see Figure 2.8). Hence, we can consider that the quantum particles represent, on average, a classical harmonic oscillator that is initially displaced at a distance of  $\sqrt{n}$  from its equilibrium point. For  $n = 0$ , for example, we have a symmetric distribution, implying a classical oscillator initially located at the origin, which remains at rest all the time. However, as we increase the value of  $n$ , we change the initial position of the classical

oscillator, in response to consider an asymmetric distribution. Consequently, we obtain an oscillatory dynamics. This is a very interesting result because, despite in average we have a classical behavior, the amplitude has a dependence of a quantum nature. More precisely, the classical mean trajectory relies on the initial wave function. As we saw, classically the amplitude of the oscillations is related with the energy through the phase space. If we substitute the position and momentum by their respective dimensionless averages, we find that the mean phase space is a circle of radius  $A_n$ , with a volume that increases linearly with  $n$ , such as in [2.7](#).

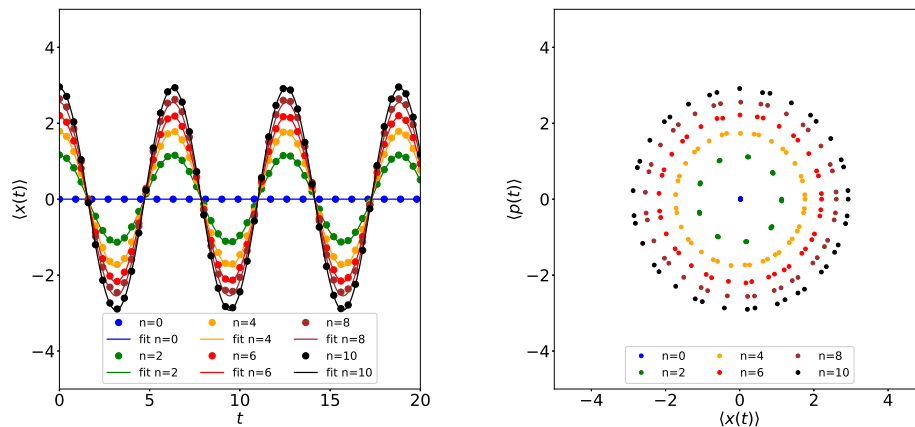


Figure 2.7: In the left, the dynamics of  $\langle x(t) \rangle_{dB}$ . All functions are optimally fitted by  $\langle x(t) \rangle_n = A_n \cos(\omega t)$ . In the right, the average phase space of the harmonic oscillator obtained by numerical results.

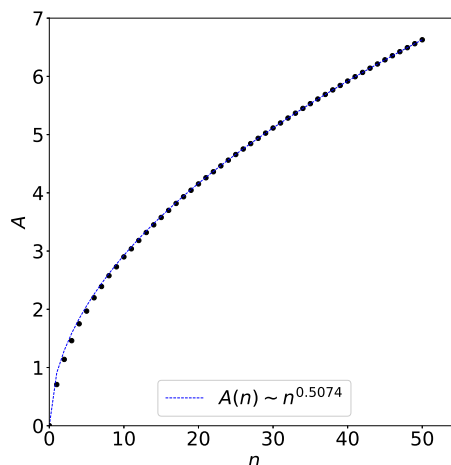


Figure 2.8: The amplitude  $A_n$  versus the total number of initial eigenstates. Performing a fit with  $n$  ranging from 0 to 50, we obtain a power law of the type  $A_n \sim n^{1/2}$ .

## 2.4.2 Forced Harmonic Oscillator

Despite the harmonic oscillator being a very studied case, it is not so evident the effect of an external force in the Bohmian trajectories. According to section [2.3](#), the Schrödinger equation in dimensionless variables can be reduced to

$$-\frac{1}{2} \frac{\partial^2 \Phi_r}{\partial x^2} + \left( \frac{1}{2} x^2 - F(t)x \right) \Phi_r = -\frac{\partial \Phi_i}{\partial t}, \quad (2.33)$$

$$-\frac{1}{2} \frac{\partial^2 \Phi_i}{\partial x^2} + \left( \frac{1}{2} x^2 - F(t)x \right) \Phi_i = \frac{\partial \Phi_r}{\partial t}, \quad (2.34)$$

where we made the substitution  $F(t) \rightarrow F(t)/\sqrt{\hbar m \omega_0^3}$  to obtain a dimensionless force, with  $\omega_0$  the fundamental frequency. Also, the Hamilton-Jacobi equation ([2.5](#)) has a correcting term  $F(t)x$  that should be considered:

$$\frac{\partial S}{\partial t} + \frac{(\vec{\nabla} S)^2}{2m} + V + Q - F(t)x = 0, \quad (2.35)$$

implying in a acceleration equation of the form

$$m \frac{d^2 \vec{x}}{dt^2} = -\vec{\nabla} V - \vec{\nabla} Q + F(t). \quad (2.36)$$

The effect of the external force on the solution of [\(2.33\)](#) and [\(2.34\)](#) changes the quantum potential and the continuity equation in a non-trivial manner, modifying the shape and the distribution of the trajectories. Nevertheless, the averages still follow a classical law, namely

$$m \frac{d^2}{dt^2} \langle x \rangle_{dBB} = -\langle \nabla V(x) \rangle_{dBB} + F(t), \quad (2.37)$$

since  $F(t)$  does not depend on  $x$ .

As is well known, the classical equation of motion for a driven harmonic oscillator is  $m\ddot{x} + m\omega_0^2 x = F_{ext}$ , which admits as solution

$$x(t) = x(t)_{HO} + \int_0^t d\tau F_{ext}(t - \tau) \sin(\tau) \quad (2.38)$$

where  $x(t)_{HO}$  is the particular solution of the unforced case, while the second term is a convolution relating the external force. Therefore, to verify the validation of the Ehrenfest theorem we expect something similar to Eq. [\(2.38\)](#). In order to elucidate this issue, we consider three distinct cases: a simple constant force, a fast-acting Gaussian impulse, and a sinusoidal signal where we investigate the resonance phenomenon.

## Constant Force

The most simple case is consider a constant force  $F = F_0$  without any time dependency, where we take  $F_0 = 0.7$  without loss of generality (see Figure 2.9). This system can be used to simulate a charged harmonic oscillator in a uniform electric field, for example, admitting an analytical solution that is expressed in terms of a shift in the position [43]. As a consequence, the mean distribution of the trajectories is also shifted by the same amount, which is well noted in the phase space. Classically, this represents an oscillator with the equilibrium point displaced of the original position as a result of the external force, similar to a vertical mass attached to a spring and subject to the gravitational field. Since the initial wave function corresponds to the ground state of the unforced case for  $n = 0$ , the mean initial position represents a point particle with an oscillatory dynamics, oppositely to what happens when  $F_0 = 0$ .

The averages (Figure 2.10) are in excellent agreement with the fit  $\langle x(t) \rangle_{dBB} = \langle x(t) \rangle_{HO} + 0.7(1 - \cos(t))$ , obtained from equation (2.38), showing the efficacy of the numerical procedure. The classical solution has the same structure of the harmonic oscillator without any external force, but the amplitude and the equilibrium point are change with  $F_0$ , namely,  $x \rightarrow x + F_0$  and  $A \rightarrow |A - F_0|$ .

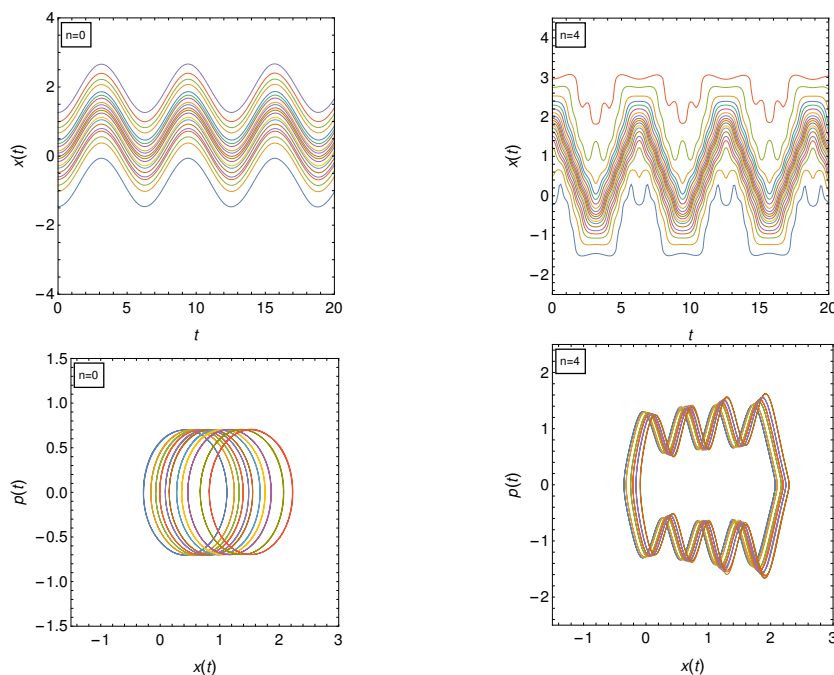


Figure 2.9: (top) Representative trajectories of a charged harmonic oscillator in the presence of a uniform electric field, for  $n = 0$ , in the left, and  $n = 4$ , in the right. (bottom) The phase for trajectories close to  $\max \{|\Psi(x, t)|^2\}$ . Note that the center is shifted to the right.

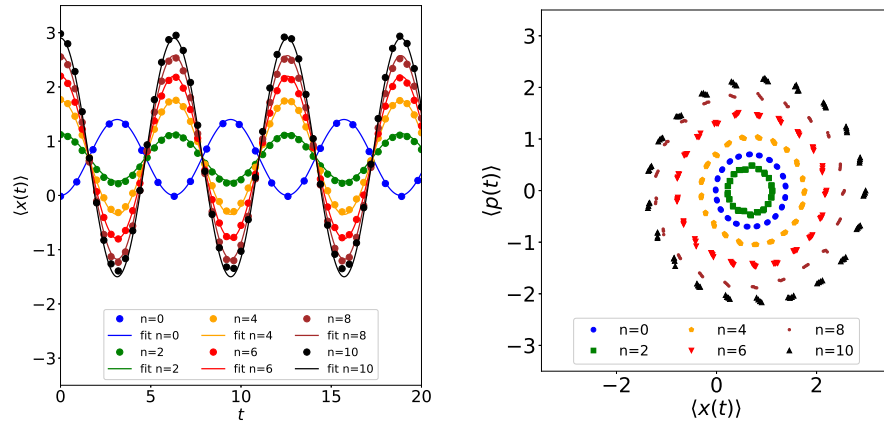


Figure 2.10: The average trajectories  $\langle x(t) \rangle_{dBB}$  (left) and the average phase space (right) for a constant force  $F(t) = 0.7$ . Note the change in amplitude and the shift in the oscillations.

### Impulsive Force

Impulsive forces have numerous applications in quantum mechanics. For example, in optomechanics [46, 47], in non-adiabatic transitions [48] and in prediction of quantum Gaussian systems [49]. To model such impulses we consider a fast acting force of Gaussian type  $F(t) = \frac{1}{\sqrt{2\pi\sigma^2}} \exp\left(-\frac{(t-t_\mu)^2}{2\sigma^2}\right)$ , with the parameters chosen such that  $t_\mu = 5$  and  $\sigma = 0.4$ .

This system is interesting because the asymptotically initial and final states are just the quantum harmonic oscillator. So, at the beginning, the trajectories are the same founded in sections 2.3 and 2.4. Since we are dealing with a non-conservative Hamiltonian, the Gaussian impulse increases the energy, leading the system to a more energetic level. Consequently the interaction excite more eigenstates in the wave function and the phase space expands (see Figure 2.11).

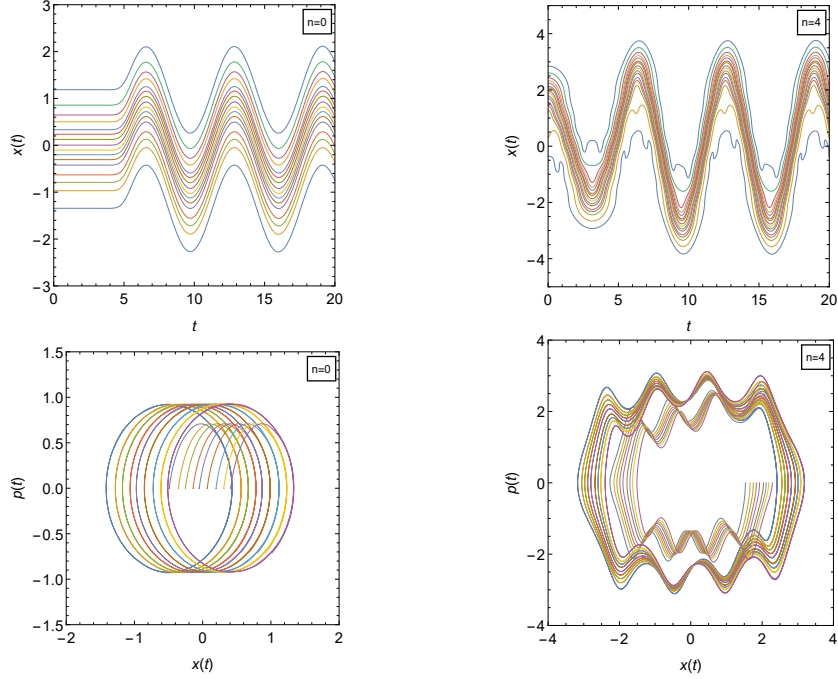


Figure 2.11: (top) Trajectories of the impulsive case for  $n = 0$ , in the left, and  $n = 4$ , in the right. (bottom) The associated phase space for central trajectories

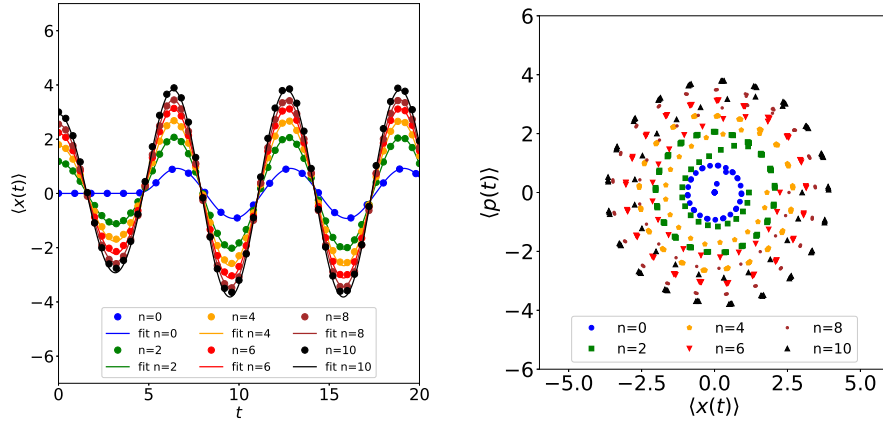


Figure 2.12: In the left, the dynamics of  $\langle x(t) \rangle_{dBB}$  for the impulsive force. In the right, the classical phase space obtained by the numerical procedures.

The mean trajectories are plotted in Figure 2.12. As expected, the averages coincides with the convolution (2.38), given two distinct regimes, before and after the force. The final vibrations have a greater amplitude, indicating a higher energy according to the classical laws. Note that for  $n = 0$  the oscillator that is at rest pass to vibrate after the impulse, indicating that the particles in the ensemble are not in an eigenstate anymore, but in some linear combination, no longer having static trajectories. Concerning the phase space, such effect can be viewed by the fast change of the trajectories into a circle of larger radius orbit. Thence, the quantum averages represent the classical analogue of a harmonic oscillator perturbed by a fast external impulse in the direction of movement,

which is responsible for increasing the amplitude of the vibrations and transferring energy to the system.

### Sinusoidal Force

The last example considered is the sinusoidal force  $F(t) = F_0 \cos(\Omega t)$ , with  $\Omega = \omega/\omega_0$  the ratio between the frequency of the oscillatory signal and the fundamental frequency. In the simulations we consider an amplitude of  $F_0 = 0.8$  for  $\Omega = 0.6$  and  $\Omega = 1.4$ . Each individual trajectory is the result of two periodic motions, so that the frequency is a combination of  $\omega$  and  $\omega_0$ , as can be seen in Figure 2.13. Once again the averages follow the convolution (2.38), satisfying the Ehrenfest theorem.

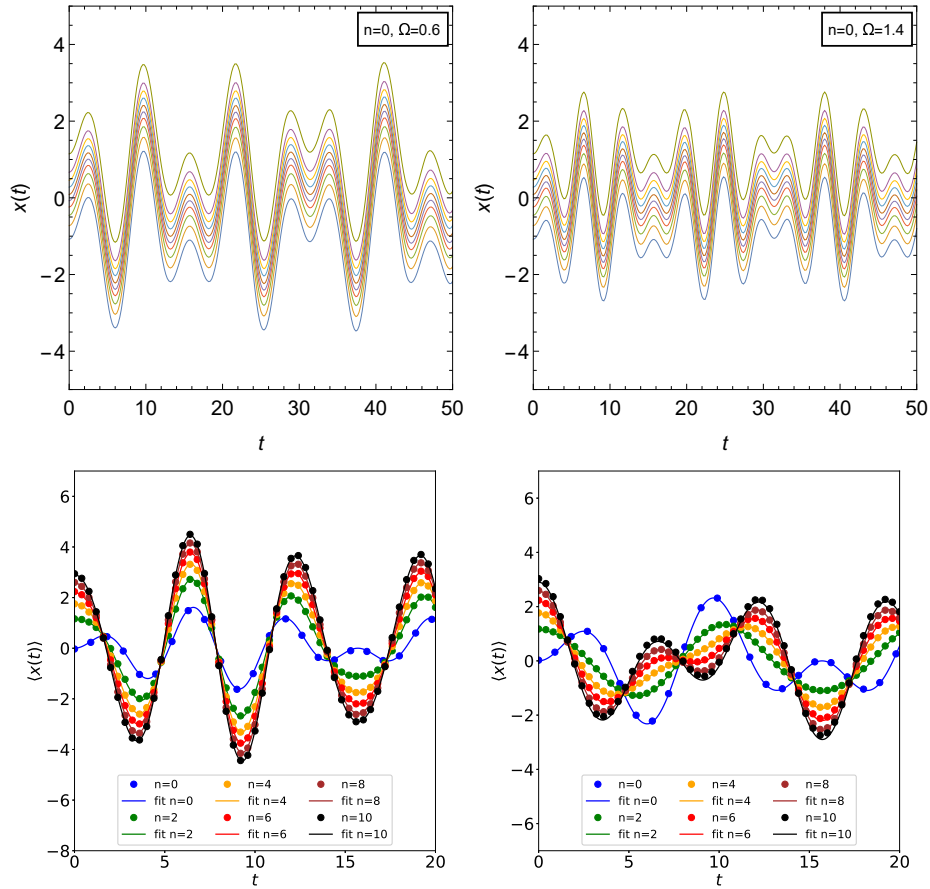


Figure 2.13: (top) The Bohmian trajectories for the sinusoidal force with  $n = 0$ . We considered  $F_0 = 0.8$ ,  $\Omega = 0.6$  (left), and  $\Omega = 1.4$  (right). (bottom) Average trajectories  $\langle x(t) \rangle_{dBB}$  for different values of  $n$ .

The resonant case  $\Omega = 1$  deserves special attention. Once the external frequency and the fundamental frequency are equal, we expect the force to make the amplitude of the oscillations grows indefinitely. This phenomenon is called quantum resonance, having applications in atomic optics [50], Polymethine dyes [51], multichromophoric energy transfer [52], electric-dipole moment experiments [53], and quasi-momentum measurements [54].

In order to avoid undesirable boundary effects in the results, we take  $F_0 = 0.2$  and  $L = 15$ . The numerical results reveals that the phase space exhibit a continuous increment of energy, with an expanding phase space volume, characterized by a periodic motion with increasing amplitude. The mean trajectories for  $n = 0$  also have a resonant motion, with a linear grow given by  $F_0 t/2$ , as shown in figure 2.14. This result is expected from the classical equations.

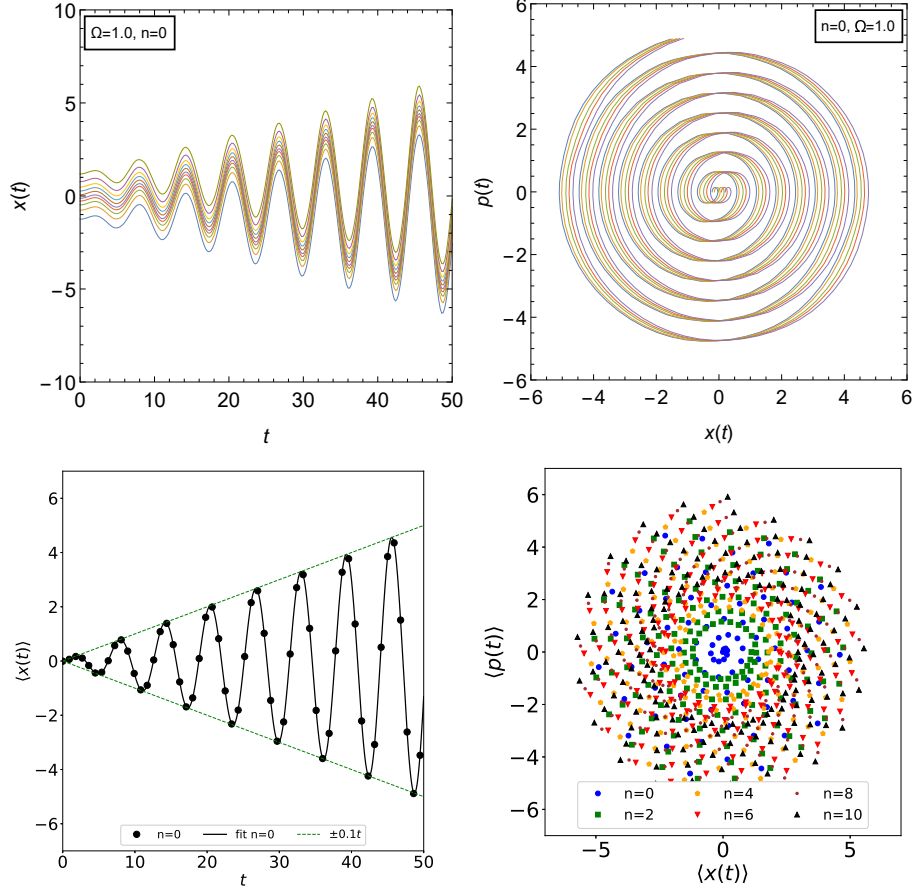


Figure 2.14: (top) Resonant trajectories for  $n = 0$  with  $F_0 = 0.2$  and (bottom) the mean trajectories.

As a conclusion, we verify that the average trajectories of all the cases considered obeys the classical equation (2.38), validating the Ehrenfest theorem even for those examples of non-conservative systems. It is worth to emphasize that the numerical approach is in great agreement with the expected classical solution, how is possible to see in all the fits. Therefore, our method can be used to study other quantum models that demands high precision, as chaotic trajectories and integrable systems exhibiting unstable orbits. Lastly, we wish to draw attention to the fact that, although obtaining such Bohmian trajectories may seem simple, as far as we know, there are few works referring to Bohmian trajectories with a time-dependent Hamiltonian. We believe that the main reason for this comes from the fact that usually such trajectories are obtained from a prior analytical knowledge of the wave function solution for any instant, which amounts to finding an

analytical solution of the time-dependent Schrödinger equation, a task that is not trivial when considering a generic system. Even knowing such a solution for the case of the quantum harmonic oscillator subjected to a constant force or that the solution for the impulsive case can be obtained in the asymptotic limits when the force is negligible, as we consider more complicated external forces, such as the sinusoidal one, for example, the analytical form of  $\Psi$  becomes too complicated. Therefore, to treat such cases, the numerical technique presented here is extremely useful. To the best of our knowledge, no one has ever presented the quantum trajectories for the three cases we consider:  $F = F_0$ ,  $F = \frac{1}{\sqrt{2\pi\sigma^2}} \exp\left(-\frac{(t-t_\mu)^2}{2\sigma^2}\right)$  and  $F = F_0 \cos(\Omega t)$ , where in this last one, we observe the resonance in the quantum trajectories. As an example of this discussion, in the next section we will illustrate the practicality of obtaining the numerical solution of the Schrödinger equation by considering the Duffing oscillator case.

## 2.5 The Duffing Oscillator

The Duffing Oscillator [55, 56] is a type of nonlinear oscillator with restoring force consisting of a linear and a cubic contributions, whose dynamics are described by a second-order nonlinear differential equation. It has a wide range of applications, such as in the modeling of electrical circuits [57, 58], in the analysis and detection of mechanical signals [59], in the study of chaotic phenomena [60, 61, 62, 63], and even employed in biological systems [64, 65, 66].

Let us consider the quantum version of the Duffing oscillator given in terms of the Hamiltonian

$$\hat{\mathcal{H}} = \frac{\hat{p}^2}{2} + \frac{\hat{x}^2}{2} + \frac{\lambda}{4}\hat{x}^4 - F_0\hat{x} \cos(\Omega t). \quad (2.39)$$

This system can be interpreted as a driven anharmonic oscillator, where  $\Omega$  is defined as the ratio between the external force frequency  $\omega$  and the natural frequency  $\omega_0$ , obtained when  $\lambda = 0$ , which corresponds to the harmonic oscillator driven by an oscillatory force studied in section 2.4.2. In order to compare this system with the results founded in the resonant case, we choose  $n = 0$ ,  $F_0 = 0.2$ , and  $\Omega = 1$  as the simulation parameters, while for the quartic potential  $\hat{V}_{anh} = \frac{\lambda}{4}\hat{x}^4$ , which is responsible for the anharmonicity, we consider  $\lambda = 0.01$  as a small perturbation.

Since the potential is not quadratic anymore, but have a quartic contribution, a difference between the first and third momentum, namely  $\langle x(t) \rangle_{dBB}$  and  $\langle x(t)^3 \rangle_{dBB}$ , arises. Therefore, as a consequence, we have that  $\langle \vec{\nabla} V(x) \rangle_{dBB} \neq \vec{\nabla} V(\langle x \rangle_{dBB})$ . Thus, the Bohmian averages do not exactly follow a Newton's second law-type equation, but in-

stead we have that

$$\frac{d^2}{dt^2} \langle x \rangle_{dBB} = -\langle x \rangle_{dBB} - \lambda \langle x^3 \rangle_{dBB} + F_0 \cos(\Omega t), \quad (2.40)$$

which can be approximately considered a Newton's law for small perturbations of the parameter  $\lambda$ . On the other hand, the corresponding classical equation for the Duffing oscillator is

$$\frac{d^2 x}{dt^2} = -x - \lambda x^3 + F_0 \cos(\Omega t), \quad (2.41)$$

whose solution can be obtained by numerical techniques.

The quantum solution of (2.40) is a little bit different from the classical solution obtained from (2.41) in reason of the difference  $\langle x(t)^3 \rangle_{dBB} - \langle x(t) \rangle_{dBB}^3 \neq 0$ . Even for a small perturbation constant, as the values of the coordinate become large, this difference also increases because of the anharmonicity. For small values of  $x$ , the quadratic term in the potential prevails. Therefore, we have the action of a resonant force in the Bohmian trajectories that gradually increases the amplitude of the oscillations, what causes the trajectories to deviate significantly from the origin, where the cubic term has a non-negligible contribution. Thus, in these regions we have a clear effect of anharmonicity, as can be seen in Figure 2.15. Even with the Ehrenfest theorem not corresponding to an exactly classical solution, it still holds. The mean trajectories have just a small deviation from the numerical solution obtained from the classical equation (2.41), showing that we have an approximately correspondence between the classical and quantum equations for small perturbations.

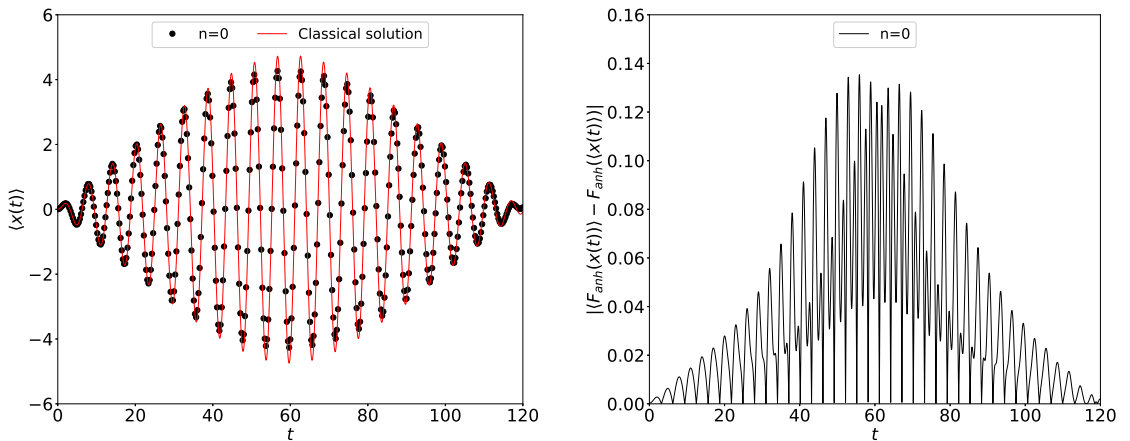


Figure 2.15: (left) Time evolution of the Bohmian averages  $\langle x(t) \rangle_{dBB}$  for the quantum Duffing oscillator (black points) and for the classical analogue (red line) with initial conditions  $(x_0, p_0) = (0, 0)$ . (right) Difference between  $\langle F_{anh}(x) \rangle_{dBB}$  and  $F_{anh}(\langle x \rangle_{dBB})$  where  $F_{anh}(x) = -\lambda x^3$  is the anharmonic force.

It is interesting to note that the behavior of the averages can be explained in the light

of a classical phenomenon. Instead of having a constantly increasing amplitude as happens in the resonant force case, we observe a beat-like pattern, one time that the anharmonic perturbation changes the fundamental frequency of the system from  $\omega_0$  to  $\omega_0 + \epsilon$ , with  $\epsilon$  a small correction. Because of that, we have the interference between two signs of almost equal frequencies, specifically the anharmonic vibration and the external force excitation, implying in a typical beating phenomenon. Such effect also can be observed in the individual Bohmian trajectories for  $n = 0$  (see figure 2.16), showing that this is not just an average effect. Conversely, as we increase the value of  $n$ , we start to have more complicated trajectories, losing this classical analogy. This arises primarily from the fact that a higher number of initial eigenstates lead to a distribution of initial positions more distant from the origin, where the effect of nonlinearity becomes more prominent.

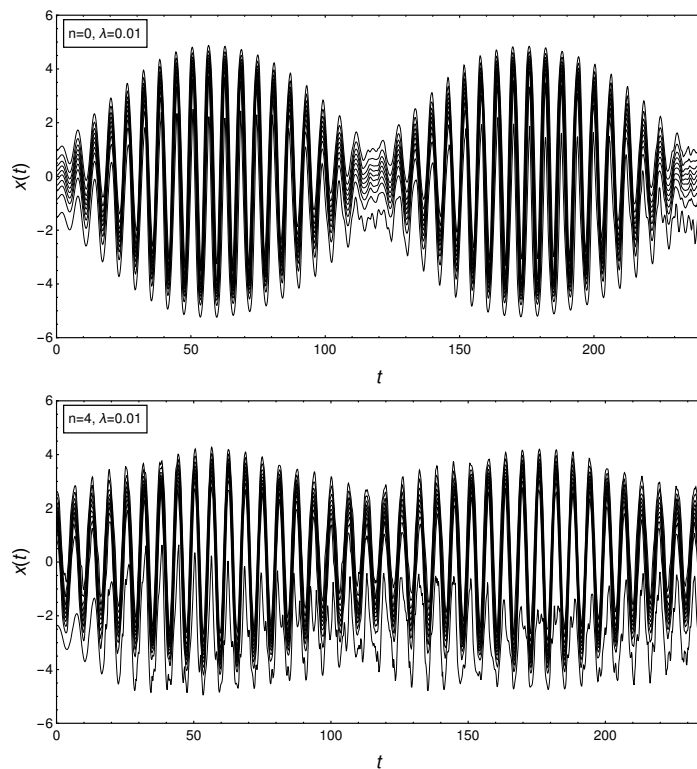


Figure 2.16: Bohmian trajectories for the Duffing oscillator in the cases  $n = 0$  and  $n = 4$ . Note that the beat pattern models the shape of the individual quantum trajectories, being more prominent in the central ones.

In the next chapter, we will pass to a two-dimensional problem, where we will use the numerical approach to obtain the Bohmian trajectories and study chaotic systems.

## Chapter 3

# Quantum Chaos and Bohmian Mechanics

The dynamics of chaotic systems [67, 68, 69] has been a topic of great interest in physics, with important discoveries in astronomy and celestial dynamics [70, 71], with special application in the study of the solar system [72, 73], as well as in the study of fluid dynamics [74, 75, 76], optics [77, 78], and plasma physics [79, 80]. Roughly speaking, a dynamical system is said to be chaotic if it exhibits some typical characteristics. The first, and perhaps the most important, is sensitivity to initial conditions. In chaotic systems, trajectories that start with very close initial conditions eventually tend to diverge and occupy very distinct regions of phase space, possessing completely different behaviors for sufficiently long times. Consequently, a second characteristic factor is the unpredictability of such systems. Due to the complexity of the equations of motion, this trajectories divergence, which occurs in an exponential ratio, makes it extremely difficult to predict the behavior of the physical system. In other words, there is no preferential representative position in phase space for a given time. Another important attribute that characterizes the presence of chaos is the aperiodicity of trajectories, which means that these systems do not exhibit regularities or repeated behaviors in a finite (long) time interval and do not follow periodic or quasiperiodic orbits. Lastly, even with the exponential divergence of neighboring particles, chaotic systems are expected to occupy a compact region in phase space, with highly dense trajectories.

From the previous discussion, we can define chaos for a deterministic system as a kind of long-term aperiodic behavior that presents sensitivity to initial conditions [69], with the nearby trajectories separating exponentially fast. Such sensitivity can be quantified by what we call of Lyapunov exponent  $\lambda$ . If two trajectories with initial conditions  $\vec{v}_1 = (\vec{x}_1, \vec{p}_1)$  and  $\vec{v}_2 = (\vec{x}_2, \vec{p}_2)$  in phase space are separated at the beginning by an infinitesimal amount  $\tilde{\xi}_0 = |\vec{v}_1 - \vec{v}_2| = \sqrt{\sum_i [(\delta x_i)^2 + (\delta p_i)^2]}$ , with  $\delta x_i$  and  $\delta p_i$  the individual distance concerning the  $i$ -th component of the position and momentum respectively, then for a generic time  $t$  the separation between the trajectories is  $\tilde{\xi}(t) = \tilde{\xi}_0 e^{\lambda t}$ . For a chaotic system,

if we plot the graphic of  $\ln \tilde{\xi}(t)$  versus  $t$ , the tendency will be to obtain a monotonically increasing line with positive slope. Usually, the Lyapunov exponent is a time-dependent quantity, with its evolution dictated by the dynamics of each system. Initially, when the separation between trajectories is small, it exhibits many oscillations, with often abrupt changes occurring over relatively short time intervals. However, as we increase the temporal variable, these oscillations become increasingly smaller, eventually reaching a saturation point. This occurs when the distance between the trajectories becomes comparable to the size of the geometric objects that causes chaos, which varies from system to system. Typically, these objects are referred to as strange attractors, which are geometric structures with a fractal dimension that characterizes their degree of self-similarity on different scales. For further clarifications on these structures, see [69].

Formally, the Lyapunov exponent is defined as follows:

$$\lambda(t) = \lim_{t \rightarrow \infty} \frac{1}{t} \ln \left( \frac{\tilde{\xi}(t)}{\tilde{\xi}_0} \right). \quad (3.1)$$

It is worth mentioning that its value depends on the choice of the set of initial conditions. Different initial positions in the phase space lead to different values of the Lyapunov exponents. It is common for a single physical system to have regions with almost non-exponential separation of trajectories, as well as regions with a high number of them, resulting in highly chaotic behavior. The calculation of the Lyapunov exponent in both regions provides quite different results, so we cannot treat the value of this quantity as a global characteristic for the entire phase space. The intermediate regions between the presence and absence of chaos are known as wedge of chaos and presents interesting features. For example, these regions can obey the q-statistics [81, 82, 83].

Although chaos in classical systems is well-understood, the study of chaos in quantum systems is, in a sense, limited due to the probabilistic nature of quantum mechanics, which contrasts with the deterministic nature of classical equations. Therefore, the quantum chaos [84, 85, 86, 87, 88, 89] is an open problem in the theory of quantum mechanics, with a wide range of applications, such as in nuclear physics [90, 91], quantum dots [92, 93], quantum computing [94, 95, 96, 97], and in black holes associated effects [98], being the main motivating topic behind this issue the correspondence between quantum and classical chaotic dynamics. Furthermore, chaotic dynamics are an important point in obtaining the Born rule for systems with initial conditions that do not obey the quantum equilibrium hypothesis, i.e., not distributed with  $|\Psi(\vec{x}, 0)|^2$  [99, 100, 101]. Attempts to study quantum chaos from a classical point of view involve searching for chaotic signatures at quantum level, by quantizing classical chaotic systems and analyzing the limits in which  $\hbar \rightarrow 0$  or  $n \rightarrow \infty$ , where  $n$  is the total number of eigenstates in the initial wave function. Such signatures are known in the literature as quantum scars, being quite recurrent in systems such as billiards [102, 103, 104] and quantum dots [105, 106]. In this approach, it

is interesting to analyze the energy levels of the studied system, for which one can use: 1) the random matrix theory [107], which assumes that the Hamiltonian of a complex system can be represented by a random matrix with appropriate statistical properties, allowing the extraction of important information regarding the spatial distribution between energy levels and the intensity distribution of the eigenfunctions, 2) the perturbation theory [108], which considers a small perturbation to the system's Hamiltonian due to an external parameter and verifies how this parameter influences the associated eigenenergies, and 3) the periodic orbit expansions [109], which is based on the idea that the energy spectrum of the quantum system in question can be represented by a sum over the contributions due to different periodic orbits.

Despite each one of these approaches allowing the understanding of important phenomena, they all need to deal with the problem of having a discrete energy spectrum, which makes it difficult to comprehend chaos from a quantum perspective. Therefore, it is often argued that dynamics at a quantum level do not strictly exhibit chaos as we know it classically, but only some indications of chaotic behavior at a macroscopic level. This is mainly due to the fact that a fundamental element for chaos to occur and we have an exponentially rapid divergence of nearby initially conditions, is the presence of nonlinearities. However, they are absent in the Schrödinger equation,  $i\hbar\partial_t\Psi = \hat{\mathcal{H}}\Psi$ , which is linear in  $\Psi$  [1]. Thus, if we only look at the Schrödinger equation, we are led to believe that chaotic dynamics, if they exist at the quantum level, must be the product of very specific conditions. However, this contradicts the fact that classical mechanics, which can be seen as a byproduct of quantum mechanics, exhibits chaos in the most different ways (see, for a few examples, [73, 112, 113, 114]).

This apparent paradox may be an indication that we are not approaching this problem correctly. From a classical point of view, we can inspect the presence or absence of nonlinearities through Newton's laws, for example. However, if we only look at Liouville's theorem, which states that the Hamiltonian evolution of a system preserves the volume of phase space, we are not able to observe any indication of nonlinearities. In fact, the Liouville equation  $\partial_t\rho = -\{\rho, H\}$  is linear in  $\rho$ , where  $\rho$  is the distribution of particles in phase space and  $\{.,.\}$  represents the Poisson brackets. Thus, following the previous reasoning, if we based ourselves solely on this result, we should not observe any exponential divergence of initially close trajectories, which contradicts various observations and computational experiments on classical systems that clearly exhibit chaos. Therefore, the Liouville equation is not the way to determine whether there will be chaos in a particular system. Similarly, perhaps for quantum systems, the correct way to discern the presence or absence of chaos is not through the Schrödinger equation, but rather at some other

---

<sup>1</sup>The only chance to have a nonlinear Schrödinger equation is if the potential explicitly depends on  $\Psi$ , as occurs, for example, in the Gross-Pitaevskii equation, which is very important in condensed matter physics for studying solitons and superfluids [110, 111].

dynamic equation of this theory.

In this sense, Bohm's interpretation of quantum mechanics fits very well. The introduction of quantum trajectories guided by the wave function results in highly nonlinear dynamic equations, attributed to the action of the quantum potential (see equation (2.8)). Thus, Bohm's view allows us to draw a perfect parallel between quantum and classical dynamics, so that chaotic trajectories appear as a natural phenomenon in both regimes. Note that this approach does not require the development of new techniques or tools to study quantum chaos. Due to the similarity between quantum and classical trajectories, we can import the same tools used in the study of classical chaos to quantum systems. In other words, we just need to integrate the equations of motion to determine whether a system is dissipative, ordered, weakly chaotic, or strongly chaotic.

Due to the computational advances of recent years, Bohmian mechanics has shown to be a very promising path in the study of chaos at quantum level, with many works carried out in the last decades, with theoretical and numerical developments on the subject founded in [11, 115, 116, 117, 118, 119, 120, 121, 122]. Examples of exponential divergence of initially close trajectories and the computation of positive Lyapunov exponents from this deterministic view of quantum mechanics are provided in [123, 124, 125], while the works [126, 127] present simple models of quantum chaotic systems. More recently, it has been shown how Bohmian dynamics explains the emergence of chaos from entangled qubits and its connection to ergodicity and Born rule [10, 128, 129].

The mechanism behind the emergence of chaos from Bohmian dynamics is extensive and complex, requiring knowledge of a range of specific concepts related to dynamical and complex systems. For detailed information on these aspects, please see reference [122]. In this chapter, we will provide a concise overview of the main known formalism responsible for the spreading of neighboring trajectories, applying it to two different examples: the anisotropic two-dimensional harmonic oscillator, which provides an analytically tractable solution, and the two-dimensional anharmonic oscillator featuring cubic and quartic interactions, where we developed a purely numerical approach to address the problem [3].

### 3.1 Nodal-Point-X-Point-Complex and vortices

The main mechanism responsible for the appearance of chaotic patterns in quantum system according to dBB formalism is the dynamical formation of vortices [11, 122], where due to the similarity between Bohmian trajectories and hydrodynamics, the formation of quantum vortices is quite common [130, 131, 132, 133, 134, 135] <sup>2</sup>. So, in order to approach this issue, we will consider two-dimensional systems, namely the 2D quantum harmonic

---

<sup>2</sup>Despite the majority of the studies in the literature indicating that the emergence of vortices may be the most viable path to achieve chaotic dynamics, there are cases of Bohmian systems that exhibit chaos even in the absence of this element [136].

oscillator and its derivatives. For Bohmian mechanics, the requirement of classical chaos is not a necessary or even sufficient condition for the existence of quantum chaos. Just as there are cases of systems that are classically chaotic but do not exhibit chaos at the quantum level [122], there are cases of systems that do not exhibit classical chaos but whose quantum counterpart is clearly chaotic [123].

To better understand this phenomenon, it is interesting to rewrite the velocity field in terms of the wave function as follows

$$\vec{p} = \hbar \Im \left( \frac{\vec{\nabla} \Psi}{\Psi} \right), \quad (3.2)$$

where  $\Im$  represents the imaginary part of the term in question. The quantum vortices are associated with points where the wave function vanishes [11], that is, regions where

$$\Re(\Psi) = \Im(\Psi) = 0, \quad (3.3)$$

what is equivalent to saying that  $\Psi_R = \Psi_I = 0$  in our previous notation. These regions are called nodal points in 2D systems and nodal lines in 3D systems, resulting in singularities in the phase of the wave function. In this hydrodynamic scenario, the creation and annihilation of vortices are dynamic and intrinsically associated with the evolution of the wave function through the guidance equations. As the system evolves in time, the phase of the wave function, which is also a function of time, changes. Thus, the nodal points move along the configuration space, carrying their respective vortices with them. This movement drastically affects neighboring trajectories, which can be attracted or repelled by the vortex center. The specific quantity of nodal points varies from system to system, ranging from a finite number to an infinite number. In general, the greater the number of such points, the more susceptible the system is to exhibiting chaos [134, 137], although there are cases where strong chaos manifests even with a small number of nodal points. This is a fundamental point, as systems with a high degree of chaos, measured by the Lyapunov exponent, for example, are capable of causing an initially probability distribution outside the quantum equilibrium to converge to the Born rule, without the need to postulate it [138, 139].

This resulting spreading of neighboring Bohmian trajectories can be better understood in a reference frame centered at the nodal point, with the help of the geometric structures known as Nodal-Point-X-Point-Complexes [122, 140, 141, 142, 143, 144]. A nodal point is said to be stable if sufficiently close trajectories are attracted towards it, while it is said to be unstable if they are repelled away from it towards regions of higher probability density around the nodal point. It is important to note that the presence of attractors or repellers does not contradict the fact that trajectories are found in regions of higher probability density, as the density remains small in the vicinity of the nodal point, making

it more likely for particles to be found in other regions. Additionally, due to the evolution of the wave function, the stability of the nodal point varies with time, and it can shift from stable to unstable. Thus, trajectories can be captured and circles the nodal points for a period of time and then be repelled when the transition occurs, significantly altering the topological aspect of the configuration space.

The other type of structure that, together with nodal points, generates the vorticity aspect observed when plotting the velocity field, is called X-points, which are unstable hyperbolic points in the nodal point reference system that accompany its evolution in configuration space [122]. From the perspective of dynamical systems, the X-points are equivalent to fixed points of the system, that is, points where the velocity field is zero. Physically, this implies that trajectories with an initial condition at one of these points will remain there indefinitely, being referred as fixed. The stability of a fixed point  $\vec{X}$  can be determined by linearizing the system in its vicinity and examining the convergence or divergence of the trajectories, which can be done by studying the eigenvalues of the correspondent Jacobian matrix, evaluated at  $\vec{X}$ . If we can approximate the velocity field as a linear system of the form  $\vec{v} = \vec{f}(\vec{x}) = J(\vec{x})|_{\vec{x}=\vec{X}} \vec{x}$ , where  $\vec{f}(\vec{x}) = (f_1(\vec{x}), f_2(\vec{x}))$  is the vector function that gives the velocity field,  $\vec{x} = (x, y)$  are the system coordinates, and  $J(\vec{x})|_{\vec{x}=\vec{X}} \vec{x}$  is its linearization, with  $J(\vec{x})$  being the Jacobian matrix given by

$$J(\vec{x}) = \begin{pmatrix} \frac{\partial f_1}{\partial x} & \frac{\partial f_1}{\partial y} \\ \frac{\partial f_2}{\partial x} & \frac{\partial f_2}{\partial y} \end{pmatrix}, \quad (3.4)$$

then the eigendirections will reveal whether the trajectories tend to approach or move away from the fixed point. In a reference system centered at  $\vec{X}$ , the Jacobian matrix takes a diagonal form, with its entries being the eigenvalues of  $J$ . In two dimensions, this corresponds to having a system of equations in the following form

$$\begin{aligned} \dot{x}' &= \sigma_1 x', \\ \dot{y}' &= \sigma_2 y', \end{aligned} \quad (3.5)$$

where  $\sigma_1$  and  $\sigma_2$  are the respectively eigenvalues, and  $(x', y')$  are the new coordinates. The solution to this system is simply  $x'(t) = x'_0 e^{\sigma_1 t}$  and  $y'(t) = y'_0 e^{\sigma_2 t}$ , which means that for negative eigenvalues, the associated eigendirections indicate an exponential approach to the fixed point, while positive eigenvalues indicate an exponential divergence. In other words, trajectories starting along a certain axis with an eigenvector corresponding to a negative (positive) eigenvalue will remain along that axis and tend to approach (move away from) the fixed point in this direction as time passes. Therefore, it is possible to determine the stability of trajectories by calculating the eigenvalues of  $J(\vec{x})|_{\vec{x}=\vec{X}}$ . The

X-points, in particular, have two divergent eigendirections along the positive eigenvalue axis and two convergent eigendirections along the negative eigenvalue axis, as indicated in Figure 3.1. As a result, trajectories tend to move away from the X-points, making them points of instability.

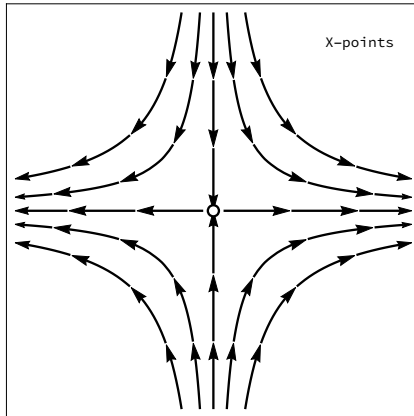


Figure 3.1: General configuration of a X-point, represented by the open dot. While the trajectories tend to approximate of  $\vec{X}$  in one direction, they move away from it along the other. Therefore the X-points acts as a saddle point that repels trajectories.

The nodal points together with the X-points form complex geometric structures, known as Nodal-Points-X-Points-Complexes (NPXPCs), responsible for the scattering of initially nearby trajectories. In Figure 3.2, we illustrate a typical velocity field (in the nodal point reference frame) of a Bohmian quantum system exhibiting such structure. Quantum trajectories tend to follow the flow defined by the vector field, leading to three scattering regions and one stability region around the vortex. Trajectories close to the nodal point  $N$  are confined within the region bounded by the gray loop (left figure), being either attracted to or repelled from  $N$  depending on the stability of the nodal point, while the remaining trajectories tend to follow one of the positive eigenvalue eigendirections associated with the X-point (right figure).

In the following, we will discuss two Bohmian systems that can exhibit chaos at quantum level and serve as good examples for the concepts presented here: the anisotropic two-dimensional harmonic oscillator studied at [11, 121, 122, 123] and the coupled two-dimensional anharmonic oscillator [3]. Regarding the first system, we will employ a semi-analytical approach since it admits a known solution to the Schrödinger equation. However, for the second case, we will adopt a fully numerical approach.

## 3.2 Anisotropic two-dimensional harmonic oscillator

As a direct extension of what was done in section 2.3, we will consider the case of the two-dimensional harmonic oscillator. In addition to the dimensional factor, we will also introduce an anisotropy in terms of the natural oscillation frequencies along the  $x$

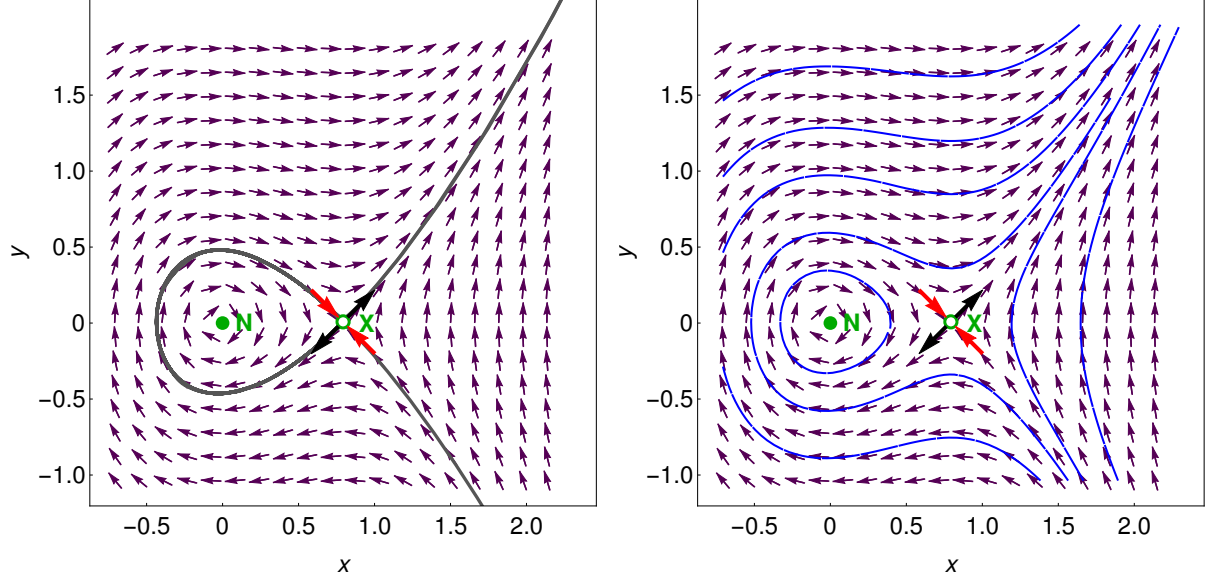


Figure 3.2: Typical velocity field of a Bohmian system. The nodal point  $N$  and the X-point are highlighted in green. The red vectors represent the approaching eigendirections, while the black vectors represent the departing eigendirections. The gray contour (left figure) delineates the scattering regions. Trajectories outside this contour will be scattered by the NPXPC, while trajectories inside it will orbit the nodal point (right figure).

and  $y$  axes. The Hamiltonian of such a system can be written as  $\hat{\mathcal{H}} = \frac{\hat{p}_x^2}{2m} + \frac{\hat{p}_y^2}{2m} + \frac{1}{2}m\omega_x^2\hat{x}^2 + \frac{1}{2}m\omega_y^2\hat{y}^2$ , where  $\omega_x$  and  $\omega_y$  are the frequencies. In dimensionless variables, the corresponding Schrödinger equation is

$$-\frac{1}{2}\nabla^2\Psi + \frac{1}{2}(x^2 + \omega^2y^2)\Psi = i\frac{\partial\Psi}{\partial t}, \quad (3.6)$$

where  $\nabla^2 = \partial_x^2 + \partial_y^2$  is the Laplacian operator, and  $\omega = \omega_y/\omega_x$  is the ratio between the frequencies along the  $y$  and  $x$  axes, respectively. The associated eigenfunctions are, therefore,

$$\psi_{mn}(x, y, t) = \frac{\omega^{1/4}}{\sqrt{2^{m+n}m!n!\pi}}H_m(x)H_n(\sqrt{\omega}y)\exp\left[-\frac{1}{2}(x^2 + \omega y^2)\right]e^{-iE_{mn}t}, \quad (3.7)$$

with  $E_{mn} = \left(m + \frac{1}{2}\right) + \left(n + \frac{1}{2}\right)\omega$  the correspondent eigenenergy.

Let us consider an initial state that is the sum of the three following eigenfunctions

$$\Psi(x, y, 0) = c_0\psi_{00} + c_1\psi_{10} + c_2\psi_{11}, \quad (3.8)$$

with  $c_0, c_1, c_2$  real constants [11, 123]. In our numerical simulations we set  $c_0 = \sqrt{\frac{4}{7}}$ ,  $c_1 = \sqrt{\frac{2}{7}}$  and  $c_2 = \sqrt{\frac{1}{7}}$  in order to have a properly normalized initial wave function. At first glance, despite the anisotropy, we expect that the oscillations concerning the

individual spatial dimensions occur independently since there is no coupling between the  $x$  and  $y$  directions. Thus, we can analyze this system from the perspective of two separate individual oscillations with different frequencies. Since the one-dimensional harmonic oscillator does not exhibit any trace of chaotic behavior (the trajectories are periodic and do not show exponential divergence), as shown in Section [2.3](#), we predict that the two-dimensional extension will also be devoid of chaos. However, as we will demonstrate shortly, this is not true in the case of an irrational ratio between the individual frequencies, i.e., when  $\omega$  is not a rational number.

After simplification, the time dependent wave function can be expressed as

$$\Psi(x, y, t) = \frac{\omega^{1/4} e^{\frac{1}{2}(-3it(\omega+1) - x^2 - y^2\omega)}}{\sqrt{\pi}} \left( c_0 e^{it(\omega+1)} + \sqrt{2}c_1 x e^{it\omega} + 2c_2 xy \sqrt{\omega} \right), \quad (3.9)$$

which will be null when the term inside the parentheses vanishes. This condition implies that

$$c_0 \cos[t(\omega + 1)] + \sqrt{2}c_1 x \cos(t\omega) + 2c_2 xy \sqrt{\omega} = 0, \quad (3.10)$$

$$c_0 \sin[t(\omega + 1)] + \sqrt{2}c_1 x \sin(t\omega) = 0. \quad (3.11)$$

The solution to this system gives us the location of the nodal point as a function of time. Namely, we have that

$$x_N(t) = -\frac{c_0 \sin[t(\omega + 1)] \csc(t\omega)}{\sqrt{2}c_1}, \quad (3.12)$$

$$y_N(t) = -\frac{c_1 \sin(t) \csc[t(\omega + 1)]}{\sqrt{2}\omega c_2}, \quad (3.13)$$

which are oscillatory functions that changes significantly as we vary the value of  $\omega$ . In Figure [3.3](#), we present a parametric plot in two distinct situations: for  $\omega = 7/10 = 0.7$  and for  $\omega = 1/\sqrt{2} = 0.7071\dots$ , up to the time  $t = 1000$ . It is worth noting that while in the first case, the trajectory is more limited due to the periodicity manifested in equations [\(3.12\)](#) and [\(3.13\)](#), in the second one, we observe a much more dispersed nodal point trajectory that occupies a significantly larger region in the configuration space, making the system more susceptible to manifest a chaotic regime. Despite that, for a rational value of  $\omega$ , the more complicated the ratio between the frequencies is, the more complex and sparse will be the trajectory defined by  $x_N(t)$  and  $y_N(t)$  and we will have a behavior similar to the irrational case [\[145\]](#). However, for sufficiently long times, the periodic nature of the associated solutions becomes evident and this apparent chaos ends up disappearing [\[122\]](#), which can be verified by calculating the Liapunov exponent.

As we mentioned, the other important structure are the X-points, defined in the nodal points reference frame and that accompanies its evolution. Using the guidance equation

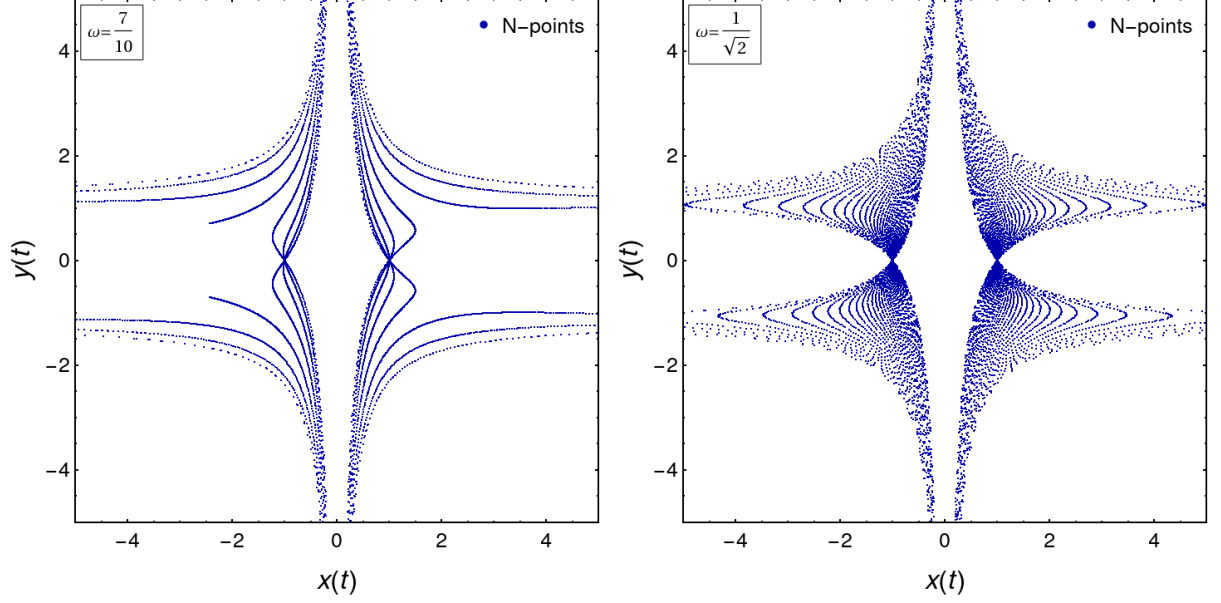


Figure 3.3: Comparison between the trajectory of the nodal point in the cases of a rational ratio ( $\omega = 7/10 = 0.7$ ) in the left figure and an irrational ratio ( $\omega = 1/\sqrt{2} = 0.7071\dots$ ) in the right figure. In the first case, the trajectory of the nodal point is simpler and occupies a significantly smaller region in the configuration space compared to the second case, which exhibits a much more dispersed trajectory.

(3.2) for the wave function (3.9) we obtain the velocity field components

$$v_x(t) = -\frac{c_0 \left( \sqrt{2}c_1 \sin(t) + 2c_2y\sqrt{\omega} \sin[t(\omega + 1)] \right)}{D}, \quad (3.14)$$

$$v_y(t) = \frac{2c_0x \left( c_0\sqrt{\omega} \sin[t(\omega + 1)] + \sqrt{2\omega}c_1x \sin(t\omega) \right)}{D}, \quad (3.15)$$

with  $D$  a common denominator given by

$$D = c_0^2 + 2\sqrt{2}c_0c_1x \cos(t) + 2x^2 \left( c_1^2 + 2\sqrt{2}c_1c_2y\sqrt{\omega} \cos(t\omega) + 2c_2^2y^2\omega \right) + 4c_0c_2xy\sqrt{\omega} \cos[t(\omega + 1)]. \quad (3.16)$$

Also, from equations (3.12) and (3.13) we can derive the velocity components associated with the nodal point. More precisely,

$$v_x^N(t) = -\frac{c_0 \csc(t\omega)}{\sqrt{2}c_1} \left\{ (\omega + 1) \cos[t(\omega + 1)] - \omega \sin[t(\omega + 1)] \cot(t\omega) \right\}, \quad (3.17)$$

$$v_y^N(t) = \frac{c_1 \csc[t(\omega + 1)]}{\sqrt{2\omega}c_2} \left\{ (\omega + 1) \sin(t) \cot[t(\omega + 1)] - \cos(t) \right\}. \quad (3.18)$$

Now, from the perspective of a comoving reference frame centered on the nodal point, with coordinates  $u = x - x_N$  and  $v = y - y_N$ , the trajectory of a Bohmian particle is

determined by the velocity field components  $v_u = v_x - v_x^N$  and  $v_v = v_y - v_y^N$ , which have a somewhat complicated analytical form

$$v_u = -\frac{2c_0c_2\sqrt{\omega}v \sin[t(\omega + 1)]}{\mathcal{D}} - v_x^N(t), \quad (3.19)$$

$$v_v = -\frac{\sqrt{2\omega}c_2u \left( \sqrt{2}c_0 \sin[t(\omega + 1)] - 2c_1u \sin(t\omega) \right)}{\mathcal{D}} - v_y^N(t). \quad (3.20)$$

Here,  $\mathcal{D} = D_1 + D_2 + D_3$ , with the coefficient  $D_1$  given by

$$D_1 = c_0^2 + 2c_0 \cos(t) \left( \sqrt{2}c_1u - c_0 \sin(t(\omega + 1)) \csc(t\omega) \right), \quad (3.21)$$

with  $D_2$  such that

$$D_2 = \frac{c_0}{c_1} \cos[t(\omega + 1)] \left( \sqrt{2}c_0 \sin[t(\omega + 1)] \csc(t\omega) - 2c_1u \right) \times \\ \left( \sqrt{2}c_1 \sin(t) \csc[t(\omega + 1)] - 2c_2v\sqrt{\omega} \right), \quad (3.22)$$

and with  $D_3$  being

$$D_3 = \frac{1}{2c_1^2} \left( \sqrt{2}c_0 \sin[t(\omega + 1)] \csc(t\omega) - 2c_1u \right)^2 \times \\ \left\{ c_1^2 + \frac{1}{2} \left( \sqrt{2}c_1 \sin(t) \csc[t(\omega + 1)] - 2c_2v\sqrt{\omega} \right)^2 + \right. \\ \left. \sqrt{2}c_1 \cos(t\omega) \left( 2c_2v\sqrt{\omega} - \sqrt{2}c_1 \sin(t) \csc[t(\omega + 1)] \right) \right\}. \quad (3.23)$$

The X-point  $(u^X, v^X)$  is defined as the point where this velocity field (equations (3.19) and (3.20)) vanishes, that is, the solutions of the system  $v_u = 0$  and  $v_v = 0$ , which can be obtained numerically. In this particular case, we employed the Newton-Raphson optimization method [146], available within the FindRoot routine in *Mathematica* [147, 148]. In summary, this method involves using a linear approximation of a given system and iteratively finding its solution starting from an initial guess. In order to ensure the convergence to the X-Point, it is advisable to visually inspect the velocity field and use a initial guess close to the nodal point, calculated through equations (3.12) and (3.13), and compare the obtained result with the apparent position of X-Point. In Figure 3.4, we plot the trajectory of the nodal point in configuration space along with the X-point until time  $t = 10$ . It is worth mentioning that for this time interval, there is not much difference between the dynamics described for  $\omega = 7/10$  and  $\omega = 1/\sqrt{2}$ .

How is possible to observe, the distance between these two structures is quite variable. Therefore, the volume defined by the NPXPC changes with time, which significantly affects the trajectories of the neighboring quantum particles. Indeed, the average radius

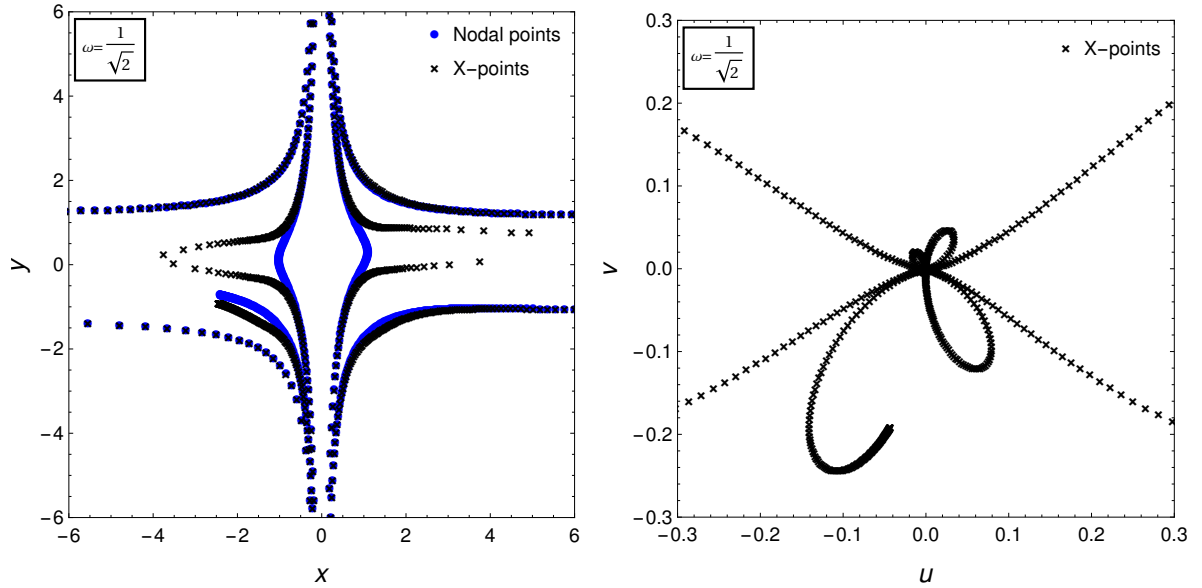


Figure 3.4: (left) The evolution of the nodal point, in blue, accompanied by the X-point, in black, in the original reference frame, with coordinates  $(x, y)$ . (right) The trajectory of the X-Point in the reference frame centred at the nodal point, with coordinates  $(u, v)$ . Please note that the distance between the nodal point and the X-point varies significantly as time passes, implying in a changing of volume of the NPXPC.

$\bar{r}$  of the NPXPC varies by approximately  $10^5 \sim 10^6$  orders of magnitude throughout its evolution, resulting in an extremely small volume for instances of close proximity between the nodal point and the X-Point (regions of intersection between the blue and black curves in the first plot of Figure 3.4). This change in the size of the NPXPC can occur rapidly, as illustrated in Figure 3.5. In the left photo, taken at  $t = 1.3$ , we plot the velocity field for the rectangular region  $[-0.20, 0.15] \times [-0.20, 0.15]$ , where an NPXPC with an  $\bar{r} \sim 10^{-1}$  is observed. Shortly after, at  $t = 1.73$ , the velocity field in the same region appears almost constant. However, upon zooming in, we observe an NPXPC with an average radius  $10^3$  times smaller, i.e., with  $\bar{r} \sim 10^{-4}$ . As a consequence of this dynamics, these geometric structures can be highly effective in scattering neighboring trajectories, in different directions, with initial conditions differing by a distance  $|\delta\vec{x}| \sim \bar{r}$ . In cases where  $|\delta\vec{x}| \ll \bar{r}$ , the trajectories tend to be scattered in the same direction and there is no effective separation between them. However, since the average radius varies with time, even if the trajectories initially remain close, they may eventually diverge as  $|\delta\vec{x}|$  becomes comparable to  $\bar{r}$ .

The interaction between Bohmian trajectories and NPXPCs depends primarily on the positions of the quantum particles at each instant. To understand the behavior of these structures and their impact on the system's dynamics, it is interesting to study the eigendirections associated with the X-point. This can be accomplished by tracing the velocity field at a fixed time and analyzing the subsequent evolution of the particles, assuming the field configuration remains constant. To achieve this, we numerically integrate

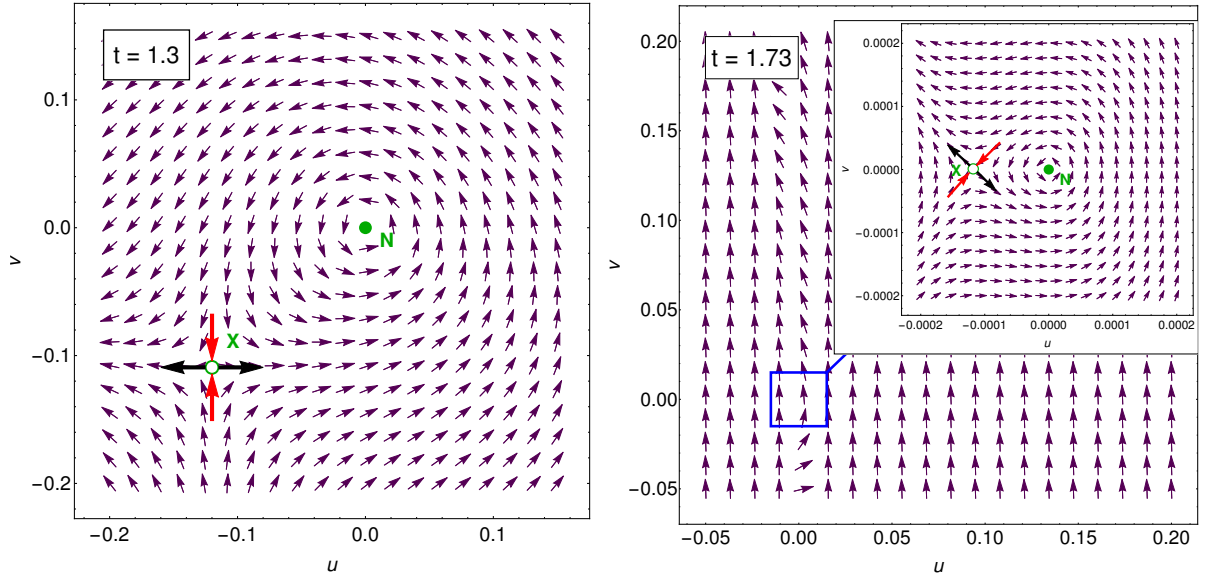


Figure 3.5: The representation of the velocity field in two different moments. At  $t = 1.3$ , in the left, we observe a NPXPC with size  $\bar{r} \sim 10^{-1}$ . At  $t = 1.73$ , into the right, we observe the same structure but with  $\bar{r} \sim 10^{-4}$ .

the associated ordinary differential equation (ODE) to obtain the particle positions for an auxiliary fictitious time. In practical terms, it is as if we pause a movie at a specific moment and use this frozen scene to predict what will happen next. As expected, this prediction is not reliable since we cannot fully anticipate the details of the entire scene by analyzing only a specific segment. We would need to let the movie play to uncover its exact unfolding. Nonetheless, through this analysis, we gain a predictive power, albeit brief, of how these geometric structures will affect the trajectories in the near future.

From Figure 3.6, where stable eigendirections (with negative eigenvalues) are represented by red curves and unstable eigendirections (with positive eigenvalues) by black curves, we observe three scattering regions due to the unstable eigendirections and a region of orbit around the vortex. In the left photo, taken at  $t = 2.35$ , we have a stable vortex that attracts trajectories. That is, particles with initial positions close to the unstable eigendirection pointing to the vortex are repelled from the X-point towards the nodal point, while those with initial positions close to the red curves approach the X-point but are gradually repelled. In contrast, in the right photo, taken at  $t = 2.43$ , we observe that the vortex in question is unstable and tends to repel trajectories whose initial conditions lie in its vicinity, directing them towards the X-point. Again, even if we start close to the red curve outside the vortex, the velocity field configuration eventually leads us towards the regions near the black curves, causing the particles to be repelled. This stability transition of the nodal point is characteristic of what is known in the literature as a Hopf bifurcation [149, 150, 151, 152], which is typically accompanied by the appearance of a limit cycle [69, 122]. In some cases, two or more particles near a stable vortex may follow it as it evolves, but they eventually are expelled when it becomes unstable, which

can result in the divergence of trajectories. The same thing can happen if they approach distinct unstable eigendirections, which is more likely to happen if  $\delta\vec{x} \sim \bar{r}$ .

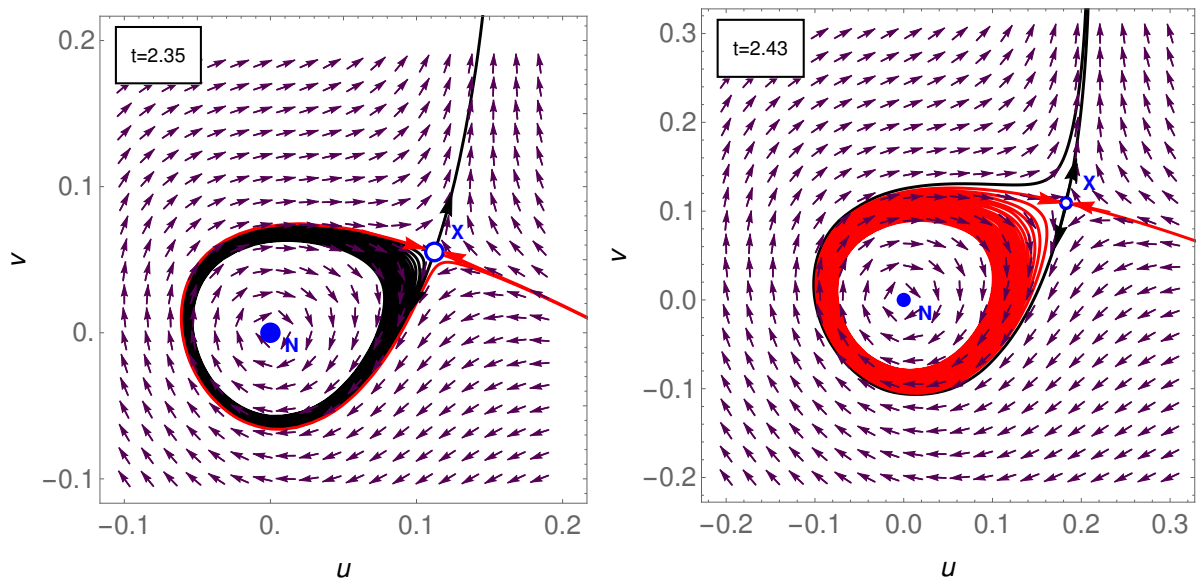


Figure 3.6: The evolution of NPXPC: for  $t = 2.35$  we have a stable vortex, whereas for  $t = 2.43$  we have an unstable one. The black curves are associated with X-point eigendirections with positive eigenvalues, while the red curves correspond to eigendirections with negative eigenvalues. Particles inside the red loop (left figure) are repelled by the X-point in the direction of the nodal point, while particles outside the loop are scattered by the NPXPC. On the contrary, particles inside the black loop (right figure) are repelled away from the vortex center, tending towards the X-point. Once again, particles outside this region are repelled by the NPXPC due to the presence of unstable eigendirections

The Bohmian particles tend to approach the NPXPC intermittently during their evolution, being subject to its influence during each approach. The greater the number of interactions, the higher the probability of observing exponential deviation of trajectories and, consequently, chaotic behavior. On the other hand, trajectories that are not subject to the influence of NPXPC tend to exhibit ordered behavior. Thus, a notable difference is observed between the cases when  $\omega = 7/10$  and  $\omega = 1/\sqrt{2}$ . In the first one, due to the periodic nature of equations (3.12) and (3.13), the nodal point, which is the center of NPXPC, has a more restricted action in configuration space compared to the case with an irrational frequency ratio (see Figure 3.3). Conversely, the latter presents a much sparser nodal point trajectories in configuration space, allowing for a greater number of interactions with quantum particles throughout its evolution, leading to their eventual spreading. In Figure 3.7 we plot the quantum trajectories obtained integrating the guidance equations (3.14) and (3.15) in the  $\omega = 7/10$  case, for five different initial conditions.

All curves were plotted up to a time  $t = 150$ . The central trajectory, shown in black, occurs in a region practically free from the presence of nodal points, resulting in a highly regular orbit. In the other trajectories, despite the action of NPXPC, it is not capable of introducing a chaotic character. The quantum particles start at the chosen

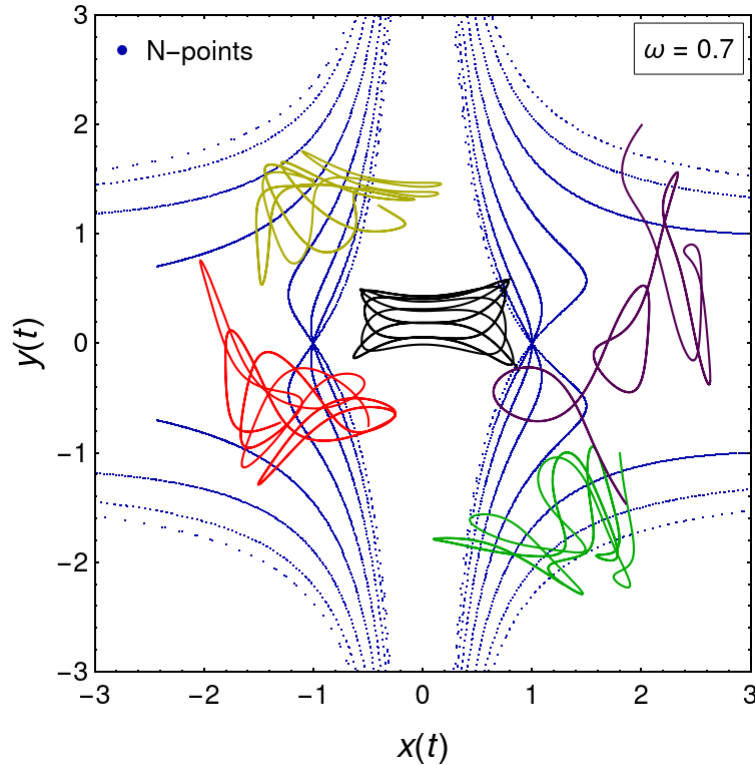


Figure 3.7: The quantum trajectories in configuration space for  $\omega = 7/10$ . We consider five different initial conditions:  $(x_0, y_0) = (-0.5, -0.75)$  in red,  $(x_0, y_0) = (0.8, 0.6)$  in black,  $(x_0, y_0) = (1.8, -1.0)$  in green,  $(x_0, y_0) = (2.0, 2.0)$  in purple, and finally  $(x_0, y_0) = (-1.0, 1.5)$  in yellow. In the background, the blue points represent the evolution of the nodal point.

initial condition and propagate according to the velocity field until reaching a point of return, after which there is a backtrack along the path, returning to the starting point. This cycle repeats continuously, confining the particles to the region delimited by the highlighted curves, with no evidence of chaos. In Figure 3.8, we plot the evolution of  $x(t)$  and  $y(t)$  separately for the case where  $(x_0, y_0) = (-0.5, -0.75)$  (red curve), where we verify the periodicity associated with this particular trajectory. It is a regular, periodic motion without the presence of exponential divergence of particles.

We can rigorously prove this assertion by numerically calculating the Lyapunov exponent (equation (3.1)), which can be obtained using the method presented in [153, 154]. Given the guidance equations 3.14 and 3.15, we can obtain the associated variational equations, namely,

$$\frac{d}{dt} \delta x = \frac{\partial v_x}{\partial x} \delta x + \frac{\partial v_x}{\partial y} \delta y, \quad (3.24)$$

$$\frac{d}{dt} \delta y = \frac{\partial v_y}{\partial x} \delta x + \frac{\partial v_y}{\partial y} \delta y, \quad (3.25)$$

which must be solved together with the guidance equations and used for the calculation of  $\lambda$ . To solve this system of ODEs, we employed the eighth-order fixed-step Runge-Kutta

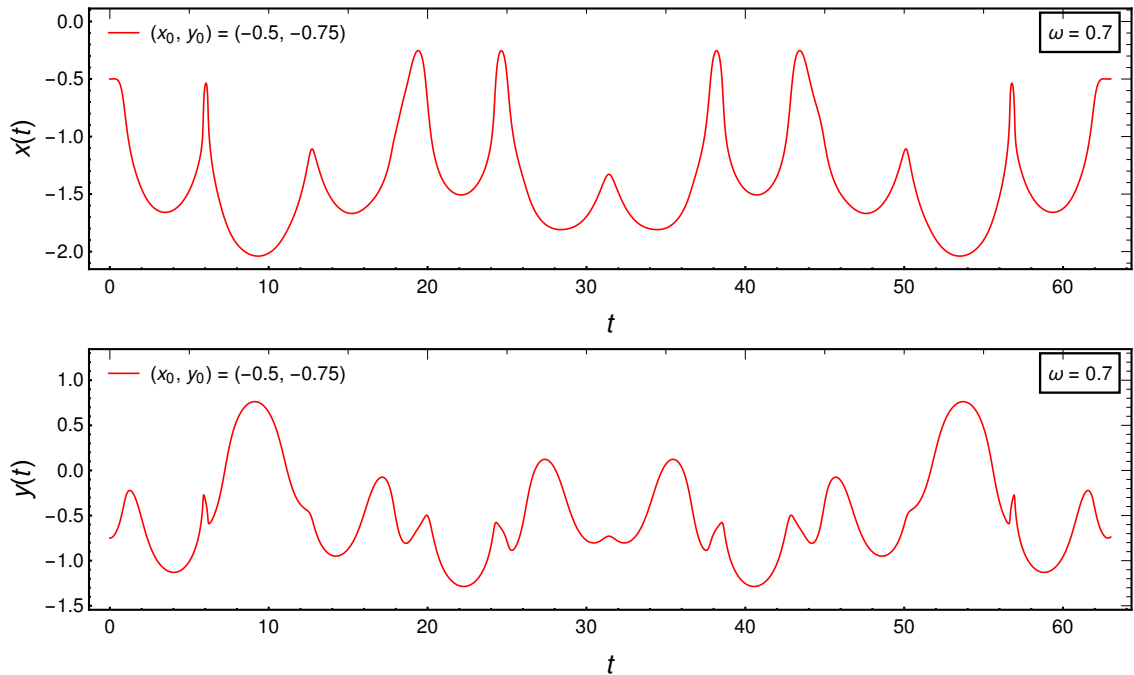


Figure 3.8: Evolution of  $x(t)$  and  $y(t)$  for the initial condition  $(x_0, y_0) = (-0.5, -0.75)$ . Note that, shortly after  $t = 30$ , the particle describes the reverse path in both spatial directions, such that the right side of each plot is a mirrored image of the left side.

method [155, 156] with a step size of  $10^{-4}$ , available within the `NDSolveValue` routine in *Mathematica* [157]. It is worth noting that the numerical calculation indicates a tendency of the system to exhibit regular or chaotic behavior, as it does not precisely give us the limit as  $t \rightarrow \infty$ , but only provides the value associated with a fixed time, which we assume to be much greater than the characteristic temporal parameters of the system under study. In our case, we calculated this value up to  $t = 10^4$ . For periodic trajectories, which do not exhibit exponential divergence, although the distance fluctuates over time, it is limited by an upper bound. Therefore, by the definition of the Lyapunov exponent (3.1),  $\lambda(t) \propto 1/t$ . In Figure 3.9, we plot the results of the computation of the Lyapunov exponent for all five initial conditions considered on a logarithmic scale. In all cases, a tendency curve with a slope of  $-1$  was observed, consistent with the expected asymptotic behavior. Consequently, we have that  $\lambda(t) = 0$ , indicating the absence of chaos.

In the case where  $\omega = 1/\sqrt{2}$ , on the contrary, we have a very different scenario with more complex and sparse trajectories due to the greater number of interactions with the NPXPC, as observed in Figure 3.10, where we plot the corresponding evolution of the Bohmian particles under the same initial conditions as in the  $\omega = 7/10$  case. It is important to highlight that these interactions do not always lead to chaotic behavior, as seen in the trajectories marked in black, green, and yellow. In the case of the central trajectory, an ordered behavior was expected since it is concentrated in a region where there is practically no influence of the nodal points. The trajectories in green and yellow, on the other hand, exhibit apparent order despite being in a region with a higher probability of

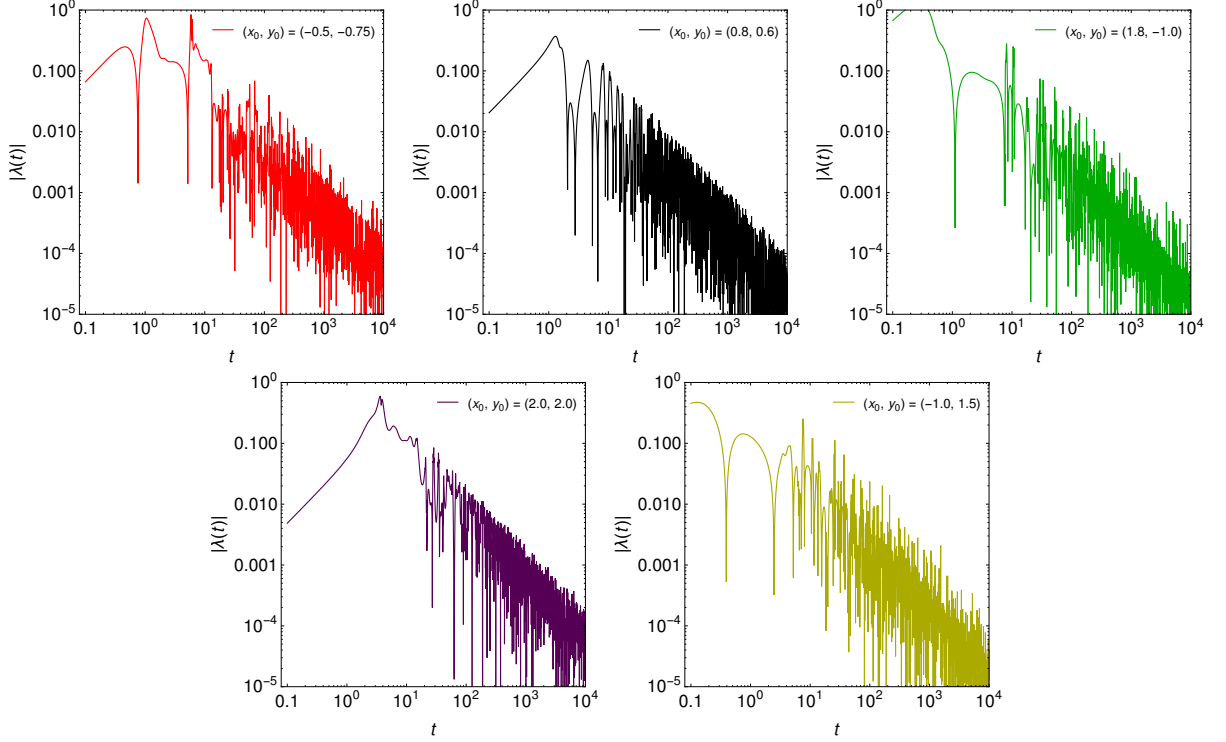


Figure 3.9: The absolute value of the Lyapunov exponent for the five initial positions considered in Figure 3.7, identified by color. In all the cases we observe a tendency curve such that  $\lambda(t) \propto 1/t$ , indicating ordered trajectories.

interactions. This can be explained, firstly, by the fact that these regions only indicate a probability of quantum particles being subject to the action of the NPXPC during their evolution, without a definitive assurance that such interaction actually occurs. For an effective approximation between the nodal point and the particles to occur, both must occupy positions close to each other in the configuration space in the same time interval. Moreover, this interaction needs to be effective and allow for the scattering of neighboring trajectories. Otherwise, they can be scattered in the same direction without an eventual separation. In Figure 3.11 we plot the individual position coordinates of two trajectories: one with an initial position of  $(x_0, y_0) = (-0.5, -0.75)$ , corresponding to the red curve in Figure 3.10, and the other starting very close to it, with  $x(0) = x_0 + \delta$  and  $y(0) = y_0 + \delta$ , where  $\delta = 10^{-4}$ . Although initially the trajectories remained quite close, as time passes their eventual separation became evident.

At last, in Figure 3.12, we compute the corresponding Lyapunov exponents. The black, green, and yellow curves indeed show ordered behavior. As for the red and purple curves, we observe a stabilization in the value of  $\lambda$ , corresponding to a positive exponent approximately equal to 0.03, which is an indicative of weakly chaotic behavior. As mentioned at the beginning of this section, the Lyapunov exponent is a local quantity that depends on the initial conditions, and different initial positions can yield different values of  $\lambda$ . This explains why we obtained  $\lambda = 0$  in some regions while in others  $\lambda = 0.03$ .

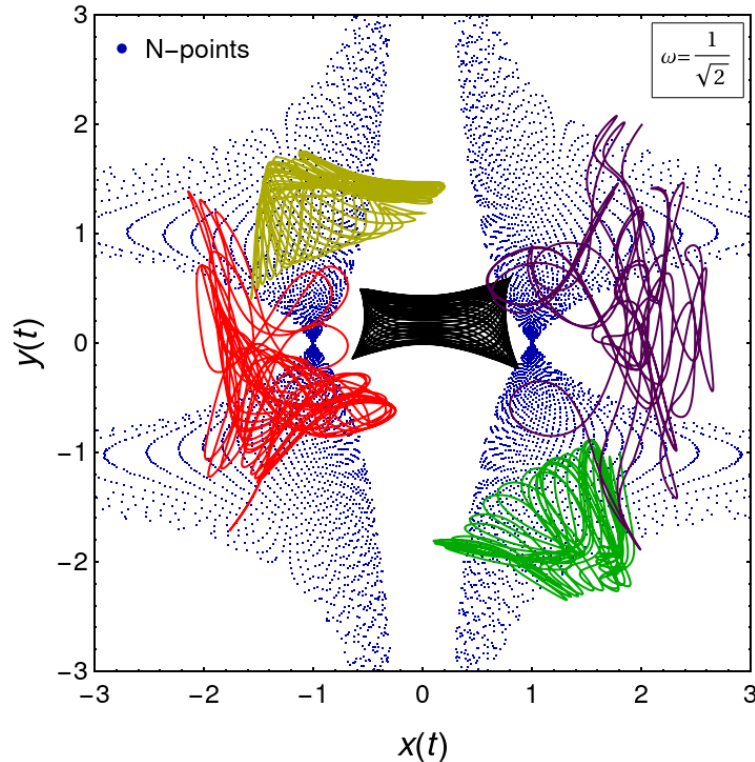


Figure 3.10: The quantum trajectories in configuration space for  $\omega = 1/\sqrt{2}$  up to a time of  $t = 150$ . We consider the same five initial conditions:  $(x_0, y_0) = (-0.5, -0.75)$  in red,  $(x_0, y_0) = (0.8, 0.6)$  in black,  $(x_0, y_0) = (1.8, -1.0)$  in green,  $(x_0, y_0) = (2.0, 2.0)$  in purple, and  $(x_0, y_0) = (-1.0, 1.5)$  in yellow. The dynamics of the black, green, and yellow curves are ordered, while the red and purple trajectories are chaotic.

In conclusion, even for a simple system such as the case of the two-dimensional anisotropic harmonic oscillator, we observe the emergence of a chaotic regime when imposing an irrational ratio between the oscillation frequencies along the  $y$  and  $x$  axes, respectively. It is noteworthy that, despite being a quantum system, the de Broglie-Bohm interpretation of quantum mechanics, through the calculation of Bohmian trajectories, allows us to use the same tools available for classical systems in studying chaos at quantum level. To be more precise, there is not much practical difference, according to this approach, between classical and quantum systems. Just as we investigate chaos in classical systems by calculating the Lyapunov exponent, we can study quantum chaos by numerically solving the associated equations of motion, which here have a natural nonlinearity due to the action of the quantum potential. Therefore, the use of Bohmian mechanics for this purpose is extremely advantageous. In the next example we consider the coupled two-dimensional anharmonic oscillator, where we investigate qualitative evidences of a chaotic regime.

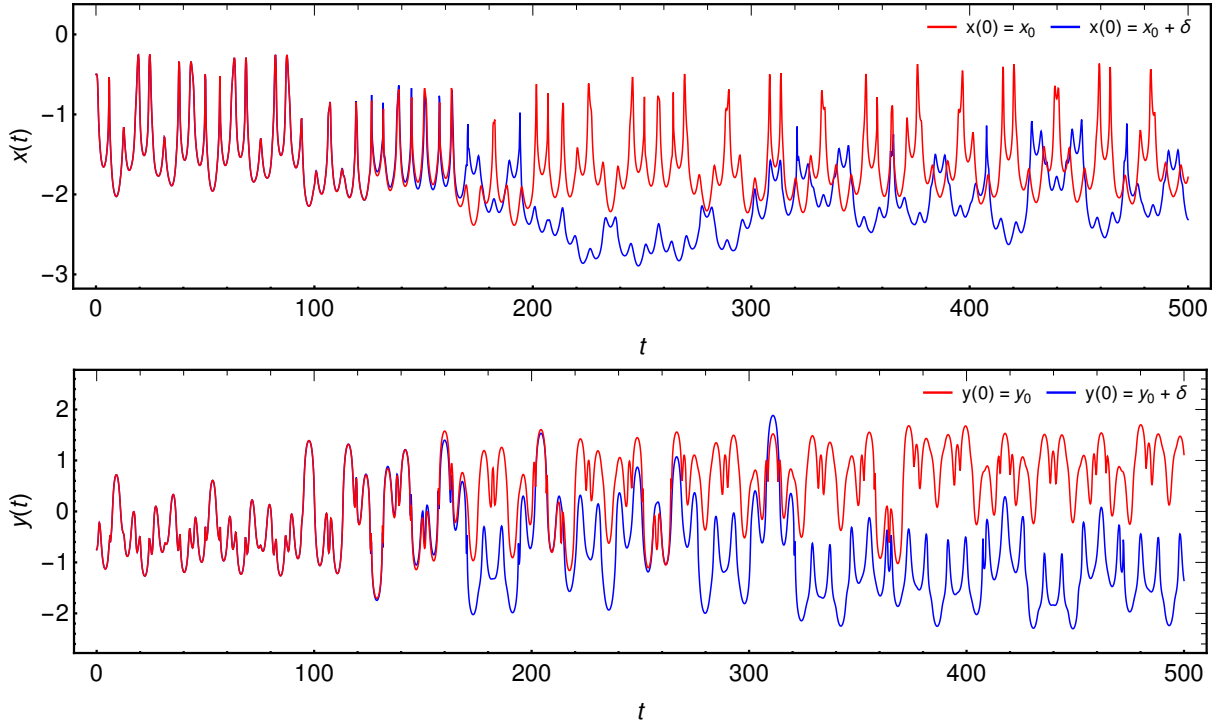


Figure 3.11: Evolution of  $x(t)$  and  $y(t)$  for two very close initial conditions, being  $(x_0, y_0) = (-0.5, -0.75)$  and  $\delta = 10^{-4}$ . We can see that as time passes the NPXPC promotes the effectively separation of the Bohmian particles.

### 3.3 The quantum anharmonic membrane

Now, let us consider the two-dimensional anharmonic oscillator with cubic and quartic terms, whose Hamiltonian is given by [3]

$$\mathcal{H} = \frac{p_x^2}{2m} + \frac{p_y^2}{2m} + \frac{1}{2}\omega^2 (x^2 + y^2) + \frac{\alpha}{3} (x^3 + y^3) + \frac{\beta}{4} (x^4 + y^4) - \kappa xy, \quad (3.26)$$

where  $\alpha$  and  $\beta$  are the anharmonicity strength constants and  $\kappa$  is the coupling constant that connects the two spatial coordinates. Therefore, the vibrations in the  $x$  and  $y$  directions are not independent. On the contrary, a perturbation in the  $x$  direction affects the dynamics associated with the  $y$  direction, and vice versa, simulating some type of quantum membrane. Note that in the case where  $\alpha \gg \beta$ , there is a high dominance region of the cubic term over the quartic one, which leads to unstable dynamics. To avoid this issue, we consider  $\alpha$  being larger than  $\beta$  only as a perturbation, ensuring the confinement of quantum particles by the potential defined by the quartic term. The Schrödinger equation, already in dimensionless variables, corresponding to this system is

$$-\frac{1}{2}\nabla^2\Psi + \frac{1}{2}\omega^2 (x^2 + y^2) \Psi + \frac{\alpha}{3} (x^3 + y^3) \Psi + \frac{\beta}{4} (x^4 + y^4) \Psi - \kappa xy\Psi = i\frac{\partial\Psi}{\partial t}. \quad (3.27)$$

Contrary to the previous example, in this specific case, we do not have knowledge of the

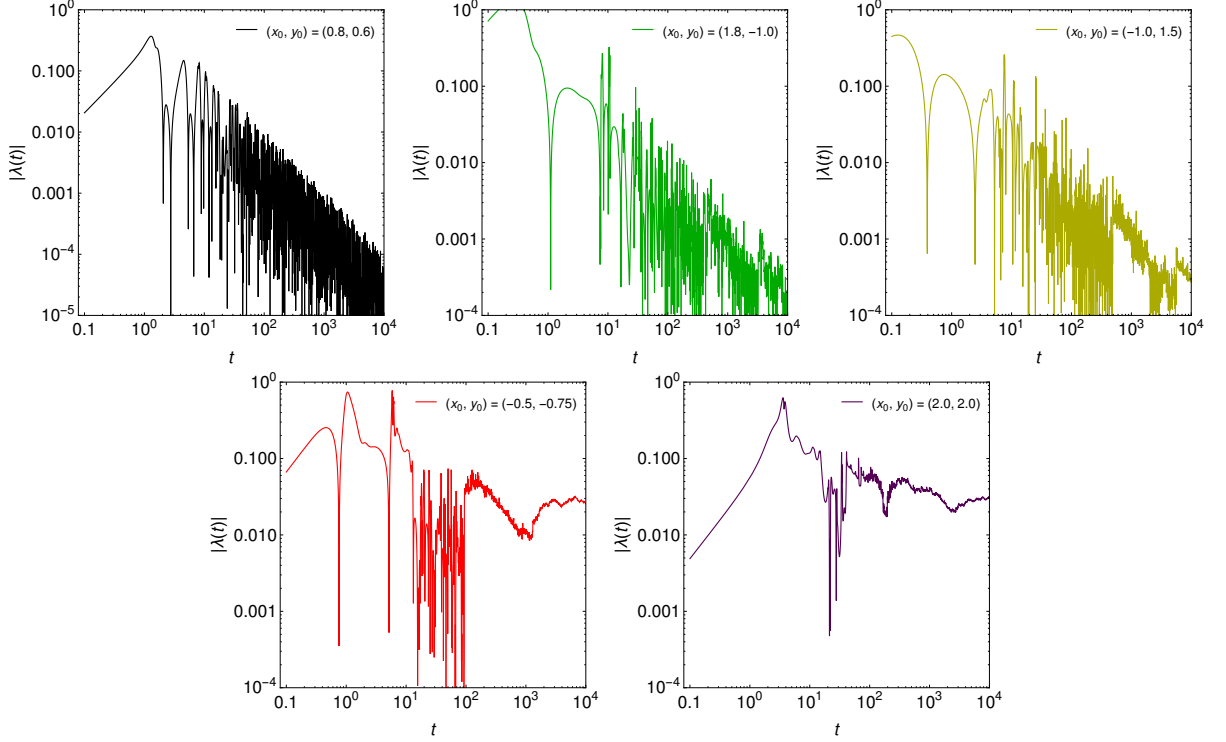


Figure 3.12: The absolute value of the Lyapunov exponent for the five considered situations, in logarithmic scale. As we can see, in the top three graphs we have ordered trajectories, with  $\lambda = 0$ . In the two cases below, the Lyapunov exponent reaches a saturation at  $\lambda = 0.03$ , implying a chaotic regime.

corresponding analytical expression for the solution of this equation. The most we could do in this situation is to consider both the anharmonic potential and the coupling term as small perturbations to the quadratic potential and construct solutions based on the known solutions of the quantum harmonic oscillator using perturbation theory. However, at the end of the day, we would have to compute the Bohmian trajectories associated with such solutions, which is done numerically due to the complexity of the correspondent equations. Thus, it becomes interesting, as we did for the numerical validation of the Ehrenfest theorem, to consider a completely numerical approach, which would allow us to explore a larger set of solutions. Such an analysis involves numerically solving the previously mentioned time-dependent Schrödinger equation, which is a highly non-trivial problem due to the dimensionality of the system. For numerical purposes, we consider as initial state a superposition of eigenstates of the quantum harmonic oscillator, given by the expression (3.7). Note that in a regime of negligible coupling and anharmonicity, we approximately have a two-dimensional quantum harmonic oscillator. We consider as initial wave function the sum

$$\Psi(x, y, 0) = \frac{1}{2} (\psi_{00} + \psi_{01} + \psi_{10} + \psi_{11}), \quad (3.28)$$

with same weight for all terms in the linear superposition. This choice of initial condition

is quite interesting because the Hamiltonian (3.26) is symmetric in the change of  $x$  and  $y$ , which is also verified for this particular wave function (see Figure 3.13). Thus, we expect this symmetry regarding the reflection with respect to the  $y = x$  line to manifest at some level within the calculation of the Bohmian trajectories.

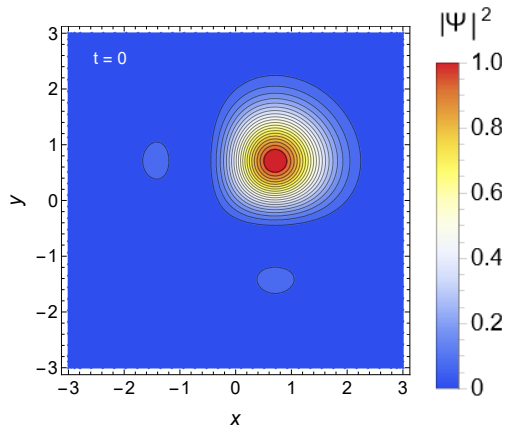


Figure 3.13: The contour plot of the initial probability density  $|\Psi(x, y, 0)|^2$ . Notice the symmetry referring to the change of the spatial variables.

Let us emphasize that obtaining an accurate and stable solution for the two-dimensional time-dependent Schrödinger equation is a highly nontrivial numerical problem that demands significant computational effort. Since our objective is to study chaotic systems through the integration of the guidance equations (3.2), it is crucial to have a precise solution for the wave function in order to minimize the propagation of errors and maintain stability over an extended period of time so that we can follow the evolution of the Bohmian particles. Thus, to solve the Schrödinger equation (3.27) with the initial condition (3.28), we employed a combination of various numerical methods. Firstly, we employed the Finite Element Method (FEM) [158, 159, 160] to discretize the spatial domain, considering a square lattice with size  $L = 5$ . More precisely, we considered the domain  $\mathcal{D} = [-L, L] \times [-L, L]$  and imposed Dirichlet boundary conditions  $\Psi(x, y, t)|_{\partial\mathcal{D}} = 0$  to avoid spurious effects resulting from the extrapolation of the wave function. The FEM is a powerful technique that involves subdividing a continuous domain into smaller finite-sized subdomains, where we obtain an approximated local solution. Connecting all these subdomains provides a global representation of the system. In our specific problem, the domain  $\mathcal{D}$  was discretized using a uniform square grid with a maximum cell size of  $l = 0.025$ .

In conjunction with the FEM, we employed the Method of Lines [40, 41] for temporal discretization. Finally, we utilized the BiConjugate Gradient Stabilized (BiCGSTAB) method [161, 162] to obtain the wave function within each cell. This method is highly effective in solving linear systems involving large sparse matrices. We integrated the transient part of the Schrödinger equation with high accuracy and precision, employing adaptive time steps in the process. By combining the FEM, the Method of Lines, and the BiCGSTAB solver, we obtained efficient and accurate solutions for relatively long times

while preserving the wave function's normalization with an error of  $10^{-3}$  throughout its evolution. In our simulations we use  $\alpha = 0.15$  and  $\beta = 0.16$  while we vary the value of the coupling constant.

In Figure 3.14, the numerical results obtained from solving the Schrödinger equation (3.27) with the initial condition (3.28) are represented in a contour plot of  $|\Psi(x, t)|^2$  for three distinct situations:  $k = 1.0$ ,  $k = 0.5$ , and  $k = 0.05$ . As can be seen the wave packet spreads during its evolution, due to the cubic potential and the coupling. When  $|x|, |y| > 1$ , the cubic term becomes highly unstable, allowing the system to escape the potential well. The presence of the quartic term in the Hamiltonian (3.26) is responsible for prevent such effect, avoiding excessive spreading and the stretching of the wave function into regions far from the origin. In fact, the evolution primarily takes place inside the region  $[-3, 3] \times [-3, 3]$ , exhibiting behavior significantly different from that of a typical quantum harmonic oscillator. It is worth noting that even at this level, the effect of the symmetry of both, the Hamiltonian and the initial condition, is observed in the change of the  $x$  and  $y$  variables. More precisely, the line  $x = y$  serves as a symmetry axis for all the figures, such that the region above this line is the mirrored image of the region below it. As expected, the evolution of the wave function follows the same symmetry present in the Hamiltonian and the adopted initial condition, supporting our numerical result.

Once in possession of the wave function, we calculate the evolution of the velocity field generated from the guidance equation (3.2). Due to the non-trivial form of the Hamiltonian in question, we obtain a much more complex velocity field than in the previous case, with the emergence of simultaneous vortices propagating in the configuration space. In Figure 3.15, obtained for  $\kappa = 0.1$ , we observe the presence of four dynamical vortices coexisting in a very close region, which eventually leads to their interaction. Over a short period of time, we notice two distinct events: first, we observe the creation of the two superior vortices at  $t = 2.8$ . After that, at  $t = 3.2$  we detect the approximation of the other two lower vortices and their subsequent collision, resulting in their disappearance. As we have stated, there is no reason for the velocity field not to be symmetric under the exchange of  $x$  and  $y$ . Thus, the eventual creation and annihilation of vortices must necessarily occur in pairs, which are equally distant from the symmetry axis  $y = x$  (gray line). Additionally, using the guidance equation together with the fact that  $\Psi(x, y, t) = \Psi(y, x, t)$ , we can see that the exchange of  $x$  and  $y$  implies a change in the sign of the vorticity (given by the  $\vec{\nabla} \times \vec{v}$ , with  $\vec{v}$  the velocity), while keeping the same absolute value. Therefore, each vortex of the pair will have the same diameter but spin in opposite directions, exactly as we observe. As a result, in both processes, the total final vorticity is zero. Since before the creation of vortices there is no vorticity, they originate in such a way that their combination results a null vorticity. Similarly, as a result of the collision, the final vorticity is also zero, consequently leading to the annihilation of the pair.

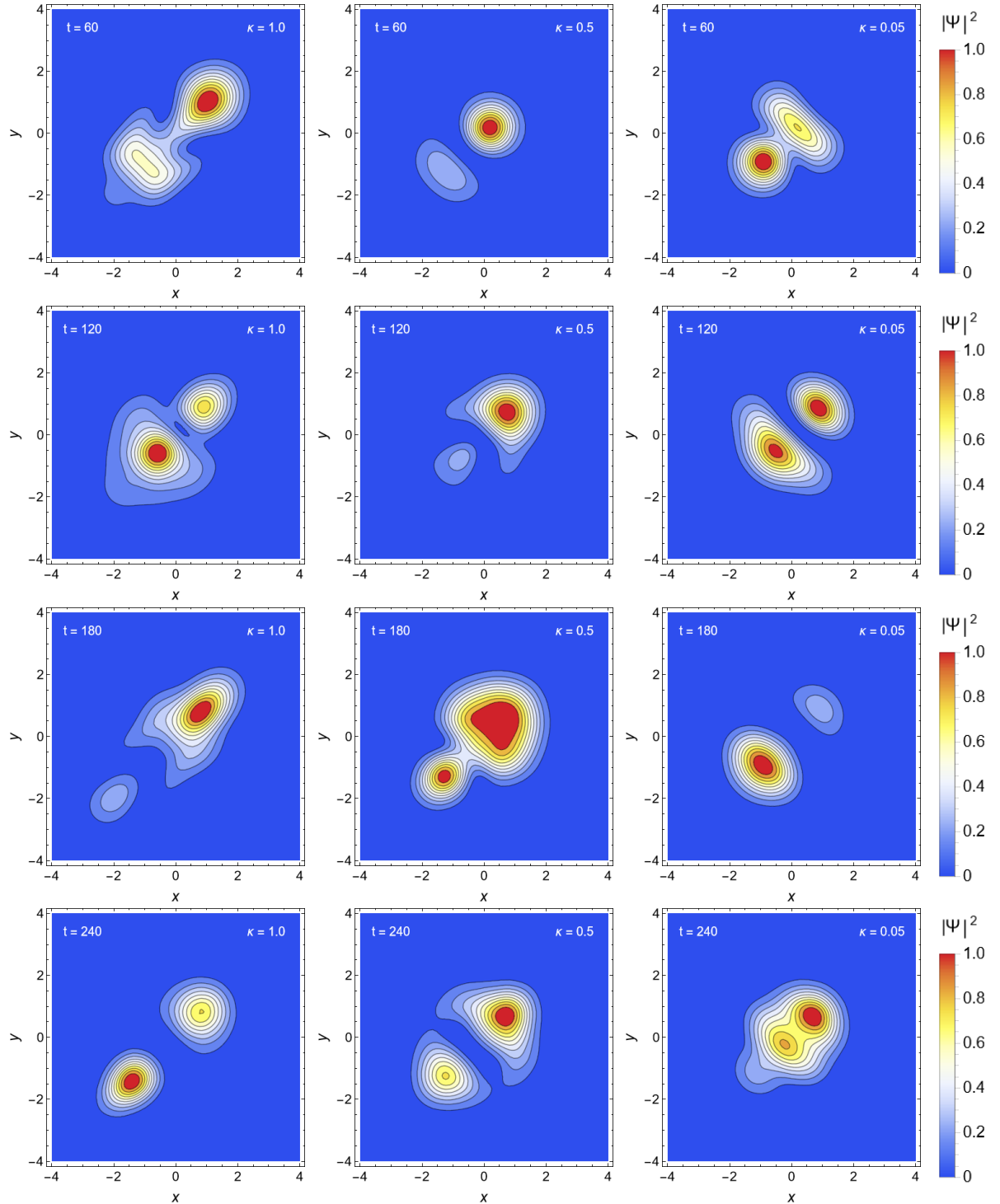


Figure 3.14: From top to bottom, we present the evolution of the probability density  $|\Psi(x, y, t)|^2$  at the moments  $t = 60, 120, 180, 240$ . We consider three different situations: from left to right, we have  $\kappa = 1.0, \kappa = 0.5$  and  $\kappa = 0.05$ . Due to the coupling, the spreading in  $x$  and  $y$  directions are connected, resulting in a dynamics resembling the movement of a membrane.

Due to the large number of nodal points in the system and their consequently fast appearance and subsequent dispersion, the Bohmian trajectories obtained from the numerical integration of the guidance equations are highly complex. In Figure [3.16](#), we plot

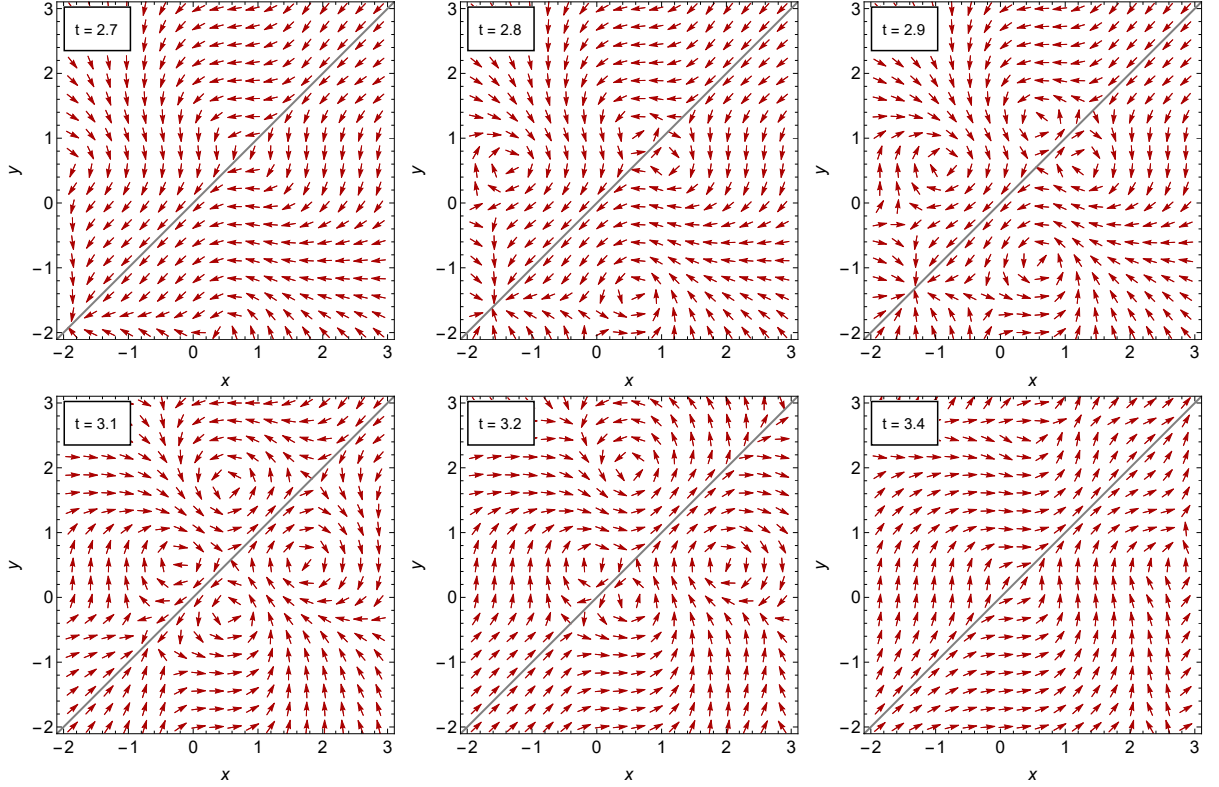


Figure 3.15: Evolution of the quantum vortices obtained for  $\kappa = 0.1$ . At  $t = 2.8$  we observe the formation of the two superior vortices. After formation, the pair start to deviate from the symmetry axis  $y=x$ , represented in gray. At  $t = 3.2$  we notice the collision of the two inferior vortices, causing their eventual annihilation. Due to the symmetry, each vortex of the pair spins in opposite directions.

four trajectories for each of the cases presented in Figure 3.14, corresponding to different values of the coupling constant. Similarly to before, we utilized the eighth-order fixed-step Runge-Kutta method [155, 156] with a step size of  $0.5 \times 10^{-5}$ . As we can notice, decreasing the value of  $\kappa$  implies an increase in the degree of ordering. For  $\kappa = 1.0$ , is evident the unpredictability of the associated trajectories, since they occupy a significant part of the configuration space. Conversely, when  $\kappa = 0$ , which is equivalent to removing the coupling, the system looks like ordered, with the quantum particles confined to a small region. This comparison shows the crucial role of the coupling constant in inducing chaotic behavior. For the uncoupled case, even keeping the cubic term, which is responsible for bring instabilities to the system, we have an apparent ordered pattern.

It is important to note that to obtain these trajectories, first we numerically solved the time-dependent Schrödinger equation, then we calculated the velocity field based on this solution, and finally we integrated it to obtain the particle positions. Thus, we performed three sequential numerical procedures, which may introduce potential error propagation. However, as we can observe in the figures, the symmetry corresponding to the change of the spatial variables is still preserved even at the level of the quantum trajectories, reinforcing the effectiveness of the adopted numerical procedure.

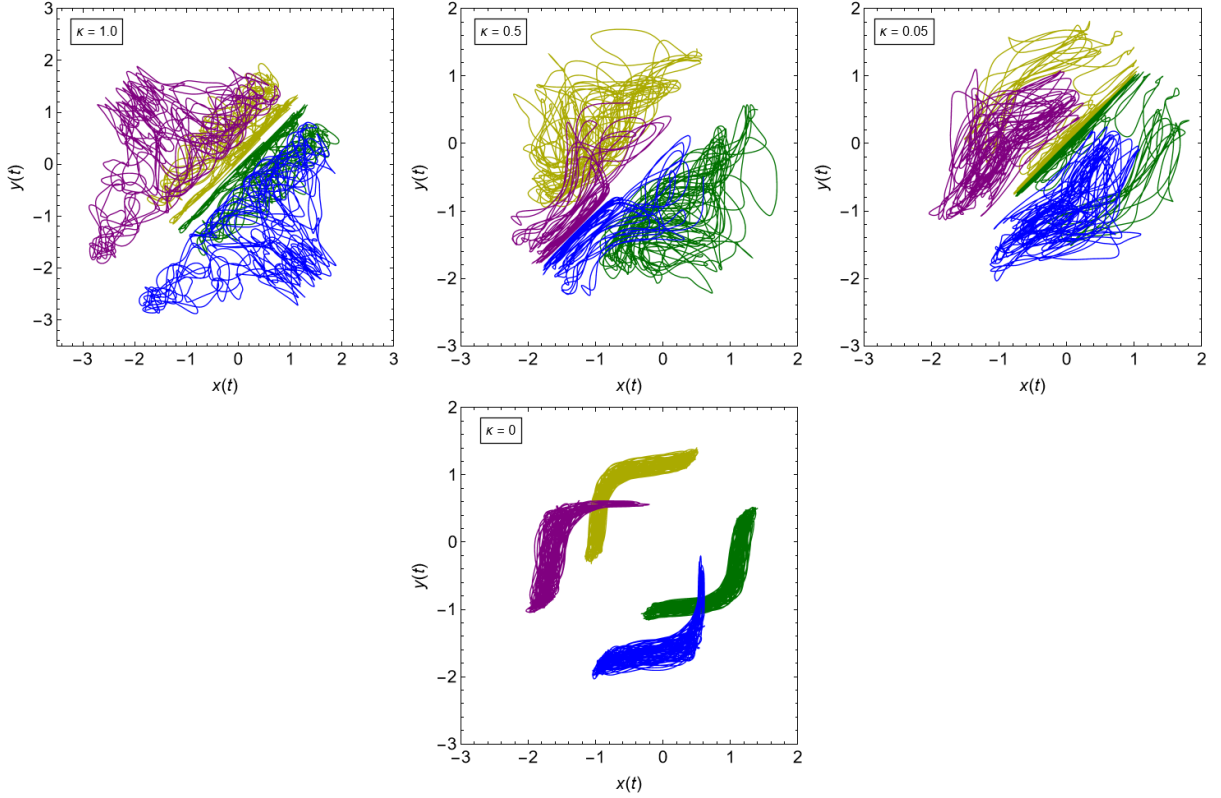


Figure 3.16: The quantum trajectories obtained considering  $\kappa = 1.0, 0.5, 0.05, 0$ . As initial conditions we take  $(x_0, y_0) = (1.4, 0.5)$  in green,  $(x_0, y_0) = (0.5, 1.4)$  in yellow,  $(x_0, y_0) = (0.6, -0.5)$  in blue, and finally,  $(x_0, y_0) = (-0.5, 0.6)$  in purple. In all the plots, the two lower trajectories are the mirrored images of the upper two.

In order to examine the divergence of initially neighboring trajectories, we plotted, in Figure 3.17, the graph corresponding to very close initial conditions. We consider three trajectories in total, one at  $(x_0, y_0) = (0.6, -0.5)$ , another with a distance of  $10^{-4}$  in the  $x$  coordinate, and the last one with a distance of  $10^{-4}$  in the  $y$  coordinate. We notice that initially the particles move practically together, but as time passes, they start to demonstrate significant differences in their trajectories as a consequence of the nonlinear dynamics. Additionally, due to the coupling and the dependence of the velocity field on both spatial coordinates (equation 3.2), we observe a consequent divergence in both the  $x$  and  $y$  components, even considering a difference in just one of them at the beginning.

To demonstrate the chaotic nature associated with this quantum system, we compute the average of the quantity  $\xi(t) = \tilde{\xi}(t)/\tilde{\xi}(0)$ , where  $\tilde{\xi}(t) = \sqrt{(\delta x)^2 + (\delta y)^2 + (\delta p_x)^2 + (\delta p_y)^2}$  is the distance, in phase space, associated with neighboring trajectories for different initial conditions. As we have seen in the previous example, this is a quantity that varies from point to point in the initial phase space, such that different positions lead to distinct outcomes. Therefore, the average corresponding to different values of  $\xi(t)$ , presented in Figure 3.18 for a total of 60 initial conditions (with other 60 separated by an amount of  $10^{-4}$ ), provides a more accurate measure of the chaotic tendency of a given system.

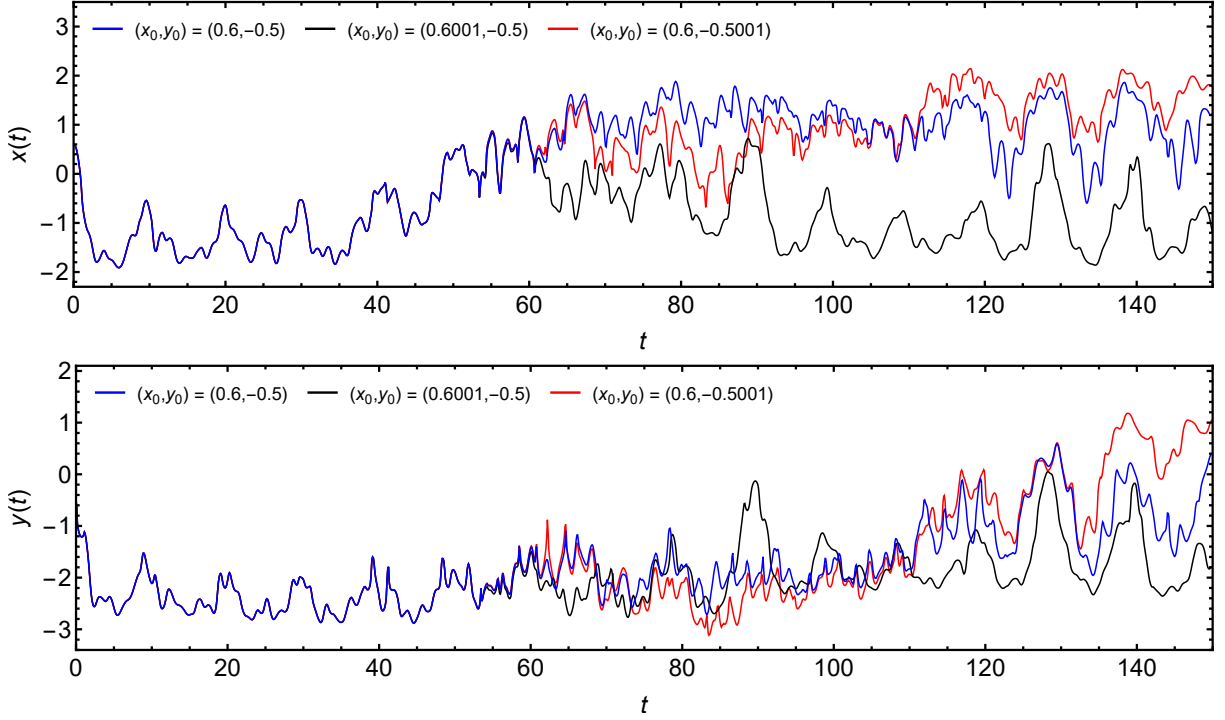


Figure 3.17: Plot evidencing the sensitivity to initial conditions. We plot three trajectories with very close initial conditions, at a distance of  $10^{-4}$ . Initially, the positions of the particles are nearly identical, but as time passes we have a significant deviation in both spatial dimensions.

Another important point is that due to the computational effort involved in numerically solving the time-dependent Schrödinger equation, we computed the results only up to time  $t = 300$ , which prevents exact stabilization. However, we can clearly observe in the left plot an increasing tendency in the curves referring to  $\kappa = 1.0$ ,  $\kappa = 0.5$ , and  $\kappa = 0.05$ , which indicates a positive slope, and, as a result, a positive Lyapunov number. Thus, we can affirm that this system is, indeed, chaotic. The curve obtained for  $\kappa = 0$ , on the other hand, oscillates around a constant value, not indicating an exponential deviation of trajectories, which is indicative of ordered behavior. To be more precise, the decreasing in the coupling strength, measured by  $\kappa$ , implies in a weaker degree of deviation, what was a expected feature anticipated from Figure 3.16. Even with the anharmonic nature of the oscillations, a null coupling results in two independent motions, incapable of generating chaotic dynamics since the adopted frequency in both axes is the same. In this situation, instead of having a quantum membrane, we have an isotropic anharmonic oscillator. Therefore, the eventual decrease in the constant  $\kappa$  implies a weaker chaotic dynamics, as observed in Figure 3.18.

Additionally, as stated earlier, because the Bohmian interpretation allow us to discuss the trajectories of the quantum particles, quantum and classical chaos can be seen as two sides of the same coin according to this view. Therefore, it becomes interesting to investigate how the system behaves when we vary the value of  $\hbar$ , which can be achieved

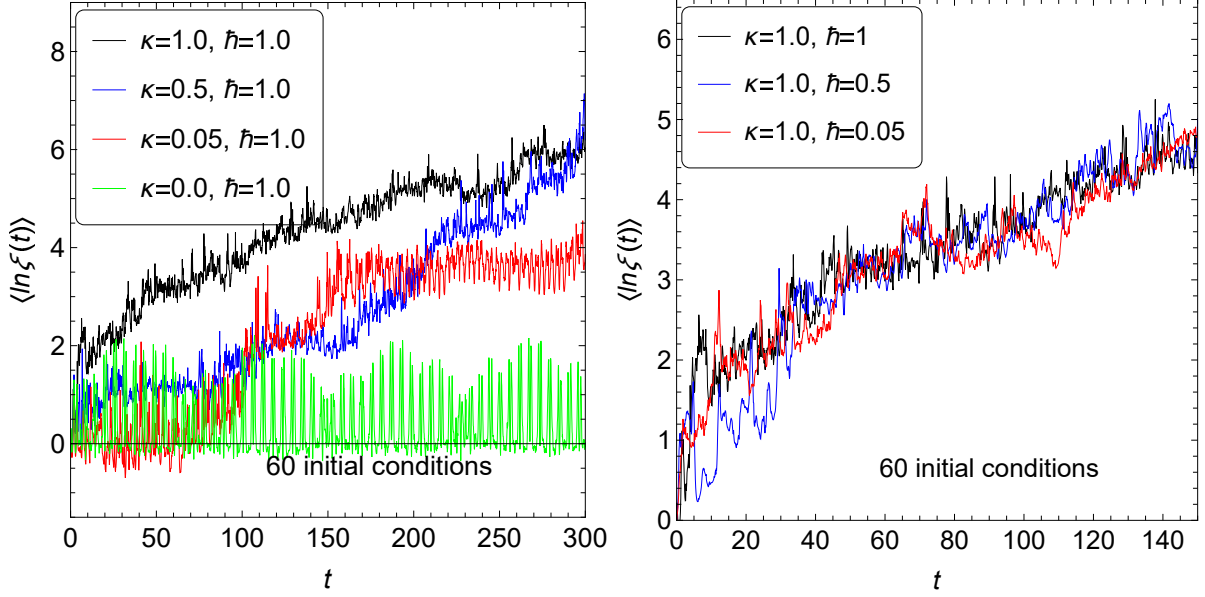


Figure 3.18: In the left, the plot of  $\langle \ln \xi(t) \rangle$  versus  $t$  for  $\kappa = 1.0, 0.5, 0.05, 0$  and  $\hbar = 1.0$ . We consider a total of 60 initial conditions regularly spaced in the interval  $(x_0, y_0) \in [-1.5, -1.1] \cup [1.1, 1.5]$ . In the right, a similar plot, but considering  $\kappa = 1.0$  and  $\hbar = 1.0, 0.5, 0.05$ , for a average computed with 60 initial conditions regularly spaced in the interval  $(x_0, y_0) \in [-0.5, -0.1] \cup [0.1, 0.5]$ .

by modifying the Planck's constant in the Schrödinger equation (3.27). For this purpose, we fix the value of the coupling constant at  $\kappa = 1.0$  and perform the same numerical procedures, varying the value of  $\hbar$  instead. We consider three scenarios:  $\hbar = 1.0$ ,  $\hbar = 0.5$ , and  $\hbar = 0.05$ . In the right plot of Figure 3.18, we present the average of  $\xi(t)$  for these three cases. Similar to before, we observe an increasing tendency for all three values, indicating a positive Lyapunov exponent and, consequently, a propensity towards chaotic behavior. The difference is that, unlike the previous case where the decrease in the value of  $\kappa$  resulted in a decrease in the degree of separation between the trajectories, for the three considered values of  $\hbar$  we observed the same behavior, with oscillations around the same tendency curve. Although we cannot guarantee with complete certainty that the classical limit is attained in the regime where  $\hbar \rightarrow 0$  [32] (the assurance of obtaining classical trajectories from the quantum analogues occurs in the limit where the quantum potential goes to zero), this analysis is important because it shows that in this specific model, the transition from considering values of  $\hbar$  close to unity to low values of  $\hbar$  barely affects the chaotic behavior of the system within the considered time interval. For larger values of  $t$ , there is likely to occur a stabilization at different values, but this fact does not affect the qualitative result of having a positive Lyapunov exponent and consequent chaotic dynamics.

Therefore, as a conclusion, we can assert that this model for the anharmonic quantum membrane exhibits chaotic dynamics, once again proving the presence of quantum chaos through an analysis based on the de Broglie-Bohm interpretation of quantum mechanics.

This tendency was observed when varying the coupling constant  $\kappa$  and varying the value of  $\hbar$  as well. Thus, even for complex systems like the one under consideration, we are capable of employing the same techniques used in the study of classical chaos at the quantum level, obtaining the Lyapunov exponent from the numerical solution of the time-dependent Schrödinger equation and from the guidance equations. As a future perspective, we intend to improve the numerical approach with the objective to obtain values of the Lyapunov exponent for longer time intervals. This will allow us to explore the effects of chaotic dynamics in situations outside the quantum equilibrium and how they may lead us to obtaining the Born rule. Another objective would be the study of classical systems whose chaotic dynamics leave imprints on their quantum counterparts. If we are able to obtain classical mechanics from Bohmian interpretation, could it be that chaos at quantum level is actually responsible for leaving traces on classical systems, rather than the other way around?

# Chapter 4

## Concluding Remarks

The Bohmian interpretation of quantum mechanics brings enlightening discussions about quantum reality and finds useful applications in various areas, ranging from statistical mechanics to quantum field theory. In this first part, we provide a brief overview of the subject, exploring the potential to study quantum phenomena from a classical perspective. The introduction of the guidance law enables us to interpret the Schrödinger equation as a Hamilton-Jacobi equation along with a continuity equation, endowing the wave function with both a dynamic and probabilistic role.

To illustrate these features, we examine the case of the simple harmonic oscillator. We have developed a numerical procedure to derive Bohmian trajectories from the numerical solution of the Schrödinger equation. This method facilitates the investigation of more complex systems that lack an analytical expression for the wave function. As examples, we explore the driven harmonic oscillator subjected to various types of forces, with a particular focus on Gaussian and oscillatory impulses.

In the Gaussian scenario, the initial and final states correspond to the simple harmonic oscillator case. However, the impulse is responsible for transferring energy to the system, exciting additional eigenstates. This effect was observed in the Bohmian trajectories as an increase in the amplitude of the oscillations and the expansion of the phase space volume. In the case of the oscillatory force, we observe the combined effect of two different types of oscillations: the natural oscillation of the system and the induced oscillation due to the external force. When the natural frequency was equal to the frequency of the oscillatory signal, we observed the phenomenon of quantum resonance in the Bohmian trajectories. This was marked by a continuous expansion of the trajectories amplitudes and the phase space volume.

A natural extension of this problem is the Duffing oscillator, which, in addition to the sinusoidal force, also takes into account the effect of a quartic interaction. For low values of the anharmonicity parameter, the Bohmian trajectories exhibit a beat-like phenomenon. This occurs because the anharmonic perturbation slightly alters the natural frequency, a change that is more pronounced for regions farther from the origin.

Once the quantum trajectories are obtained, we calculate the averages of the position and the momentum of the quantum particles, showing that the mean values mimic classical laws of motion, but with the amplitude of the oscillations and the volume of the phase space related to Bohmian averages depending on quantum properties. This quantum-classical treatment of particle trajectories aligns with the Ehrenfest theorem, as illustrated in the figures presented throughout Chapter 2.

On Chapter 3 we discussed a more complex topic: the quantum chaos from the point of view of Bohmian Mechanics. We show that it is possible to address this issue without making any reference about the energy levels or the discrete nature of the quantum observations. Instead, we employed the quantum trajectories approach to calculate the Lyapunov exponent, which quantifies the degree of separation between neighboring trajectories. It's important to note that this approach aligns with the method used to study chaos at the classical level. Consequently, Bohmian mechanics allow us to view classical and quantum chaos as two facets of the same phenomenon, with the latter distinguished from the former by the presence of the nonlinear quantum potential. In fact, the analogy between classical and quantum equations of motion, exemplified by Newton's equation, vividly illustrates that particle trajectories can exhibit nonlinear behavior during their evolution in both regimes, a critical aspect in the study of chaos.

We have reviewed the primary mechanism responsible for generating chaotic behavior at the quantum level, namely, the dynamic formation of vortices through Nodal-Points-X-Points-Complexes (NPXPCs). We have observed that the presence of these geometric structures promotes the divergence of neighboring trajectories, potentially resulting in exponential divergence. In the context of the anisotropic two-dimensional harmonic oscillator example, we have noted that in the case of irrational frequency ratios, NPXPCs have a broader range of influence compared to the rational case, with the NPXPC trajectory occupying a more extensive region in configuration space. We have computed the Bohmian trajectories and, consequently, the Lyapunov exponent. For  $\omega = 7/10$ , we have observed ordered behavior. However, for  $\omega = 1/\sqrt{2}$ , we have noticed the coexistence of both ordered and chaotic trajectories, with a non-zero Lyapunov exponent in the latter case indicating a weak chaotic behavior.

Finally, we study the two-dimensional coupled anharmonic oscillator featuring cubic and quartic interactions with the objective to observe evidences of chaos. Due to the inherent complexity of this system, we have developed a numerical procedure to solve the 2D Schrödinger equation and obtain Bohmian trajectories over relatively long periods with high precision and stability. In this example, we have observed the dynamic formation and subsequent annihilation of vortices, resulting in highly intricate Bohmian trajectories. Notable chaotic features have been identified in the quantum trajectories, including compactness, unpredictability, sensitivity to initial conditions, and a positive Lyapunov number, all confirming the presence of robust chaos in both limits,  $\hbar = 1$  and

$\hbar \rightarrow 0$ . Remarkably, in the absence of coupling ( $\kappa = 0$ ), chaos disappears, underscoring its crucial function in inducing the emergence of vortices and driving chaotic behavior.

In conclusion, the results presented here can be used as a point of departure in the study of more intricate systems, since the numerical methods provide the Bohmian trajectories without the necessity of using an analytical expression for the wave function. For instance, we can investigate condensed matter phenomenons in the mean-field approximation within this approach. Another possibility, with applications in quantum information, is the study of entangled Bohmian systems, with the numerical methods we used being a promising path on this investigation. Regarding the quantum equilibrium hypothesis, we may wonder what is the effect in considering an initial probability distribution that is not given in terms of Born's rule in the quantum-classical relations obtained for the average values, especially the ones referring to the position and momentum of the quantum particles. Additionally, it is known that chaotic dynamics is a critical component in validating Born's rule for these types of systems. Hence, exploring systems of this nature for further study becomes an intriguing avenue of research. Finally, in the future, we aim to delve deeper into understanding the intricate dynamics of the quantum-to-classical transition in chaotic scenarios, with a focus on elucidating the role of the quantum potential in this process.

## Part II

# Quantum Field Theory and the Unruh effect: A Bohmian approach

# Chapter 5

## Introduction

Quantum gravity remains one of the most captivating challenges in current theoretical physics, with numerous endeavors in its understanding. Despite the inherent difficulty in constructing a quantum theory for the gravitational field, one plausible approach to comprehend how quantum effects emerge in gravitational theories is to consider a quantum field theory in curved spacetimes, where significant phenomena such as cosmological particle production in an expanding universe and Hawking radiation take place.

Within this scenario, the concept of particles as field excitations from a vacuum state is reference-frame dependent. As an example of such a phenomenon, we can cite the well-known Unruh effect [163, 164, 165], which yields similar results to those obtained from a Schwarzschild geometry [166, 167] through much simpler calculations.

In order to illustrate such effect we can consider a free scalar field in a flat 2-dimensional Minkowski space from two different perspectives: according to an inertial frame and according to a Rindler observer, uniformly accelerated in relation to the first one. It turns out that the vacuum state for both observers is different. While for the inertial observer, the vacuum state is  $|0\rangle_M$ , for the Rindler observer, it is actually  $|0\rangle_R$ . Consequently, the number of particles defined as excitations of  $|0\rangle_M$  and  $|0\rangle_R$  respectively, are different, as expected by quantum field theory. More precisely, the state of zero particles defined in the inertial reference frame corresponds to a Bose-Einstein distribution for the Rindler observer, with temperature<sup>1</sup>

$$T = \frac{\hbar a}{2\pi\kappa_b c}, \quad (5.1)$$

proportional to the acceleration  $a$ . This is an important result that relates three important constants in physics: the Planck's constant  $\hbar$ , the Boltzmann's constant  $\kappa_b$  and the speed of light  $c$ . While a captivating phenomenon, its observation is considerably challenging. As a rough estimation of its scale, to achieve a temperature of  $1K$ , an acceleration on the order of  $10^{19}m/s^2$  is required. Nevertheless, experimental observations are discussed in

---

<sup>1</sup>A similar result can be obtained if we consider fermions instead of a scalar field. In this case we obtain a Fermi-Dirac distribution with the same temperature [168, 169].

[170, 171, 172, 173, 174], whereas for Hawking radiation see [175, 176, 177, 178, 179].

Usually, to obtain the Unruh temperature (5.1), we expand the field in terms of the mode solutions obtained from the equations of motion. With this expansion, we obtain the creation and annihilation operators, from which we define the vacuum state and its respective excited states. However, it is important to note that this expansion, in general, depends on the reference frame we are considering, as different frames can lead to different equations of motion. By connecting both expansions, in Rindler and Minkowski frames, through Bogoliubov transformations, it is possible to calculate the expectation value of the number operator, defined in the Rindler frame, in the Minkowski vacuum. Such calculation gives us the Bose-Einstein distribution with the mentioned temperature. This is the standard approach, reviewed for example in the works [180, 181, 182], and uses the Heisenberg picture of quantum mechanics in the framework of the usual interpretation. Additionally to this fact, it is known that there is a kind of entanglement between the left and right Rindler wedge fields [183], which is hard to explain due the locality inherent to quantum field theory. Therefore, since Bohmian mechanics is manifestly non-local, could be interesting to address this phenomenon according to this interpretation.

In the relativistic Bohmian approach of the quantum field theory the element of objective reality are the fields that represents the particles [31, 32, 184, 185]. With the aim of obtain a guidance law like in the non-relativistic case it is usual to use the Schrödinger representation of the fields [186], where we substitute the particle trajectories by field trajectories, being the velocity field the canonical conjugated momentum. In this context, the quantum potential is responsible for the quantum interactions between the bosonic fields and matter, as the result of its non-linear and non-local nature [187, 188, 189, 190].

Following this lines of investigation, in this chapter we explored the Unruh effect using the de Broglie-Bohm framework, where from the Minkowski vacuum wave functional in Rindler spacetime [191] we obtained the guidance equations and, as consequence, the Bohmian field trajectories. Within this formalism, we were able to separate the quantum and classical contributions to the total energy and the temperature associated effects through the computation of the Bohmian averages. For this purpose, in a first moment we will introduce the Unruh effect in the standard interpretation. After that we intend to give a concise introduction to the Schrödinger picture in the context of quantum field theory. Then, we will present the principal results regarding the Bohmian version of the Klein-Gordon theory and review relevant aspects concerning the wave functional for a massless scalar field in the right Rindler wedge. Following this, we plan to present the associated de Broglie-Bohm theory, calculating the field trajectories and also the power spectrum, studying the regimes of low and high accelerations. Finally, we will investigate the complete manifold problem, extending our findings to the left Rindler wedge as well. We carry out the same calculations and asymptotic expansions. By doing so, we pretend to address the entanglement problem with the help of the non-local nature of guidance

equations, potentially paving the way for the black hole analysis.

# Chapter 6

## The Unruh effect from a Bohmian perspective

### 6.1 The Unruh effect in the standard approach

In the context of a two-dimensional Minkowski flat spacetime, we can mimic the effect of a curved geometry by considering the trajectory of an observer with a constant acceleration  $a$  and with coordinates  $(t, x)$  in some Minkowski inertial frame. We can describe its trajectory through the Rindler transformations [\[180, 181, 182, 192, 193\]](#)

$$\begin{aligned}x(\tau, \xi) &= \frac{e^{a\xi}}{a} \cosh(a\tau), \\t(\tau, \xi) &= \frac{e^{a\xi}}{a} \sinh(a\tau),\end{aligned}\tag{6.1}$$

where  $\tau$  and  $\xi$  represent the Rindler coordinates, taking values from  $-\infty$  to  $\infty$ . Here,  $\tau$  takes the role of a temporal variable, while  $\xi$  represents the spatial one.

The effect of the Rindler spacetime  $(\tau, \xi)$  is very similar to the Schwarzschild geometry. From equation [\(6.1\)](#), we can observe that  $-x < t < x$ . Consequently, these transformations are valid only in region I of the Minkowski spacetime, as indicated in the diagrams presented in Figure [\(6.1\)](#). The curves  $t = \pm x$ , in red, act as horizons, being reached as  $\tau \rightarrow \pm\infty$ , while the origin is attained when  $\xi \rightarrow -\infty$ . In Rindler coordinates, a Rindler observer is just an observer who moves along a constant parameter  $\xi$ , which corresponds to the hyperbolas  $x^2 - t^2 = \frac{e^{2a\xi}}{a^2}$  in Minkowski space, represented by the yellow curves in the left diagram. Initially, the observer is located at  $x \rightarrow \infty$ , approaching the origin as time passes, reaching a minimum distance at  $t = \tau = 0$ , after which the observer starts moving away again until  $x \rightarrow \infty$ . As we change the value of the parameter  $\xi$ , we change the point of closest proximity to the origin, in such a way that each hyperbola corresponds to a different Rindler observer. On the other hand, the yellow dashed lines are hypersurfaces with constant value of the temporal variable  $\tau$ , implying constant foliations in

proper time.

Considering that the line element of the Minkowski space is  $ds^2 = -dt^2 + dx^2$  and using equation (6.1), we obtain the line element of the Rindler spacetime, which is  $ds^2 = e^{2a\xi}(-d\tau^2 + d\xi^2)$ , revealing a conformal invariance between both metrics, with a conformal factor of  $e^{a\xi}$ . Additionally,  $\partial_\tau = a(x\partial_t + t\partial_x)$  is a Killing vector in Rindler spacetime, where to obtain the expression related to  $\partial_\tau$  we invert relation (6.1) and we use the chain rule. In fact,  $\partial_\tau$  is a timelike Killing vector associated with temporal translations, given that  $(\partial_\tau)^\mu(\partial_\tau)_\mu = -[(\partial_\tau)^t]^2 + [(\partial_\tau)^x]^2 = a^2(-x^2 + t^2) < 0$  in region I. Additionally, we can see from the Rindler transformations (6.1) that as we increase the value of  $\tau$ , we also increase the value of  $t$ , indicating that both temporal variables evolve in the same direction, as shown in Figure (6.1). Furthermore, the lines  $t = \pm x$  are called the Killing horizons, in which  $(\partial_\tau)^\mu(\partial_\tau)_\mu = 0$ .

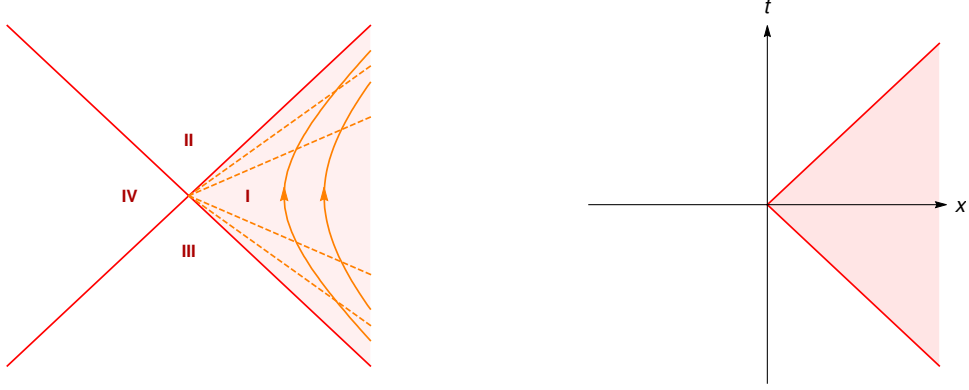


Figure 6.1: Diagram of the Rindler spacetime. The Rindler transformations are valid only in the region I of Minkowski space, where  $-x < t < x$  and  $x > 0$  (shaded area). The thick curves represent the trajectories of a Rindler observer in Minkowski space, while the dashed lines denote the hypersurfaces of constant parameter  $\tau$ . The temporal evolution of the parameter  $\tau$  is indicated by the yellow arrows, pointing in the same direction as  $t$ .

In what follows let us consider a real massless scalar field with action

$$S = \frac{1}{2} \int dt dx \left\{ \left( \frac{\partial \phi}{\partial t} \right)^2 - \left( \frac{\partial \phi}{\partial x} \right)^2 \right\} \quad (6.2)$$

in Minkowski space. From the extremization of  $S$ , we obtain the Klein-Gordon equation of motion

$$\left( -\frac{\partial^2}{\partial t^2} + \frac{\partial^2}{\partial x^2} \right) \phi(t, x) = 0, \quad (6.3)$$

which admits as mode solutions

$$u_k(t, x) = \frac{1}{\sqrt{4\pi\omega_k}} e^{i(kx - \omega_k t)}, \quad (6.4)$$

where  $\omega_k = |k|$  and  $k$  is a continuous index that labels the solutions. Conventionally,  $k$  is interpreted as the wave number, while  $\omega_k$  represents the frequency. The  $u_k$  modes correspond to positive frequency modes (p.f.m.) with respect to  $t$ , such that they are eigenfunctions of  $\partial_t$ , that is,  $\partial_t u_k = -i\omega_k u_k$ . Analogously,  $\partial_t u_k^* = i\omega_k u_k^*$ , establishing the  $u_k^*$  modes as negative frequency modes (n.f.m.).

Defining the Klein-Gordon inner product acting in the solution space

$$(\phi_1, \phi_2)_M := i \int_{\Sigma} dx \left( \phi_1^* \frac{\partial \phi_2}{\partial t} - \phi_2 \frac{\partial \phi_1^*}{\partial t} \right), \quad (6.5)$$

with  $\Sigma$  a Cauchy hypersurface specifying a hyperplane of simultaneity at a constant time, we can see from (6.4) that  $\{u_k, u_k^*\}$  form a normalized orthogonal basis according to (6.5), since

$$\begin{aligned} (u_k^*, u_{k'})_M &= 0, \\ (u_k, u_{k'})_M &= \delta(k - k'), \\ (u_k^*, u_{k'}^*)_M &= -\delta(k - k'). \end{aligned} \quad (6.6)$$

So, in order to quantize the system we promote the scalar field  $\phi$  to an operator and we impose the canonical commutation relations at equal times<sup>1</sup>

$$\begin{aligned} [\phi(t, x), \phi(t, x')] &= 0, \\ [\Pi_{\phi}(t, x), \Pi_{\phi}(t, x')] &= 0, \\ [\phi(t, x), \Pi_{\phi}(t, x')] &= i\delta(x - x'), \end{aligned} \quad (6.7)$$

where  $\Pi_{\phi} = \partial_t \phi$  is the canonical conjugated momentum associated to  $\phi$ . As a consequence, the field can be expanded in terms of the mode solution basis  $\{u_k, u_k^*\}$ . Therefore,

$$\phi(t, x) = \int dk \left\{ a_k u_k + a_k^{\dagger} u_k^* \right\}. \quad (6.8)$$

Here, the integral represents a sum over the continuous index  $k$ , while  $a_k$  and  $a_k^{\dagger}$  are the coefficients of this expansion. With the help of the inner product we can invert the

---

<sup>1</sup>Throughout the text, we will omit the hat symbols above the operators in order to maintain a lighter notation, except when their use becomes necessary.

previous expression and write  $a_k$  and  $a_k^\dagger$  in terms of  $\phi$  and the mode solutions. In fact,

$$\begin{aligned}
(u_k, \phi)_M &= i \int_{\Sigma} dx (u_k^* \partial_t \phi - \phi \partial_t u_k^*) \\
&= i \int_{\Sigma} dx \left\{ u_k^* \int dk' (a_{k'} \partial_t u_{k'} + a_{k'}^\dagger \partial_t u_{k'}^*) - \partial_t u_k^* \int dk' (a_{k'} u_{k'} + a_{k'}^\dagger u_{k'}^*) \right\} \\
&= \int dk' \left\{ a_{k'} (u_k, u_{k'}) + a_{k'}^\dagger (u_k, u_{k'}^*) \right\} \\
&= a_k,
\end{aligned} \tag{6.9}$$

where we used (6.6). With this result we can compute the commutation relations concerning the coefficients  $a_k$  and  $a_k^\dagger$  in the following manner:

$$\begin{aligned}
[a_k, a_{k'}^\dagger] &= [(u_k, \phi)_M, (u_{k'}, \phi)_M^\dagger] \\
&= \left[ i \int_{\Sigma} dx \{ u_k^*(x, t) \Pi(x, t) - \partial_t u_k^*(x, t) \phi(x, t) \}, \right. \\
&\quad \left. -i \int_{\Sigma'} dx' \{ u_{k'}(x', t) \Pi(x', t) - \partial_t u_{k'}(x', t) \phi(x', t) \} \right] \\
&= \int_{\Sigma \Sigma'} dx dx' \left\{ u_k^*(x, t) u_{k'}(x', t) [\Pi(x, t), \Pi(x', t)] - u_k^*(x, t) \partial_t u_{k'}(x', t) [\Pi(x, t), \phi(x', t)] + \right. \\
&\quad \left. - \partial_t u_k^*(x, t) u_{k'}(x', t) [\phi(x, t), \Pi(x', t)] + \partial_t u_k^*(x, t) \partial_t u_{k'}(x', t) [\phi(x, t), \phi(x', t)] \right\} \\
&= i \int_{\Sigma} dx \{ u_k^* \partial_t u_{k'} - \partial_t u_k^* u_{k'} \} \\
&= \delta(k - k').
\end{aligned} \tag{6.10}$$

In this sequence of equations we take into account that  $[A + B, C] = [A, C] + [B, C]$ , we use the canonical commutation relations (6.7), and consider the fact that  $\{u_k, u_k^*\}$  form an orthogonal basis. In the same manner

$$\begin{aligned}
[a_k, a_{k'}] &= 0, \\
[a_k^\dagger, a_{k'}^\dagger] &= 0.
\end{aligned} \tag{6.11}$$

Consequently, drawing an analogy to the quantum harmonic oscillator, we can interpret the field expansion coefficients  $a_k$  and  $a_k^\dagger$  as the creation and annihilation operators, respectively. By doing so, we can span the Hilbert space in terms of the quantum states defined from  $a_k$  and  $a_k^\dagger$ . The vacuum state  $|0\rangle_M$ , where the label  $M$  indicates that we are in Minkowski space, is defined as the state annihilated by the operator  $a_k$  for any wave number  $k$ , that is,  $a_k |0\rangle_M = 0$ . From  $|0\rangle_M$  we can construct the states of one or more particles by successive applications of the creation operator  $a_k^\dagger$ . For instance, the one-particle state is represented as  $|1_k\rangle_M = a_k^\dagger |0\rangle_M$ . Applying  $a_k^\dagger$  to  $|1_k\rangle_M$  yields the state of two particles, applying  $a_k^\dagger$  to  $|2_k\rangle_M$  produces the state of three particles, and so on. Similarly, it is

possible to build the multi-particle state as  $|1_{k_1}, 1_{k_2}, \dots, 1_{k_n}\rangle = a_{k_1}^\dagger a_{k_2}^\dagger \dots a_{k_n}^\dagger |0\rangle_M$ , where we are supposing a total of  $n$  particles with different wave numbers. It is worth mentioning that when the number of particles remains fixed, we only need to use the appropriate Hilbert space to provide a quantum description of our system. However, in cases where the number of particles fluctuates, as commonly seen in Quantum Field Theory, it becomes necessary to consider all the possible particle states. In this manner, the Hilbert space becomes the direct sum of all possible individual particle states. Consequently,

$$\mathcal{H} = \mathbb{C} \oplus \mathcal{H}_1 \oplus (\mathcal{H}_1 \otimes \mathcal{H}_1)_{sym} \oplus (\mathcal{H}_1 \otimes \mathcal{H}_1 \otimes \mathcal{H}_1)_{sym} \oplus \dots, \quad (6.12)$$

where  $\mathbb{C}$  is associated with the vacuum state,  $\mathcal{H}_1$  represents the Hilbert space of a single particle, and because of the bosonic nature of the field, we must consider the symmetrized Hilbert space for multi-particle states.

As a conclusion, we can say that expand the field in terms of positive and negative frequency modes allow us to physically interpret the coefficients  $\hat{a}_k$  and  $\hat{a}_k^\dagger$  as operators from which we construct the Fock space. But note that this construction is intrinsically tied to the basis  $\{u_k, u_k^*\}$ , obtained from the equation of motion (6.3). As a result, if we use another basis  $\{\bar{u}_k, \bar{u}_k^*\}$ , the coefficients appearing in the expansion of  $\phi$  would be different, so that the Fock space associated with this new basis could be slightly distinct. In particular, nothing guarantees that the vacuum state from which we construct the multi-particle state is the same. More clearly, we can assume an expansion for the field as follows

$$\phi(t, x) = \int dk' \left\{ b_{k'} \bar{u}_{k'} + b_{k'}^\dagger \bar{u}_{k'}^* \right\}, \quad (6.13)$$

where  $b_{k'}$  and  $b_{k'}^\dagger$  are interpreted as creation and annihilation operators in this new basis, obeying commutation relations similar to (6.10) and (6.11), and with a vacuum state  $|\bar{0}\rangle_M$  satisfying  $b_{k'} |\bar{0}\rangle_M = 0$ .

Since both basis are assumed complete, we can write  $\bar{u}_k$  in terms of  $\{u_k, u_k^*\}$  and vice-versa, with the correspondent expressions called Bogolubov transformations [194, 195]. For instance, we have that

$$\bar{u}_{k'} = \int dk (\alpha_{k'k} u_k + \beta_{k'k} u_k^*), \quad (6.14)$$

where the matrices  $\alpha_{k'k}$  and  $\beta_{k'k}$  are the Bogolubov coefficients. Taking into account that the inner product (6.5) is antilinear in the first entry, meaning that for any complex constant  $c$  the relation  $(c\phi_1, \phi_2)_M = c^*(\phi_1, \phi_2)_M$  holds, and considering the orthonormality

of  $\{u_k, u_k^*\}$  expressed by the set of equations (6.6), we have that

$$\begin{aligned}(\bar{u}_{k'}, u_k)_M &= \alpha_{k'k}^*, \\ (\bar{u}_{k'}, u_k^*)_M &= -\beta_{k'k}^*.\end{aligned}\tag{6.15}$$

So, we can invert expression (6.14) and expand  $u_k$  in terms of  $\bar{u}_{k'}$  as follows:

$$u_k = \int dk' (\alpha_{k'k}^* \bar{u}_{k'} - \beta_{k'k} \bar{u}_{k'}^*).\tag{6.16}$$

By inserting this previous equation into (6.14), we obtain a normalization condition satisfied by the Bogolubov coefficients,

$$\int dk (\alpha_{k'k} \alpha_{k''k}^* - \beta_{k'k} \beta_{k''k}^*) = \delta(k' - k'').\tag{6.17}$$

Concerning the creation and annihilation operators  $b_{k'}$  and  $b_{k'}^\dagger$ , we can also express them in terms of inner products associated with this new basis, similarly to equation (6.9). As a matter of fact,

$$b_{k'} = (\bar{u}_{k'}, \phi)_M.\tag{6.18}$$

Now, inserting the expansion (6.8) in this relation we obtain that

$$\begin{aligned}b_{k'} &= \int dk \left\{ a_k (\bar{u}_{k'}, u_k)_M + a_k^\dagger (\bar{u}_{k'}, u_k^*)_M \right\} \\ &= \int dk \left\{ \alpha_{k'k}^* a_k - \beta_{k'k} a_k^\dagger \right\}.\end{aligned}\tag{6.19}$$

As a consequence, when  $\beta_{k'k} \neq 0$ , the annihilation operator  $b_{k'}$ , defined in the  $\{\bar{u}_{k'}, \bar{u}_{k'}^*\}$  basis, does not annihilate the  $|0\rangle_M$  vacuum, meaning that  $|0\rangle_M$  and  $|\bar{0}\rangle_M$  are not equivalent. More precisely, the average of the number operator  $\bar{N}_{k'} \equiv b_{k'}^\dagger b_{k'}$ , computed in the  $|0\rangle_M$  vacuum, is not null, but actually

$$\langle \bar{N}_{k'} \rangle_M \equiv {}_M \langle 0 | \bar{N}_{k'} | 0 \rangle_M = \int dk |\beta_{k'k}|^2.\tag{6.20}$$

Therefore, we can conclude that the vacuum definition and the particle concept are not unique, depending on the positive and negative frequency modes used to expand the field. In other words, different coordinate systems can lead to different vacuum definitions and, consequently, different particle numbers, as is the case of Minkowski and Rindler observers.

In order to give a Rindler description of the Minkowski vacuum, we need to quantize the field using the coordinates associated with the accelerated observer, which are given

by (6.1). With these transformations the action (6.2) becomes

$$S = \frac{1}{2} \int d\tau d\xi \left( \left( \frac{\partial\phi}{\partial\tau} \right)^2 - \left( \frac{\partial\phi}{\partial\xi} \right)^2 \right), \quad (6.21)$$

admitting

$$\left( -\frac{\partial^2}{\partial\tau^2} + \frac{\partial^2}{\partial\xi^2} \right) \phi(\tau, \xi) = 0, \quad (6.22)$$

as equation of motion, as expected due the conformal equivalence of the metrics. Analogously to the previous case, the mode solutions are

$$v_k(\tau, \xi) = \frac{1}{\sqrt{4\pi\omega_k}} e^{i(k\xi - \omega_k\tau)}, \quad (6.23)$$

with the  $v_k$  modes identified as positive frequency modes with respect to  $\tau$ , such that  $\partial_\tau v_k = -i\omega_k v_k$ , while  $v_k^*$  correspond to the negative frequency modes, with  $\partial_\tau v_k^* = i\omega_k v_k^*$ . However, there is a slight difference here. Whereas in the action (6.2) the field  $\phi$  is defined all over Minkowski spacetime, in (6.21) the field is defined only in the region I of figure 6.1, mathematically expressed for  $-x < t < x$  and  $x > 0$ .

With the effort to expand the field in terms of  $v_k$  and  $v_k^*$ , we can define the equivalent to the Klein-Gordon inner product in Rindler space<sup>2</sup>:

$$(\phi_1, \phi_2)_R := i \int_\Sigma d\xi \left( \phi_1^* \frac{\partial\phi_2}{\partial\tau} - \phi_2 \frac{\partial\phi_1^*}{\partial\tau} \right), \quad (6.24)$$

on which  $\Sigma$  is the Cauchy hypersurface given by constant foliations of the Rindler temporal variable. From this definition, we realize that  $\{v_k, v_k^*\}$  form a completely orthonormal basis, satisfying

$$\begin{aligned} (v_k^*, v_{k'})_R &= 0, \\ (v_k, v_{k'})_R &= \delta(k - k'), \\ (v_k^*, v_{k'}^*)_R &= -\delta(k - k'). \end{aligned} \quad (6.25)$$

---

<sup>2</sup>The generalization of the Klein-Gordon product in curved spacetimes can be expressed as

$$(\phi_1, \phi_2) := i \int_\Sigma \sqrt{\sigma} d\Sigma^\mu (\phi_1^* \nabla_\mu \phi_2 - \phi_2 \nabla_\mu \phi_1^*),$$

with  $d\Sigma^\mu = d\Sigma n^\mu$  representing an infinitesimal normal vector associated to the Cauchy hypersurface  $\Sigma$  and  $\sigma = \det \sigma_{ij}$ , where  $\sigma_{ij}$  is the induced metric. When applied to Minkowski and Rindler spacetimes, this inner product returns the expressions (6.5) and (6.24), respectively.

similarly to (6.6). Then, the field can be expanded as

$$\phi(\tau, \xi) = \int dk' \left\{ d_{k'} v_{k'} + d_{k'}^\dagger v_{k'}^* \right\}, \quad (6.26)$$

where  $d_{k'}$  and  $d_{k'}^\dagger$  are the annihilation and creation operators, respectively. These operators define particle states in Rindler spacetime and obey canonical commutation relations similar to those presented in (6.10) and (6.11). Specifically, the vacuum state  $|0\rangle_R$  is such that  $d_{k'} |0\rangle_R = 0$ , for all values of  $k'$ .

To compute the Bogolubov coefficients, it is interesting to introduce the null variables in both, Minkowski and Rindler spaces. They are given by

$$U = t - x \quad V = t + x, \quad (6.27)$$

$$\tilde{U} = \tau - \xi \quad \tilde{V} = \tau + \xi. \quad (6.28)$$

So, the expansions (6.8) and (6.26) can be written as

$$\phi(t, x) = \int_0^\infty \frac{dk}{\sqrt{4\pi k}} \left\{ e^{-ikU} a_k + e^{ikU} a_k^\dagger + e^{-ikV} a_{-k} + e^{ikV} a_{-k}^\dagger \right\}, \quad (6.29)$$

$$\phi(\tau, \xi) = \int_0^\infty \frac{dk'}{\sqrt{4\pi k'}} \left\{ e^{-ik'\tilde{U}} d_{k'} + e^{ik'\tilde{U}} d_{k'}^\dagger + e^{-ik'\tilde{V}} d_{-k'} + e^{ik'\tilde{V}} d_{-k'}^\dagger \right\}, \quad (6.30)$$

where, in order to obtain this result, we separate the expansions into positive and negative contributions of the wave number, performing the change of variables  $k \rightarrow -k$  in the negative part. After this we identify  $\omega_k = |k|$  just as  $k$  since the integrals run from zero to infinity. The first two terms are identified as right-moving modes, while the last two correspond to left-moving modes.

In terms of these variables, the equations of motion (6.3) and (6.22) take the form

$$\partial_U \partial_V \phi = 0 \quad \partial_{\tilde{U}} \partial_{\tilde{V}} \phi = 0. \quad (6.31)$$

Thus, it is reasonable to assume that the field admits the following separation

$$\phi(U, V) = A(U) + B(V) \quad \phi(\tilde{U}, \tilde{V}) = \tilde{A}(\tilde{U}) + \tilde{B}(\tilde{V}), \quad (6.32)$$

corresponding to a sum of right-moving and left-moving modes. Now, taking into consideration the explicit form of the Rindler transformations (equation (6.1)) in the definition of the null variables, we obtain that

$$U = -\frac{e^{-a\tilde{U}}}{a} \quad V = \frac{e^{a\tilde{V}}}{a}, \quad (6.33)$$

that is,  $U = U(\tilde{U})$  can be considered a function of  $\tilde{U}$  alone, without any dependency in

$\tilde{V}$ . Similarly we have that  $V = V(\tilde{V})$ . Since in region I of Minkowski spacetime we can equivalently expand the field in terms of the  $(U, V)$  and  $(\tilde{U}, \tilde{V})$  variables, which means that  $\phi(U, V) = \phi(\tilde{U}, \tilde{V})$  in this region, we must have that  $A(U) = \tilde{A}(\tilde{U})$  and  $B(V) = \tilde{B}(\tilde{V})$ .

Considering the first equality, we obtain

$$\int_0^\infty \frac{dk}{\sqrt{4\pi k}} \left\{ e^{-ikU} a_k + e^{ikU} a_k^\dagger \right\} = \int_0^\infty \frac{dk'}{\sqrt{4\pi k'}} \left\{ e^{-ik'\tilde{U}} d_{k'} + e^{ik'\tilde{U}} d_{k'}^\dagger \right\}. \quad (6.34)$$

Applying the Fourier transformation in relation to  $\tilde{U}$  in both sides and using the definition of the delta function, we have that

$$\begin{aligned} \int_{-\infty}^\infty \frac{d\tilde{U}}{\sqrt{2\pi}} e^{ik''\tilde{U}} \int_0^\infty \frac{dk}{\sqrt{4\pi k}} \left\{ e^{-ikU} a_k + e^{ikU} a_k^\dagger \right\} &= \int_{-\infty}^\infty \frac{d\tilde{U}}{\sqrt{2\pi}} e^{ik''\tilde{U}} \int_0^\infty \frac{dk'}{\sqrt{4\pi k'}} \left\{ e^{-ik'\tilde{U}} d_{k'} + e^{ik'\tilde{U}} d_{k'}^\dagger \right\}, \\ &= \int_0^\infty \frac{dk'}{\sqrt{2k'}} \delta(k' - k'') d_{k'} + \int_0^\infty \frac{dk'}{\sqrt{2k'}} \delta(k' + k'') d_{k'}^\dagger, \\ &= \frac{d_{k''}}{\sqrt{2k''}}, \end{aligned} \quad (6.35)$$

from which we obtain the following Bogolubov transformation for  $d_{k''}$

$$d_{k''} = \int_0^\infty dk \left\{ \left( \int_{-\infty}^\infty \frac{d\tilde{U}}{2\pi} \sqrt{\frac{k''}{k}} e^{i(k''\tilde{U} - kU)} \right) a_k + \left( \int_{-\infty}^\infty \frac{d\tilde{U}}{2\pi} \sqrt{\frac{k''}{k}} e^{i(k''\tilde{U} + kU)} \right) a_k^\dagger \right\}, \quad (6.36)$$

with the Bogolubov coefficients given by

$$\begin{aligned} \alpha_{k''k}^* &= \int_{-\infty}^\infty \frac{d\tilde{U}}{2\pi} \sqrt{\frac{k''}{k}} e^{i(k''\tilde{U} + \frac{k}{a}e^{-a\tilde{U}})}, \\ \beta_{k''k}^* &= - \int_{-\infty}^\infty \frac{d\tilde{U}}{2\pi} \sqrt{\frac{k''}{k}} e^{i(k''\tilde{U} - \frac{k}{a}e^{-a\tilde{U}})}, \end{aligned} \quad (6.37)$$

where we have used equation (6.33). Then, the explicit computation of the integrals yields

$$\begin{aligned} \alpha_{k''k}^* &= \frac{1}{2\pi a} \sqrt{\frac{k''}{k}} \exp\left(\frac{\pi k''}{2a}\right) \left(\frac{a}{k}\right)^{-\frac{ik''}{a}} \Gamma\left(-\frac{ik''}{a}\right), \\ \beta_{k''k}^* &= -\frac{1}{2\pi a} \sqrt{\frac{k''}{k}} \exp\left(-\frac{\pi k''}{2a}\right) \left(\frac{a}{k}\right)^{-\frac{ik''}{a}} \Gamma\left(-\frac{ik''}{a}\right). \end{aligned} \quad (6.38)$$

As a result, the Bogolubov coefficients are related in such manner that  $|\alpha_{k''k}|^2 = e^{\frac{2\pi k''}{a}} |\beta_{k''k}|^2$ .

Additionally, the normalization condition (6.17) for the Bogolubov coefficients returns

$$\int_0^\infty dk (|\alpha_{k''k}|^2 - |\beta_{k''k}|^2) = \delta(0) \quad (6.39)$$

when  $k' = k''$ . Therefore, if  $N_{k'}^R \equiv d_{k'}^\dagger d_{k'}$  is the number operator defined in Rindler spacetime, then its mean value computed in Minkowski vacuum is just (see equation (6.20))

$$\langle N_{k'}^R \rangle_M = \frac{1}{e^{\frac{2\pi k'}{a}} - 1} \delta(0), \quad (6.40)$$

with  $\delta(0)$  a divergent factor due the infinite volume of the space. After a proper regularization process, for example considering the quantization of the field in a finite box of volume  $V$ , with the integrals substituted by discrete sums, the  $\delta(0)$  factor give place to  $V$ , in such manner that the mean density  $\langle n_{k'}^R \rangle_M \equiv \langle N_{k'}^R \rangle_M / V$  becomes

$$\langle n_{k'}^R \rangle_M = \frac{1}{e^{\frac{2\pi k'}{a}} - 1}, \quad (6.41)$$

which is a Planck spectrum with Unruh temperature

$$T = \frac{a}{2\pi}. \quad (6.42)$$

The significance of this result is profound: Minkowski and Rindler observers do not share the same vacuum. While the Minkowski vacuum represents a state of no particles for an inertial observer, the same vacuum state corresponds to a Bose-Einstein distribution in Rindler spacetime. This means that an uniformly accelerated detector will see a thermal bath of particles, with temperature proportional to the acceleration, exemplifying the fact that the particle concept is, in general, frame-dependent.

## 6.2 The Schrödinger representation and the scalar field wave functional in Minkowski space

A key element in the Bohm interpretation is the wave function, which provides the trajectories of particles through the guidance equations. In the previous chapter, we saw that by writing the wave function in polar form and substituting into the Schrödinger equation, we obtain a Hamilton-Jacobi-like equation and a continuity equation, from which we infer the quantum particles velocity field and, consequently, the Bohmian trajectories. Nevertheless, we derived the Unruh effect in the previous section only using the vacuum eigenstates  $|0\rangle_M$  and  $|0\rangle_R$ , without any reference to any wave function. Thus, in order to give a Bohmian description of the Unruh effect we need to introduce the Schrödinger representation of the fields, from which we are able to establish a wave functional associated with the vacuum states.

In this approach, wave functionals are essentially coordinate representations of state vectors, similar to the usual Quantum Mechanics. The main difference here is that the

coordinates are given in terms of fields, with canonically conjugate momenta replaced by their respective functional derivatives. In this scenario, the Schrödinger equation becomes a functional differential equation, with the solutions representing the eigenstates, expressed in terms of eigenfunctionals.

More formally, for a field operator  $\hat{\phi}(x)$  with eigenstate  $|\phi\rangle$  and eigenvalue  $\phi(x)$ , we have that  $\hat{\phi}(x)|\phi\rangle = \phi(x)|\phi\rangle$ . Therefore, the wave functional  $\Psi[\phi, t]$ , a functional of the complex function  $\phi(x)$ , is the projection of the state  $|\Psi(t)\rangle$  on the coordinate basis  $|\phi\rangle$ , which is mathematically expressed as  $\Psi[\phi, t] \equiv \langle\phi|\Psi\rangle$ . If the field operator satisfies the canonical commutation relations (equation (6.7)), then the functional differential representation of the conjugated momentum is  $\hat{\Pi}_\phi = -i\frac{\delta}{\delta\phi(x)}$ , where  $\frac{\delta}{\delta\phi(x)}$  denotes the functional derivative with respect to the eigenvalue  $\phi(x)$ . Thus, the following relations hold for the field operator and its conjugated momentum:

$$\hat{\phi}(x)\Psi[\phi, t] = \phi(x)\Psi[\phi, t], \quad \hat{\Pi}_\phi\Psi[\phi, t] = -i\frac{\delta\Psi[\phi, t]}{\delta\phi(x)}. \quad (6.43)$$

Once in possession of (6.43), we can write the Hamiltonian  $\hat{H}$  as a functional differential operator, from which we can define a functional Schrödinger equation

$$i\frac{\partial\Psi[\phi, t]}{\partial t} = \hat{H}\Psi[\phi, t], \quad (6.44)$$

and find the functional eigenstates.

For the real massless scalar field in Minkowski space considered in the last section and described by the action (6.2), the associated Hamiltonian operator is

$$H = \frac{1}{2} \int dx \left\{ \left( \frac{\partial\phi}{\partial t} \right)^2 + \left( \frac{\partial\phi}{\partial x} \right)^2 \right\} = \frac{1}{2} \int dx \left\{ -\frac{\delta^2}{\delta\phi^2} + \left( \frac{\partial\phi}{\partial x} \right)^2 \right\}, \quad (6.45)$$

where we identify  $\hat{\Pi}_\phi = \partial_t\phi$  as the canonical momentum, described in terms of the functional derivatives. Therefore, the correspondent Schrödinger equation is

$$i\frac{\partial\Psi[\phi, t]}{\partial t} = \frac{1}{2} \int dx \left\{ -\frac{\delta^2}{\delta\phi^2} + \left( \frac{\partial\phi}{\partial x} \right)^2 \right\} \Psi[\phi, t], \quad (6.46)$$

with the coordinate  $x$  being a continuous index summing over all the “particles”, in an analogy with a many-body quantum system, and with the term  $\frac{1}{2} \int dx (\partial_x\phi)^2$  acting as an “external” potential.

In order to give a Bohmian description for the scalar field, we will proceed similarly as outlined in the previous chapter and write the wave functional in the polar form  $\Psi[\phi, t] = R[\phi, t]e^{iS[\phi, t]}$ . By inserting this expression into Schrödinger equation (6.46) and separating in real and imaginary parts, we obtain two equations (compare with (2.5) and

(2.6))

$$\frac{\partial S}{\partial t} + \frac{1}{2} \int dx \left\{ \left( \frac{\delta S}{\delta \phi} \right)^2 + \left( \frac{\partial \phi}{\partial x} \right)^2 \right\} + Q = 0, \quad (6.47)$$

$$\frac{\partial R^2}{\partial t} + \int dx \frac{\delta}{\delta \phi} \left( R^2 \frac{\delta S}{\delta \phi} \right) = 0. \quad (6.48)$$

The first one is a Hamilton-Jacobi-like equation, with a supplementary non-local quantum potential

$$Q[\phi, t] = -\frac{1}{2R} \int dx \frac{\delta^2 R}{\delta \phi^2}, \quad (6.49)$$

resembling equation (2.7). The second is a continuity-like equation, from which we can identify  $R^2[\phi, t]$  as a probability density. In this sense, we can interpret  $R^2 \mathcal{D}\phi$  as the probability for the field lie in an infinitesimal hypervolume  $\mathcal{D}\phi = \prod_x d\phi$ . Also, we can identify the field velocity

$$\frac{\partial \phi}{\partial t} = \frac{\delta S}{\delta \phi}, \quad (6.50)$$

from which we obtain the field trajectories. So, in this Bohmian field interpretation we are presuming that at each instant the field possesses a clearly defined value in all the space, with its evolution determined by the integration of the guidance equation (6.50). In this sense, the quantum theory, which in this case is a quantum field theory, is built based in the Hamilton-Jacobi formalism for the classical field theory, similar to what we have done in the previous chapter.

The key element that brings quantum properties to this classical-based theory is the quantum potential. For instance, taking the time derivative of equation (6.50) and using the Hamilton-Jacobi equation (6.47), we obtain that

$$\left( \frac{\partial^2}{\partial t^2} - \frac{\partial^2}{\partial x^2} \right) \phi = -\frac{\delta Q}{\delta \phi}, \quad (6.51)$$

which is exactly the equation of motion (6.3) but with a corrective "quantum force". It is this extra term that gives rise to the distinctive individual quantum effects observed in quantum field theory. When the quantum potential is negligible compared to the other quantities, from equations (6.47) and (6.51) we recover the classical Hamilton-Jacobi equation and the Klein-Gordon equation (6.3), respectively, in such manner that it is possible to connect the classical and quantum field theories with this approach. Nevertheless, it is important to emphasize that here  $\phi$  is the eigenvalue of the field operator  $\hat{\phi}$  computed throughout the field trajectory. Then, while  $\phi$  follows equation (6.51), in the

In Heisenberg representation the operator  $\hat{\phi}$  obeys the equation

$$\left( \frac{\partial^2}{\partial t^2} - \frac{\partial^2}{\partial x^2} \right) \hat{\phi} = 0. \quad (6.52)$$

In summary, starting from a general quantum state  $\Psi[\phi, t]$  defined through the functional Schrödinger equation, the Bohmian interpretation allows us to study events in quantum field theory in an individualized manner, not solely restricted to statistical observables. For each different initial condition considered in the guidance equation (or equivalently, in the respective equation of motion), we have a distinct occurrence, or more precisely, a different field trajectory. When we take into account all possible field trajectories, we can calculate the Bohmian averages as

$$\langle \mathcal{O}(t) \rangle_{dBB} = \int \mathcal{D}\phi |\Psi[\phi, t]|^2 \mathcal{O}[\phi, t], \quad (6.53)$$

with  $\mathcal{O}[\phi, t]$  being a physically meaningful property related to the field trajectories thoughtfully chosen to yield the same results as the conventional mean values of the quantum operators

$$\langle \hat{\mathcal{O}} \rangle = \int \mathcal{D}\phi \Psi^*[\phi, t] (\hat{\mathcal{O}} \Psi[\phi, t]). \quad (6.54)$$

The advantage of such an interpretation is that it allows for the separation of contributions of classical and purely quantum nature, which is not possible in the usual interpretation. This distinction is exemplified, for instance, in the Hamilton-Jacobi equation (6.47), where the energy

$$E = -\frac{\partial S}{\partial t} \quad (6.55)$$

is composed by the “kinetic” and “classical” potential terms,

$$K = \frac{1}{2} \int dx \left( \frac{\delta S}{\delta \dot{\phi}} \right)^2 \quad \text{and} \quad V = \frac{1}{2} \int dx \left( \frac{\partial \phi}{\partial x} \right)^2, \quad (6.56)$$

respectively, in addition to the quantum potential (6.49). This differentiation remains possible even when we calculate the individual mean contributions of each term in the Hamilton-Jacobi equation, as we will further explore when considering the Unruh effect.

However, a relevant issue arises: how to address a non-local quantum potential in a quantum field theory, given that one of its foundational principles is locality? In a first moment, it is important to note that the expression for  $Q[\phi, t]$  (equation (6.49)) takes into account the contribution of field states across all of space. Therefore, the corrective quantum force present on the right-hand side of the equation of motion (6.51)

instantaneously connects field elements in different spatial regions. Secondly, observe that this same term breaks Lorentz covariance, as time and space are treated differently in its presence. This is an expected result since we quantize the system through the Schrödinger representation of fields, with a wave functional satisfying the Schrödinger equation (6.46), which is not Lorentz-covariant.

While these ideas may initially appear counter-intuitive, it is worth emphasizing that the non-locality of fields and the breaking of Lorentz covariance are both purely quantum effects stemming from individual processes. As we have previously stated, in the limit where the quantum potential is negligible, the quantum force vanishes, and consequently, we recover the Klein-Gordon equation, thus restoring notions of locality and covariance. Hence, we can assert that the quantum potential is responsible for these peculiar characteristics.

Another aspect in favor of the Bohmian interpretation is that, as mentioned before, in field theory we do not measure individual field configurations due to specific trajectories. Instead, we obtain expected values, which are not subject to the peculiarities of the quantum potential. In this manner, locality and covariance are restored at the experimental level, both being statistical effects according to this framework.

To conclude this section and illustrate how the functional formalism works, it is interesting to obtain an explicit form for the wave functional of the scalar field from equation (6.46). In pursuit of this objective, let us consider the Fourier expansion for  $\phi(t, x)$

$$\phi(t, x) = \int_{-\infty}^{\infty} \frac{dk}{\sqrt{2\pi}} e^{ikx} \phi_k(t). \quad (6.57)$$

Because of the reality of the field, the mode  $\phi_k(t)$  should be such that  $\phi_k = \phi_{-k}$ . Inserting this expression into equation (6.45) and using the definition of the delta function, the Hamiltonian operator can be expanded as

$$H = \int_0^{\infty} dk \left\{ \left( \frac{\partial \phi_k}{\partial t} \right) \left( \frac{\partial \phi_k^*}{\partial t} \right) + k^2 |\phi_k|^2 \right\}, \quad (6.58)$$

where we use the fact that the sum over positive and negative  $k$  yields the same result. So, in this form, the effective contribution to the energy in (6.58) for each mode  $k$  is half the value obtained, since the contribution due  $-k$  is hidden in the value of the energy. Identifying  $\Pi_{\phi_k} = \partial_t \phi_k^*$  as the mode decomposition of the canonical momentum and considering that the functional derivative admits the following expansion

$$\frac{\delta}{\delta \phi} = \int_{-\infty}^{\infty} \frac{dk}{\sqrt{2\pi}} e^{-ikx} \frac{\partial}{\partial \phi_k}, \quad (6.59)$$

the Schrödinger equation (6.44) becomes

$$i \frac{\partial \Psi[\phi, t]}{\partial t} = \int_0^\infty dk \left\{ -\frac{\partial^2}{\partial \phi_k \partial \phi_k^*} + k^2 |\phi_k|^2 \right\} \Psi[\phi, t]. \quad (6.60)$$

Assuming that the wave functional can be expressed by a product state over the continuous index  $k$  as

$$\Psi[\phi, \eta] = \prod_{k>0} \Psi_k[\phi_k, \phi_k^*, \eta], \quad (6.61)$$

with  $\eta$  a general temporal parameter (which in Minkowski represents the variable  $t$ ), then each individual  $\Psi_k$  will satisfy an independent Schrödinger equation

$$i \frac{\partial}{\partial t} \Psi_k[\phi_k, \phi_k^*, t] = \left\{ -\frac{\partial^2}{\partial \phi_k \partial \phi_k^*} + k^2 |\phi_k|^2 \right\} \Psi_k[\phi_k, \phi_k^*, t], \quad (6.62)$$

being identical to the Schrödinger equation for a quantum harmonic oscillator. This confirms, therefore, the notion that the Klein-Gordon field can be viewed as a collection of infinite harmonic oscillators, each one indexed by a wave number  $k$ . Hence, the ground state solution is just

$$\Psi_k[\phi_k, \phi_k^*, t] = \sqrt{\frac{\omega_k}{\pi}} e^{-k|\phi_k|^2} e^{-i\omega_k t}, \quad (6.63)$$

Since in the Hamiltonian (6.58) we just consider the positive values of  $k$ , each mode  $\Psi_k$  in the wave functional decomposition (6.61) corresponds to a product of two terms, one due to  $k$  and another due to  $-k$ , both given the same contribution according to equation (2.15). Also, as mentioned earlier, each  $k$  is counted twice in the Hamiltonian, in such manner that the ground state energy in (6.63) is two times the expected value. Consequently, the original wave functional  $\Psi[\phi, t]$  is

$$\Psi[\phi, t] = \left( \prod_{k>0} \sqrt{\frac{\omega_k}{\pi}} \right) \exp \left( - \int_0^\infty k |\phi_k|^2 dk \right) e^{-i\Omega_0 t} \quad (6.64)$$

with  $\Omega_0 = \int_0^\infty \omega_k dk$  being the zero-point energy, which does not have a finite value due to the infinity number of oscillators.

Once in possession of the wave functional, we can apply the Bohmian formalism by identifying the radial part  $R[\phi, t]$  and the phase  $S[\phi, t]$ , present in the Hamilton-Jacobi equation (6.47), the continuity equation (6.48), and the guidance equation (6.50). For the

ground state (6.64) we have that

$$R[\phi, t] = \left( \prod_{k>0} \sqrt{\frac{\omega_k}{\pi}} \right) \exp \left( - \int_0^\infty k |\phi_k|^2 dk \right) \quad (6.65)$$

and

$$S[\phi, t] = -\Omega_0 t, \quad (6.66)$$

such that the phase is independent of  $\phi$ . Therefore, the derivative of  $S[\phi, t]$  with respect to  $\phi$  is zero, implying in a solution of the guidance equation independent of time, that is, a static field configuration

$$\phi(x, t) = \phi_0(x). \quad (6.67)$$

This is a result previously anticipated: eigenstates of a quantum system generate static Bohmian trajectories, in perfect analogy to the result presented in subsection 2.3.1 of the previous chapter. Also, the total energy of the system is, indeed,  $\Omega_0$ , since according to Hamilton-Jacobi equation,

$$E = -\frac{\partial S}{\partial t} = \Omega_0. \quad (6.68)$$

Once that the canonical momentum is null (static trajectory), we do not have a “kinetic” contribution  $K$  (equation (6.56)), only remaining the potential  $V$  as a “classical” contribution to the total energy. Then

$$K = 0 \quad \text{and} \quad V = \int_0^\infty k |\phi_k|^2 dk. \quad (6.69)$$

As a consequence, the quantum potential can be expressed simply as

$$Q = \Omega_0 - V. \quad (6.70)$$

Please note that the calculation of these quantities takes into account the contribution of an infinite number of oscillators, which can make it challenging to analyze these results according to physical grounds. Furthermore, when dealing with complex systems, the need to employ complex variational calculation techniques, which can be quite complicated depending on the specific model under consideration. With this in mind, working in momentum space becomes more advantageous, because we can explicitly observe the contribution of each term in the Hamilton-Jacobi equation for every value of  $k$ , thus simplifying the calculation of averages. In the following sections, we will apply the formalism

presented here to the case of the Unruh effect, where we will demonstrate that for each  $k$  an associated Hamilton-Jacobi equation and a continuity equation are derived.

### 6.3 The Rindler wave functional and its Bohmian interpretation in the right-wedge

Our goal in this section is essentially to calculate the wave functional associated with the vacuum state of the massless scalar field in Rindler spacetime and gives its Bohmian description. The strategy for studying the Unruh effect is similar to what was developed in Section [6.1](#) when comparing Minkowski and Rindler vacua. The difference here is that instead of defining the vacuum states from the annihilation operators in their respective spaces, we define the vacuum states from the wave functionals associated with the scalar field. The idea is essentially to express the wave functional  $(\Psi^M)_0$  of the Minkowski vacuum in terms of Rindler variables, obtaining its temporal evolution [\[191\]](#). However, we cannot directly apply the results from the previous section since those were obtained considering the entire spacetime, not just region I in Figure [6.1](#) ( $-x < t < x$  and  $x > 0$ ), which slightly alters the wave functional.

With the objective to achieve a normal mode decomposition for  $(\Psi^M)_0$ , we expand the field in terms of Minkowski modes using the half-Fourier expansion, taking into account the fact that we are restricted to the right-Rindler wedge. So,

$$\phi(t, x) = \sqrt{\frac{2}{\pi}} \int_0^\infty dk \sin(kx) \phi_k^M(t), \quad (6.71)$$

with  $(\phi_k^M)^* = \phi_k^M$  being the Minkowski modes. From action [\(6.2\)](#) and the expansion [\(6.71\)](#), we can express the Minkowski Hamiltonian for the right wedge as

$$H^M = \frac{1}{2} \int_0^\infty dk \left\{ \left( \frac{\partial \phi_k^M}{\partial t} \right)^2 + k^2 (\phi_k^M)^2 \right\} = \frac{1}{2} \int_0^\infty dk \left\{ -\frac{\partial^2}{\partial (\phi_k^M)^2} + k^2 (\phi_k^M)^2 \right\}, \quad (6.72)$$

where we identify  $\Pi_{\phi_k^M}^M = \partial_t \phi_k^M$ . Assuming a decomposition for the wave functional analogous to the one given in equation [\(6.61\)](#), we have an independent Schrödinger equation for each  $\Psi_k$ , that is,

$$i \frac{\partial}{\partial t} \Psi_k^M[\phi_k^M, t] = \frac{1}{2} \left\{ -\frac{\partial^2}{(\partial \phi_k^M)^2} + k^2 (\phi_k^M)^2 \right\} \Psi_k^M[\phi_k^M, t], \quad (6.73)$$

which is slightly different from (6.60). The ground state solution for this case is

$$\Psi_k[\phi_k^M, t] = \left(\frac{\omega_k}{\pi}\right)^{1/4} e^{-\frac{1}{2}k(\phi_k^M)^2} e^{-\frac{i}{2}\omega_k t}, \quad (6.74)$$

implying in a wave functional of the form,

$$(\Psi^M)_0[\phi_k^M, t] = \left\{ \prod_{k>0} \left(\frac{\omega_k}{\pi}\right)^{1/4} \right\} \exp\left(-\frac{1}{2} \int_0^\infty k (\phi_k^M)^2 dk\right) e^{-i\Omega_0 t}, \quad (6.75)$$

with  $\Omega_0 = \frac{1}{2} \int_0^\infty \omega_k dk$ , being half of the value obtained for the entire space problem.

The wave functional  $(\Psi^R)_0$  of the Rindler ground state can be obtained in a similar manner. Considering that the spatial variable  $\xi$  runs from minus infinity to infinity, the field admits a complete Fourier expansion in terms of the Rindler variables, namely,

$$\phi(\tau, \xi) = \int_{-\infty}^{\infty} \frac{dk'}{\sqrt{2\pi}} e^{ik'\xi} \phi_{k'}^R(\tau), \quad (6.76)$$

with  $(\phi_{k'}^R)^* = \phi_{-k'}^R$ . As a result, from the action (6.21) we obtain the Rindler Hamiltonian

$$H^R = \int_0^\infty dk' \left\{ \left(\frac{\partial \phi_{k'}^R}{\partial t}\right) \left(\frac{\partial \phi_{k'}^{R*}}{\partial t}\right) + k'^2 |\phi_{k'}^R|^2 \right\} = \int_0^\infty dk' \left( -\frac{\partial^2}{\partial \phi_{k'}^R \partial \phi_{k'}^{R*}} + k'^2 |\phi_{k'}^R|^2 \right). \quad (6.77)$$

In virtue of the conformal invariance between Minkowski and Rindler spaces, the Hamiltonians (6.58) and (6.77) have the same format. As a consequence, we will have a similar functional Schrödinger equation

$$i \frac{\partial}{\partial \tau} \Psi_{k'}^R[\phi_{k'}^R, \phi_{k'}^{R*}, \tau] = \left\{ -\frac{\partial^2}{\partial \phi_{k'}^R \partial \phi_{k'}^{R*}} + k'^2 |\phi_{k'}^R|^2 \right\} \Psi_{k'}^R[\phi_{k'}^R, \phi_{k'}^{R*}, \tau], \quad (6.78)$$

with alike ground state solution

$$\Psi_{k'}^R[\phi_{k'}^R, \phi_{k'}^{R*}, \tau] = \sqrt{\frac{\omega_{k'}}{\pi}} e^{-k' |\phi_{k'}^R|^2} e^{-i\omega_{k'} \tau}. \quad (6.79)$$

Despite the appearance, the vacuums defined by equations (6.74) and (6.79) are essentially different, seeing that we have distinct field configurations. However, as they are defined in different temporal variables, we need to consider a simultaneous Cauchy hypersurface in both spaces in order to compare them, what is achieved for  $t = \tau = 0$ . By inverting equation (6.71) we obtain the Minkowski modes in terms of the field, that

is to say,

$$\phi_k^M(t) = \sqrt{\frac{2}{\pi}} \int_0^\infty dx \sin(kx) \phi(t, x). \quad (6.80)$$

Now, using the field expansion (6.76) in terms of Rindler variables, we have that

$$\phi_k^M(t) = \int_{-\infty}^\infty dk' A(k, k') \phi_{k'}^R(\tau), \quad (6.81)$$

with the coefficient  $A(k, k')$  being

$$A(k, k') = \frac{1}{\pi} \int_0^\infty dx \sin(kx) e^{ik'\xi(x)} = \frac{1}{a\pi} \Gamma\left(1 + \frac{ik'}{a}\right) \cosh\left(\frac{\pi k'}{2a}\right) \left|\frac{k}{a}\right|^{-1 - i\frac{k'}{a}}, \quad (6.82)$$

where in order to solve the integral we utilize the Rindler transformations (6.1) to express  $\xi$  in terms of  $x$  for  $\tau = 0$ . Therefore, substituting equations (6.81) into (6.75), the Minkowski ground state wave functional can be written in terms of the Rindler field variables as

$$(\Psi^M)_0[\phi_{k'}^R, \phi_{k'}^{R*}, 0] = N_0 \exp\left(-\frac{I}{2}\right), \quad (6.83)$$

with  $N_0$  the properly normalization constant and with  $I$  given by the following integral

$$I = \int_0^\infty dk k \int_{-\infty}^\infty \int_{-\infty}^\infty dk' dk'' A(k, k') A(k, k'') \phi_{k'}^R \phi_{k''}^R. \quad (6.84)$$

Although the coefficient  $A(k, k')$  in equation (6.82) exhibits a complex form, this expression can be simplified through a more straightforward relation. In pursuit of this objective, first notice that we can explicitly express the coefficient  $I$  as

$$I = \int_{-\infty}^\infty \int_{-\infty}^\infty dk' dk'' \Gamma\left(1 + \frac{ik'}{a}\right) \Gamma\left(1 + \frac{ik''}{a}\right) \cosh\left(\frac{\pi k'}{2a}\right) \cosh\left(\frac{\pi k''}{2a}\right) \phi_{k'}^R \phi_{k''}^R \times J(k', k''), \quad (6.85)$$

with  $J(k', k'')$  an integral over  $k$

$$J(k', k'') = \frac{2}{\pi} \int_0^\infty \frac{dk}{2\pi k} \left(\frac{k}{a}\right)^{-i\frac{k'+k''}{a}}, \quad (6.86)$$

which can be reformulated in a more advantageous manner by observing that  $\left(\frac{k}{a}\right)^{-i\frac{k'+k''}{a}} = \exp\left\{-i\frac{k'+k''}{a} \ln\left(\frac{k}{a}\right)\right\}$ . Thus, through the substitution  $u = \ln\left(\frac{k}{a}\right)$ , we can represent the

coefficient  $J(k', k'')$  in terms of a delta function. Specifically,

$$J(k', k'') = \frac{2}{\pi} \delta\left(\frac{k' + k''}{a}\right) = \frac{2a}{\pi} \delta(k' + k''), \quad (6.87)$$

where we use the fact that  $\delta(\alpha x) = \delta(x)/|\alpha|$ . Introducing this result into equation (6.85) implicates that

$$I = \frac{2a}{\pi} \int_{-\infty}^{\infty} dk' \Gamma\left(1 + \frac{ik'}{a}\right) \Gamma\left(1 - \frac{ik'}{a}\right) \cosh^2\left(\frac{\pi k'}{2a}\right) \phi_{k'}^R \phi_{-k'}^R. \quad (6.88)$$

Now, taking into account the properties  $\Gamma(1 + y) = y\Gamma(y)$  and  $\Gamma(y)\Gamma(1 - y) = \pi/\sin(\pi y)$  concerning the gamma function, the following relation holds

$$\Gamma\left(1 + \frac{ik'}{a}\right) \Gamma\left(1 - \frac{ik'}{a}\right) = -i \frac{\pi k'/a}{\sin\left[\pi\left(1 + \frac{ik'}{a}\right)\right]} = \frac{\pi k'/a}{\sinh\left(\frac{\pi k'}{a}\right)}. \quad (6.89)$$

Hence, after all this calculation, the integral  $I$  can be simplified to

$$I = \int_{-\infty}^{\infty} dk' k' \coth\left(\frac{\pi k'}{2a}\right) \phi_{k'}^R \phi_{k'}^{R*}, \quad (6.90)$$

which provides the Minkowski vacuum in terms of Rindler variables in the  $t = \tau = 0$  hypersurface

$$(\Psi^M)_0[\phi_{k'}^R, \phi_{k'}^{R*}, 0] = N_0 \exp\left(-\int_0^{\infty} dk' k' \coth\left(\frac{\pi k'}{2a}\right) \phi_{k'}^R \phi_{k'}^{R*}\right), \quad (6.91)$$

where we take into consideration that the positive and negative values of  $k'$  have the same contribution for  $I$ . It should be noted that this form of  $(\Psi^M)_0$  is compatible with the normal mode decomposition for the wave functional previously mentioned in equation (6.61), where we can identify  $(\Psi_{k'}^M)_0$  as

$$(\Psi_{k'}^M)_0[\phi_{k'}^R, \phi_{k'}^{R*}, 0] = N_{k'} \exp\left(-k' \coth\left(\frac{\pi k'}{2a}\right) \phi_{k'}^R \phi_{k'}^{R*}\right), \quad (6.92)$$

with  $N_{k'}$  being the normalization constant for each mode. In this form, we can clearly see that the vacuums defined by equations (6.92) and (6.79) are essentially different for  $\tau = 0$ . However, in the limit of low accelerations, when  $\pi k'/2a \gg 1$ , both results become approximately equal. In fact, for this regime the conformal factor is almost 1, which says that there is no such difference between the Minkowski and Rindler perspectives.

Now, the temporal evolution of  $(\Psi_{k'}^M)_0$  on the Cauchy hypersurface defined in the accelerated frame is given in terms of the Schrödinger equation in this same referential,

namely equation (6.78), but considering (6.92) as initial condition. Therefore, a good ansatz for the vacuum wave functional is

$$(\Psi_k^M)_0[\phi_k^R, \phi_k^{R*}, \tau] = \mathcal{N}_k \exp\left(-k f_k(\tau) \phi_k^R \phi_k^{R*} + \Omega_k(\tau)\right), \quad (6.93)$$

where we have omitted the primes for the sake of clarity. Here,  $f_k(\tau)$  and  $\Omega_k(\tau)$  are complex coefficients with initial values settled as  $f_k(0) = \coth\left(\frac{\pi k}{2a}\right)$  and  $\Omega_k(0) = 0$ . Inserting this expression into Schrödinger equation (6.78) give us that

$$-ik \frac{\partial f_k(\tau)}{\partial \tau} |\phi_k^R|^2 + i \frac{\partial \Omega_k(\tau)}{\partial \tau} = k f_k(\tau) + (1 - f_k(\tau)^2) k^2 |\phi_k^R|^2, \quad (6.94)$$

which can be decomposed in two differential equations

$$-\frac{i}{k} \frac{\partial f_k(\tau)}{\partial \tau} = 1 - f_k^2(\tau) \quad \text{and} \quad \frac{\partial \Omega_k(\tau)}{\partial \tau} = -ik f_k(\tau), \quad (6.95)$$

having as respective solutions

$$f_k(\tau) = \coth\left(\frac{\pi k}{2a} + ik\tau\right) \quad (6.96)$$

and

$$\Omega_k(\tau) = -\ln\left[\sinh\left(\frac{\pi k}{2a} + ik\tau\right)\right], \quad (6.97)$$

where we absorb the integration constant coming from the equation for  $\Omega_k(\tau)$  in the normalization factor  $\mathcal{N}_k$ .

Lastly, in order to get a probabilistic interpretation for the wave functional we need to impose that  $\int |\Psi_k^M|^2 d\phi_k^R d\phi_k^{R*} = 1$ . For the ground state solution,

$$|(\Psi_k^M)_0|^2 = |\mathcal{N}_k|^2 \exp\left(-2k \Re[f_k(\tau)] |\phi_k^R|^2 + 2\Re[\Omega_k(\tau)]\right), \quad (6.98)$$

with  $\Re[f_k(\tau)]$  and  $\Re[\Omega_k(\tau)]$  representing the real part of the respective coefficients. Considering that the integral in question could be performed in terms of  $|\phi_k^R|$  and  $\arg(\phi_k^R)$ , we obtain as a normalization constant

$$\mathcal{N}_k = \sqrt{\frac{k \Re[f_k(\tau)]}{\pi}} e^{-\Re[\Omega_k(\tau)]}. \quad (6.99)$$

As a consequence, the Minkowski vacuum can be expressed as

$$(\Psi_k^M)_0[\phi_k^R, \phi_k^{R*}, \tau] = \sqrt{\frac{k\Re[f_k(\tau)]}{\pi}} \exp \left\{ -k\Re[f_k(\tau)]|\phi_k^R|^2 + i \left( -k\Im[f_k(\tau)]|\phi_k^R|^2 + \Im[\Omega_k(\tau)] \right) \right\}. \quad (6.100)$$

The explicit form of the real and imaginary parts of  $f_k(\tau)$  are, respectively,

$$\Re[f_k(\tau)] = \frac{\sinh\left(\frac{\pi k}{a}\right)}{\cosh\left(\frac{\pi k}{a}\right) - \cos(2k\tau)}, \quad \Im[f_k(\tau)] = \frac{-\sin(2k\tau)}{\cosh\left(\frac{\pi k}{a}\right) - \cos(2k\tau)}, \quad (6.101)$$

while for the  $\Omega_k(\tau)$  we have that

$$\Re[\Omega_k(\tau)] = -\frac{1}{2} \ln \left[ \cosh^2\left(\frac{\pi k}{2a}\right) - \cos^2(k\tau) \right], \quad \Im[\Omega_k(\tau)] = -\tan^{-1} \left( \coth\left(\frac{\pi k}{2a}\right) \tan(k\tau) \right). \quad (6.102)$$

Starting from equation (6.100), in the next section we will provide the Bohmian description for this vacuum state, deriving the Hamilton-Jacobi equation and the corresponding guidance equation, thereby identifying the individual contributions to the energy.

### 6.3.1 The de Broglie-Bohm approach

With the purpose of obtaining the de Broglie-Bohm approach for the Minkowski wave functional in Rindler variables, we need to identify the radial part and the phase from its polar form  $(\Psi_k^M)_0 = R_k e^{iS_k}$ . So, according to equation (6.100), we can see that

$$R_k(\phi_k^R, \phi_k^{R*}, \tau) = \sqrt{\frac{k\Re[f_k(\tau)]}{\pi}} \exp \left( -k\Re[f_k(\tau)]|\phi_k^R|^2 \right), \quad (6.103)$$

$$S_k(\phi_k^R, \phi_k^{R*}, \tau) = -k\Im[f_k(\tau)]|\phi_k^R|^2 + \Im[\Omega_k(\tau)]. \quad (6.104)$$

Since each  $(\Psi_k^M)_0$  obeys an independent Schrödinger equation, we can derive the Hamilton-Jacobi formalism for each mode individually, which enables us to extract information about the energy contributions much more easily. By employing the polar form of the ground state into Schrödinger equation obtained in Rindler space (equation (6.78)), and assuming that the modes  $\phi_k^R$  are indeed modes of the scalar field guided by the wave functional (6.100) and evolving in spacetime through the dBB guidance equations

$$\frac{\partial \phi_k^R}{\partial \tau} = \frac{\partial S_k}{\partial \phi_k^{R*}} = -k\Im[f_k(\tau)]\phi_k^R, \quad (6.105)$$

we once again arrive at a Hamilton-Jacobi equation and a continuity equation, but this time for each value of  $k$ . Specifically, we have that

$$\frac{\partial S_k}{\partial \tau} + \frac{\partial S_k}{\partial \phi_k^{R*}} \frac{\partial S_k}{\partial \phi_k^R} + k^2 |\phi_k^R|^2 - \frac{1}{R_k} \frac{\partial^2 R_k}{\partial \phi_k^R \partial \phi_k^{R*}} = 0, \quad (6.106)$$

$$\frac{\partial R_k^2}{\partial \tau} + \frac{\partial}{\partial \phi_k^R} \left( R_k^2 \frac{\partial S_k}{\partial \phi_k^{R*}} \right) + \frac{\partial}{\partial \phi_k^{R*}} \left( R_k^2 \frac{\partial S_k}{\partial \phi_k^R} \right) = 0. \quad (6.107)$$

As a result, the energy of each mode will consist of a classical term, composed by the kinetic energy and a classical potential energy, in addition to a quantum potential term. Taking into consideration the fact that the modes with wave numbers  $k$  and  $-k$  make equivalent contributions and are counted twice in (6.77), the effective contribution of each wave number need to be divided by 2 in the Hamilton-Jacobi equation (6.106). Therefore, we define

$$E_k(\tau) \equiv -\frac{1}{2} \left( \frac{\partial S_k}{\partial \tau} \right) = \frac{1}{2} \left( k \frac{\partial \Im[f_k(\tau)]}{\partial \tau} |\phi_k^R|^2 - \frac{\partial \Im[\Omega_k(\tau)]}{\partial \tau} \right), \quad (6.108)$$

$$K_k(\tau) \equiv \frac{1}{2} \left( \frac{\partial S_k}{\partial \phi_k^{R*}} \frac{\partial S_k}{\partial \phi_k^R} \right) = \frac{1}{2} \left( k^2 \Im^2[f_k(\tau)] |\phi_k^R|^2 \right), \quad (6.109)$$

$$V_k(\tau) \equiv \frac{1}{2} \left( k^2 |\phi_k^R|^2 \right), \quad (6.110)$$

$$Q_k(\tau) \equiv \frac{1}{2} \left( -\frac{1}{R_k} \frac{\partial^2 R_k}{\partial \phi_k^R \partial \phi_k^{R*}} \right) = \frac{1}{2} \left( k \Re[f_k(\tau)] - k^2 \Re^2[f_k(\tau)] |\phi_k^R|^2 \right), \quad (6.111)$$

with

$$E_k(\tau) = K_k(\tau) + V_k(\tau) + Q_k(\tau). \quad (6.112)$$

In the previous equations  $E_k$  represents the total energy of the system,  $K_k$  plays the role of kinetic energy, while  $V_k$  and  $Q_k$  denote the classical and quantum potential, respectively. An important observation is that such separation of terms in the total energy is allowed only in the dBB approach for quantum theory, not being possible in the usual interpretation. Also, when the quantum potential term is overwhelmed by the others, the classical evolution is restored.

The guidance equations (6.105) gives the dynamic evolution of the  $\phi_k^R$  modes in terms of the Rindler variable  $\tau$ , where each solution has an integration constant given by some initial condition, which are unknown and practically impossible to determine trough experiments. Nevertheless, if at some initial time  $\tau_0$  the initial conditions are distributed according to a probability density satisfying the Born rule, that is, with  $\mathcal{P}(\phi_k^R(\tau_0)) = R_k^2(\phi_k^R, \tau_0)$ , then equation (6.107) in addition with the guidance equations (6.105) guarantee that  $R_k^2(\phi_k^R, \tau)$  gives the probability density that the field mode has the value  $\phi_k^R$  at any time  $\tau$ , in such manner that all the statistical predictions of quantum theory are recovered.

So, equation (6.107) can then be understood as a continuity equation for an ensemble of field trajectories in configuration space with probability distribution  $P = R_k^2$  and velocity field given in Eq. (6.105). Now, if we use the explicit expressions of the real and imaginary parts of  $f_k(\tau)$  and  $\Omega_k(\tau)$  from equations (6.101) and (6.102), we obtain that

$$E_k(\tau) = \frac{1 - \cosh\left(\frac{\pi k}{a}\right) \cos(2k\tau)}{\left[\cosh\left(\frac{\pi k}{a}\right) - \cos(2k\tau)\right]^2} k^2 |\phi_k^R|^2 + \frac{k \sinh\left(\frac{\pi k}{a}\right)}{2 \left[\cosh\left(\frac{\pi k}{a}\right) - \cos(2k\tau)\right]}, \quad (6.113)$$

$$K_k(\tau) = \frac{\sin^2(2k\tau)}{2 \left[\cosh\left(\frac{\pi k}{a}\right) - \cos(2k\tau)\right]^2} k^2 |\phi_k^R|^2, \quad (6.114)$$

$$V_k(\tau) = \frac{1}{2} k^2 |\phi_k^R|^2, \quad (6.115)$$

$$Q_k(\tau) = \frac{\sinh\left(\frac{\pi k}{a}\right)}{2 \left[\cosh\left(\frac{\pi k}{a}\right) - \cos(2k\tau)\right]} k - \frac{\sinh^2\left(\frac{\pi k}{a}\right)}{2 \left[\cosh\left(\frac{\pi k}{a}\right) - \cos(2k\tau)\right]^2} k^2 |\phi_k^R|^2, \quad (6.116)$$

which explicitly depends on the mode  $\phi_k^R$ . As a consequence, the field trajectories can exhibit very distinct dynamics, with different solutions of the guidance equations leading to different values of energy, as well as different values of each one of its individual contributions.

Regarding the equations of motion, we can proceed similarly to what we did in section 6.2 and from the Hamilton-Jacobi equation (6.106) and the guidance equations (6.105), obtain a Klein-Gordon equation for the Bohmian field, with a source of quantum nature. Specifically, we have that

$$\frac{\partial^2 \phi_k^R}{\partial \tau^2} + k^2 \phi_k^R = -2 \frac{\partial Q_k}{\partial \phi_k^{R*}} = k^2 \Re^2[f_k(\tau)] \phi_k^R, \quad (6.117)$$

corresponding to a linear source that plays the role of an effective mass. In what follows we will calculate the average value of each term in the Hamilton-Jacobi equation and analyze the limits of low and high accelerations.

### 6.3.2 Mean values and Unruh temperature

As observed in the previous subsection, equations (6.105), (6.106), and (6.107) enable us to interpret  $|(\Psi_k^M)_0|^2 = R_k^2$  as the probability density of the Minkowski ground state associated with an ensemble of quantum trajectories determined by the guidance equations in Rindler space. As a result,

$$\langle \mathcal{O}(\tau) \rangle_{dBB} = \int d\phi_k^R d\phi_k^{R*} \left| \Psi_k^M(\phi_k^R, \phi_k^{R*}, \tau) \right|^2 \mathcal{O}(\phi_k^R, \phi_k^{R*}, \tau) \quad (6.118)$$

is the mean value in dBB interpretation of a physically meaningful property  $\mathcal{O}$  related to the field trajectories (see equation (6.53)). For the Hamiltonian operator  $\hat{H}_k$ , its mean value is shown to be identical to the mean value of the property  $\mathcal{O} = E_k$  defined in equation (6.108), which shows the necessity of considering the contribution of the quantum potential in the calculation. Hence, according to equation (6.112), the mean energy  $\langle E_k \rangle_{dBB}$  can be expressed as

$$\langle E_k \rangle_{dBB} = \langle K_k \rangle_{dBB} + \langle V_k \rangle_{dBB} + \langle Q_k \rangle_{dBB}, \quad (6.119)$$

being the sum of the mean values of each term present in Hamilton-Jacobi equation.

Given that equations (6.108-6.111) depend on  $|\phi_k^R|^2$  and taking into account that

$$|(\Psi_k^M)_0|^2 = \frac{k\Re[f_k(\tau)]}{\pi} e^{-2k\Re[f_k(\tau)]|\phi_k^R|^2}, \quad (6.120)$$

the computation of the mean values in (6.119) is reduced to the calculus of the following integrals:

$$\begin{aligned} I_1 &= v_k(\tau) \int d\phi_k^R d\phi_k^{R*} |(\Psi_k^M)_0|^2, \\ I_2 &= \Upsilon_k(\tau) \int d\phi_k^R d\phi_k^{R*} |\phi_k^R|^2 e^{-2k\Re[f_k(\tau)]|\phi_k^R|^2}, \end{aligned} \quad (6.121)$$

with  $v_k(\tau)$  and  $\Upsilon_k(\tau)$  general functions depending on the property  $\mathcal{O}$  in question. Because of the normalization condition, the first integral is trivial. In relation to the second one, using the polar form of  $\phi_k^R$  and remembering the fact that  $\int_0^\infty d\rho \rho^3 e^{-c\rho^2} = \frac{1}{2c^2}$ , with  $\rho = |\phi_k^R|$  and  $c = 2k\Re[f_k(\tau)]$ , we have that

$$I_1 = v_k(\tau) \quad \text{and} \quad I_2 = \frac{\pi}{2k^2} \frac{\Upsilon_k(\tau)}{\Re^2[f_k(\tau)]}. \quad (6.122)$$

In the case of the total energy  $E_k$  given by equation (6.108), for instance,  $\langle E_k \rangle_{dBB} = I_1 + I_2$ , with  $v_k(\tau) = -\frac{1}{2} \frac{\partial \Im[\Omega_k(\tau)]}{\partial \tau}$  and  $\Upsilon_k(\tau) = \frac{k^2}{2\pi} \Re[f_k(\tau)] \frac{\partial \Im[f_k(\tau)]}{\partial \tau}$ . Hence,

$$\langle E_k \rangle_{dBB} = \frac{k}{2} \coth\left(\frac{\pi k}{a}\right) = k \left( \frac{1}{2} + \frac{1}{e^{\frac{2\pi}{a}k} - 1} \right). \quad (6.123)$$

This result can be further examined to derive the average number of Rindler particles within the Minkowski vacuum taking advantage of the fact that the Hamilton operator can be expressed in terms of the number operator as  $\hat{H}_k = (\hat{n}_k + \frac{1}{2})k$ . Consequently,

$\langle n_k \rangle_{dBB} = \frac{1}{k} \langle E_k \rangle_{dBB} - \frac{1}{2}$ , yielding,

$$\langle n_k \rangle_{dBB} = \frac{1}{e^{\frac{2\pi}{a}k} - 1}, \quad (6.124)$$

which is the mean number corresponding to a Bose-Einstein distribution with Unruh temperature  $T = a/2\pi$ . This demonstrates that within the Bohmian formalism, we are also capable of reproducing such effect.

In a parallel fashion, we can calculate the average values of the different parts of the energy, which lead us to

$$\langle K_k \rangle_{dBB} = \frac{k \Im^2[f_k(\tau)]}{4 \Re[f_k(\tau)]} = \frac{k \operatorname{csch}\left(\frac{\pi k}{a}\right) \sin^2(2k\tau)}{4 \left[ \cosh\left(\frac{\pi k}{a}\right) - \cos(2k\tau) \right]}, \quad (6.125)$$

$$\langle V_k \rangle_{dBB} = \frac{k}{4} \frac{1}{\Re[f_k(\tau)]} = \frac{k \left[ \cosh\left(\frac{\pi k}{a}\right) - \cos(2k\tau) \right]}{4 \sinh\left(\frac{\pi k}{a}\right)}, \quad (6.126)$$

$$\langle Q_k \rangle_{dBB} = \frac{k}{4} \Re[f_k(\tau)] = \frac{k \sinh\left(\frac{\pi k}{a}\right)}{4 \left[ \cosh\left(\frac{\pi k}{a}\right) - \cos(2k\tau) \right]}. \quad (6.127)$$

Note that each one of the above expressions has a non-trivial time dependence, however their sum, the total mean energy, is completely time-independent. It is interesting to examine the behavior of these quantities under different acceleration values. Figure (6.2) presents plots of the Bohmian averages as functions of the acceleration  $a$ , where we observe two distinct moments:  $\tau = 0$  and  $\tau = \pi/2$ . We observe that for low accelerations, the classical and quantum potentials exhibit close magnitudes in both cases. However, as the acceleration increases, Figure (6.2a) illustrates the average quantum potential tending asymptotically to  $\langle E_k \rangle_{dBB}$ , whereas in Figure (6.2b), the classical potential primarily governs the mean energy as the dominant factor. In the upcoming section, we shall explore the temporal dependence of the mean values in the low and high acceleration limits, studying the transitions between quantum and classical dominances.

### 6.3.3 Low and high temperature regimes

#### Low acceleration limit:

Let us initiate this analysis by considering the limit where  $\frac{\pi k}{a} \gg 1$ , which can be attained in the regime of low accelerations (temperatures). Under these circumstances,

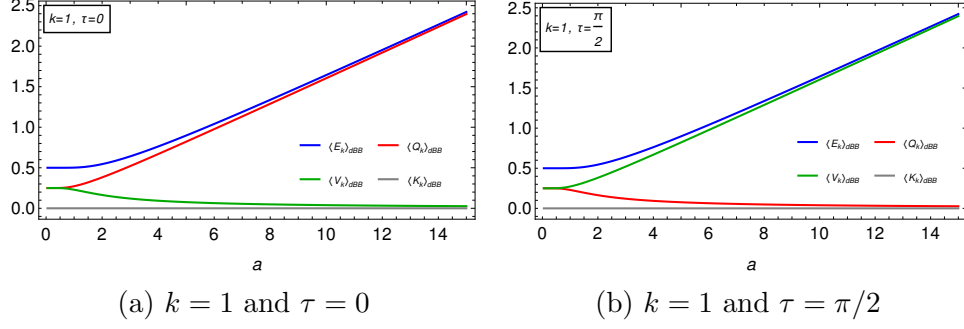


Figure 6.2: The Bohmian averages as functions of the acceleration parameter  $a$  for  $\tau = 0$  and  $\tau = \pi/2$ . While for low accelerations, the quantum and classical potentials are equivalents, in the high acceleration limit we have very distinct behaviors.

the coefficients  $f_k(\tau)$  and  $\Omega_k(\tau)$ , as given by equations (6.101) and (6.102), are such that

$$\begin{aligned} \Re[f_k(\tau)] &\approx 1, & \Im[f_k(\tau)] &\approx 0, \\ \Re[\Omega_k(\tau)] &\approx -\frac{k}{4T}, & \Im[\Omega_k(\tau)] &\approx -k\tau. \end{aligned} \quad (6.128)$$

As a consequence, we obtain the following approximation for the wave functional (6.100):

$$(\Psi_k^M)_0[\phi_k^R, \phi_k^{R*}, \tau] \approx \sqrt{\frac{k}{\pi}} e^{-k|\phi_k^R|^2 - ik\tau}, \quad (6.129)$$

which is exactly equal to the Rindler vacuum  $(\Psi_k^R)_0$  given in equation (6.79). This is an expected result, as when we approach this limit, the accelerated observer can be considered as an inertial one, resulting in little differentiation between the Rindler and Minkowski representations. Therefore, the vacuum descriptions in both frameworks are equivalent.

In the context of equations (6.108-6.111), the low acceleration regime recovers the expressions for the total energy of the Minkowski vacuum and its parts in the dBB interpretation, that is,  $E_k \approx k/2$ ,  $K_k \approx 0$ , and  $Q_k \approx k/2 - V_k$ . On the other hand, the guidance equation (6.105) becomes  $\partial_\tau \phi_k^R \approx 0$ , implying in a set of static trajectories where  $\phi_k^R(\tau) = \phi_k^R(0)$ . In relation to the average values, we have that

$$\langle K_k \rangle_{dBB} \approx k \sin^2(2k\tau) e^{-k/T} \approx 0, \quad (6.130)$$

$$\langle V_k \rangle_{dBB} \approx \frac{k}{4} - \frac{k \cos(2k\tau) e^{-k/(2T)}}{2} \approx \frac{k}{4}, \quad (6.131)$$

$$\langle Q_k \rangle_{dBB} \approx \frac{k}{4} + \frac{k \cos(2k\tau) e^{-k/(2T)}}{2} \approx \frac{k}{4}, \quad (6.132)$$

$$\langle E_k \rangle_{dBB} \approx \frac{k}{2}, \quad (6.133)$$

meaning that the energy of the field is equally shared between the classical and quantum potential, with the energy average being precisely the energy of a single harmonic oscillator

with wave number  $k = \hbar\omega$  in the ground state, that is,  $\langle E_k \rangle_{dBB} = k/2$ . Thus, the Bohmian approach of the Rindler vacuum restores the same results of the massless scalar field in Minkowski space in its ground state, which is a robust consistent test of our findings.

**High acceleration limit:**

Let us now consider the limit where  $\frac{\pi k}{a} \ll 1$ , which can be achieved in the regime of high accelerations (temperatures). In this scenario, two distinct moments need to be highlighted:

**i)  $\tau \neq n\pi/k$ , with  $n$  an integer (classical dominance)**

In this case, the coefficients  $f_k(\tau)$  and  $\Omega_k(\tau)$  admit the subsequent expansions:

$$\begin{aligned} \Re[f_k(\tau)] &\approx \frac{k}{4T \sin^2(k\tau)}, & \Im[f_k(\tau)] &\approx -\cot(k\tau), \\ \Re[\Omega_k(\tau)] &\approx \ln \sqrt{2} - \frac{1}{2} \ln(1 - \cos(2k\tau)), & \Im[\Omega_k(\tau)] &\approx -\frac{\pi}{2} \text{sign}(\tan(k\tau)), \end{aligned} \quad (6.134)$$

where  $T$  is the Unruh temperature. Therefore, this allows us to approximate the wave functional as

$$\begin{aligned} (\Psi_k^M)_0[\phi_k^R, \phi_k^{R*}, \tau] &\approx \frac{k}{\sqrt{4\pi T} |\sin(k\tau)|} \exp \left\{ -\frac{k^2}{4T \sin^2(2k\tau)} |\phi_k^R|^2 \right\} \times \\ &\exp \left\{ ik \cot(k\tau) |\phi_k^R|^2 - i\frac{\pi}{2} \text{sign}(\tan(k\tau)) \right\}. \end{aligned} \quad (6.135)$$

An interesting point is that the Bohmian averages are primarily governed by the classical parts when  $\tau \neq \frac{n\pi}{k}$ , with a negligible contribution from the quantum potential. This can be seen by using the expansions (6.134) in equations (6.125-6.127). As a result,

$$\langle K_k \rangle_{dBB} \approx T \cos^2(k\tau), \quad (6.136)$$

$$\langle V_k \rangle_{dBB} \approx T \sin^2(k\tau), \quad (6.137)$$

$$\langle Q_k \rangle_{dBB} \approx \frac{k^2}{16T \sin^2(k\tau)} \approx 0, \quad (6.138)$$

$$\langle E_k \rangle_{dBB} \approx T, \quad (6.139)$$

with  $\langle K_k \rangle_{dBB}$  and  $\langle V_k \rangle_{dBB}$  being oscillatory functions that dictate the field dynamics. Please note that the total mean energy  $\langle E_k \rangle_{dBB}$  is exactly the energy of a thermal distribution of oscillators at temperature  $T$ , in complete agreement with the equipartition theorem.

**ii)  $\tau = n\pi/k$ , with  $n$  an integer (quantum dominance)**

In the majority part of the time, the total mean energy is primarily determined by the

classical contributions. However, the situation changes significantly when  $\tau$  approaches  $n\pi/k$ , with  $n$  being an integer. In this case, we have that

$$\begin{aligned}\Re[f_k(\tau)] &\approx \frac{4T}{k}, & \Im[f_k(\tau)] &= 0, \\ \Re[\Omega_k(\tau)] &\approx \ln\left(\frac{4T}{k}\right), & \Im[\Omega_k(\tau)] &= 0,\end{aligned}\tag{6.140}$$

with the wave functional having the simple form

$$(\Psi_k^M)_0[\phi_k^R, \phi_k^{R*}, \tau] \approx \sqrt{\frac{4T}{\pi}} \exp\left\{-4T|\phi_k^R|^2\right\}.$$

Then, the mean values are just

$$\langle K_k \rangle_{dBB} \approx 0,\tag{6.141}$$

$$\langle V_k \rangle_{dBB} \approx \frac{k^2}{16T} \approx 0,\tag{6.142}$$

$$\langle Q_k \rangle_{dBB} \approx T,\tag{6.143}$$

$$\langle E_k \rangle_{dBB} \approx T,\tag{6.144}$$

showing the dominance of the quantum potential over the negligible values of the classical contributions. This result reveals that the total mean energy is constant, but there is a notable transition from classical to quantum contributions occurring periodically at  $\tau = n\pi/k$ , which instigates us to think about the possibility of measuring such an effect.

To illustrate such phenomenon, in Figure [6.3](#) we plot the graphic of the mean energy, along with its classical and quantum components, for two distinct scenarios: one with an intermediate acceleration ( $a = 1$ ), highlighting the non-trivial temporal variations of the individual terms present in Hamilton-Jacobi equation, and another with a high value of the acceleration ( $a = 100$ ), where we show the sum of the classical energies together with the quantum potential. In the latter, it is possible to observe the periodic abrupt transitions from classical to quantum dominance in the vicinity of  $\tau = n\pi/k$ .

As a matter of fact, these abrupt changes can be seen already in the effective Klein-Gordon equation for the Bohmian field (equation [\(6.117\)](#)). In the high temperature regime and for  $\tau \neq n\pi/k$ , is valid the approximation

$$\frac{\partial^2 \phi_k^R}{\partial \tau^2} + k^2 \phi_k^R \approx \frac{k^4}{16T^2 \sin^2(k\tau)} \phi_k^R \approx 0; \quad \tau \neq n\pi/k.\tag{6.145}$$

So, the quantum force is negligible, and the Bohmian field obeys a classical Klein-Gordon

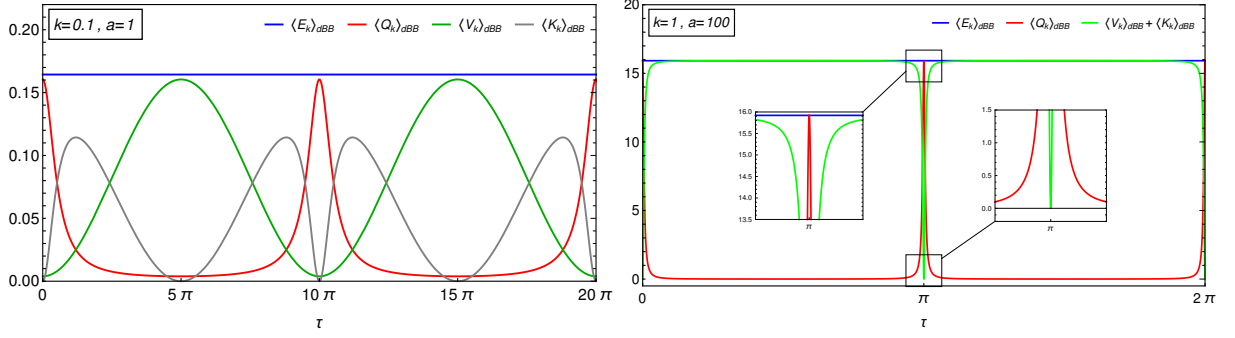


Figure 6.3: *Left:* Average values for  $a = 1$  and  $k = 0.1$ . We observe a quantum dominance around  $\tau = n\pi/k$ , although the classical terms remain relevant. *Right:* Average values for  $a = 100$  and  $k = 1$ . In the vicinity of  $\tau = n\pi/k$ , there is an abrupt transition between the classical ( $\langle V_k \rangle_{dB B} + \langle K_k \rangle_{dB B}$ ) and quantum ( $\langle Q_k \rangle_{dB B}$ ) contributions. The quantum potential rapidly becomes the dominant part of  $\langle E_k \rangle_{dB B}$  as the classical terms suddenly drop to zero.

equation. For  $\tau = n\pi/k$ , on the other hand, we obtain that

$$\frac{\partial^2 \phi_k^R}{\partial \tau^2} + k^2 \phi_k^R \approx 16T^2 \phi_k^R; \quad \tau = n\pi/k, \quad (6.146)$$

indicating that the quantum force drives the field dynamics. Hence, also in this perspective, there is a substantial change from classical to quantum dominance in the vicinity of  $\tau = n\pi/k$ . Since the field dynamics are very different for these two distinct moments, it allows us to speculate whether such an effect can be observed.

### 6.3.4 Field Trajectories

In this subsection, we derive the general solution to the guidance equations, obtaining the ensemble of possible field trajectories. Among them, we highlight one particularly remarkable trajectory with astonishing properties and study its behavior under both low and high acceleration conditions.

By using the expression (6.101) for  $\Im[f_k(\tau)]$ , we can integrate the guidance equation (6.105), resulting in the following field trajectory

$$\phi_k^R(\tau) = C_k(a) \sqrt{\cosh\left(\frac{\pi k}{a}\right) - \cos(2k\tau)}, \quad (6.147)$$

that can be presented in a more convenient form if we write the integration constant  $C_k(a)$  as  $C_k(a) = D_k(a)/[2k \sinh((\pi k/a))]^{1/2}$ . By doing so,

$$\phi_k^R(\tau) = \frac{D_k(a)}{\sqrt{2k \Re[f_k(\tau)]}} = D_k(a) \sqrt{\frac{\cosh\left(\frac{\pi k}{a}\right) - \cos(2k\tau)}{2k \sinh\left(\frac{\pi k}{a}\right)}}. \quad (6.148)$$

As a result, the probability distribution associated with the field trajectories, namely  $|(\Psi_k^M)_0|^2$ , admits a very simple form: the Gaussian distribution  $|(\Psi_k^M)_0|^2 \propto e^{-|D_k(a)|^2}$ . Moreover, each trajectory will possess an energy configuration that depends on the constant  $D_k(a)$ ,

$$E_k = k \frac{|D_k(a)|^2 - 1 + \cosh\left(\frac{\pi k}{a}\right) \left[ \cosh\left(\frac{\pi k}{a}\right) - |D_k(a)|^2 \cos(2k\tau) \right]}{2 \left[ \cosh\left(\frac{\pi k}{a}\right) - \cos(2k\tau) \right] \sinh\left(\frac{\pi k}{a}\right)}. \quad (6.149)$$

An immediate consequence of this result is that the total energy of the Bohmian fields will be time-independent if, and only if, we choose  $D_k(a)$  such that  $|D_k(a)|^2 = 1$ . This condition is achieved when  $D_k(a) = \exp(i\theta_k(a))$ , with  $\theta_k(a)$  being a real constant. For this subset of initial conditions, disregarding the normalization factor, the probability distribution  $|(\Psi_k^M)_0|^2 \propto e^{-|D_k(a)|^2}$  is fixed and does not depend on either  $k$  or  $a$ . Additionally to this fact, the energy configuration arising from this choice precisely corresponds to the mean energy (6.123), that is,

$$E_k = k \left( \frac{1}{2} + \frac{1}{e^{\frac{2\pi k}{a}} - 1} \right). \quad (6.150)$$

Furthermore, these specific field trajectories exhibit a noteworthy property: each component of their total energy exactly matches the average values of their respective contributions, that is,  $Q_k = \langle Q_k \rangle_{dBB}$ ,  $V_k = \langle V_k \rangle_{dBB}$ , and  $K_k = \langle K_k \rangle_{dBB}$  (see equations (6.127), (6.126), and (6.125)). Thus, the examination of the asymptotic limits of the mean quantities, as discussed in the preceding subsection, applies to all the Bohmian fields characterized by  $D_k(a) = \exp(i\theta_k(a))$ , including the sudden transitions from classical to quantum dominance occurring periodically at  $\tau = n\pi/k$ . These particular Bohmian fields follow the mean value evolution exactly. As far as we know, this is the first time that non-static Bohmian field trajectories with such characteristics are exhibited.

Lastly, the asymptotic behaviors of these particular Bohmian fields, disregarding their phase, read

$$\phi_k^R = \frac{1 - \cos(2k\tau)e^{-k/(2T)}}{\sqrt{2k}}, \quad T \ll 1 \quad (6.151)$$

$$\phi_k^R = \frac{\sqrt{2T} |\sin(2k\tau)|}{k}, \quad T \gg 1 \quad (6.152)$$

In order to present a proper visualization of these Bohmian trajectories, in Figure 6.4 we plot the graphics of the Bohmian fields (6.148) as functions of  $\tau$ , considering  $\theta_k(a) = 0$ , since the phase dependence is quite trivial. We consider the cases where  $a = 0.1$ ,  $a = 1$ ,  $a = 10$ , and  $a = 100$ , with each curve representing a different value of the wave

number. We observe static trajectories in the low-temperature regime, in agreement with the results in the last subsection. On the other hand, the field trajectories exhibit non-trivial behavior for high-temperatures, indicating that they become more dynamic as temperature (acceleration) increases.

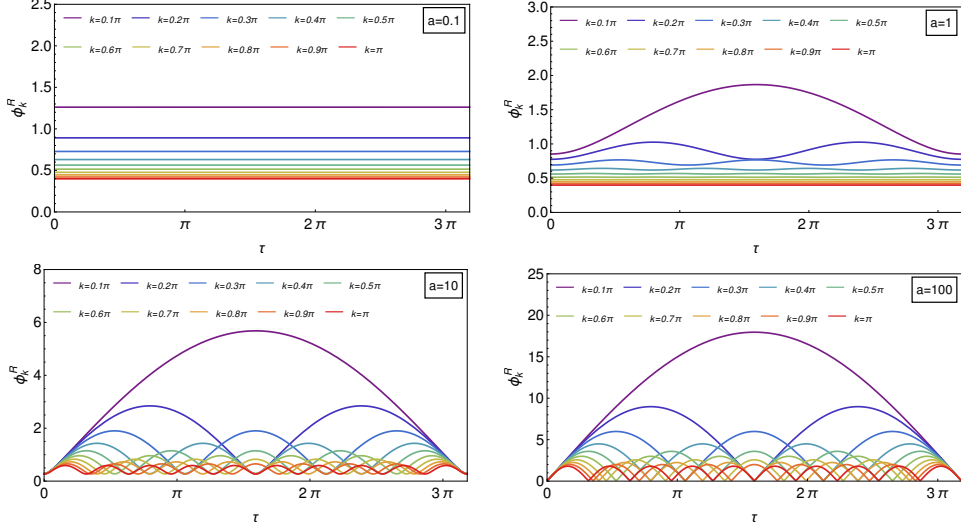


Figure 6.4: The Bohmian trajectories (6.148) as functions of time. Each curve represents a different value of the parameter  $k$ . For low temperatures we have static trajectories, whereas in the high-temperature regime the field has a non-trivial behavior.

### 6.3.5 Power Spectrum

An important property that provides us with statistical insights is the power spectrum, defined as

$$P_k(\tau) = \int d\xi e^{-ik\xi} \langle \phi(\xi)\phi(0) \rangle_{dBB}. \quad (6.153)$$

Here,  $\langle \phi(\xi)\phi(0) \rangle_{dBB}$  is the two-point correlation function, calculated in dBB interpretation as an average over all the field configurations. Assuming the quantum equilibrium hypotheses for the initial conditions, it is possible to establish the equivalence between the two-point function in the dBB interpretation and the one calculated in the usual manner [196], which can be expressed as

$$\langle \phi(\tau, \xi)\phi(\tau, \xi + \sigma) \rangle_{dBB} = \langle \phi(\tau, \xi)\phi(\tau, \xi + \sigma) \rangle, \quad (6.154)$$

with

$$\langle \phi(\tau, \xi)\phi(\tau, \xi + \sigma) \rangle = \frac{\int \mathcal{D}\phi |\Psi(\phi(\tau, \xi))|^2 \phi(\xi)\phi(\xi + \sigma)}{\int \mathcal{D}\phi |\Psi(\phi(\tau, \xi))|^2}. \quad (6.155)$$

The integration measure is expressed as  $\mathcal{D}\phi \equiv \prod_k d\phi_k^R$ , and we consider the ground state wave functional  $(\Psi^M)_0 = \prod_{k>0} (\Psi_k^M)_0$  (equation (6.61)) to evaluate the correlations associated with the Minkowski vacuum. Using the Fourier decomposition (6.76) in terms of Rindler variables, the two-point function assumes the non-trivial form

$$\langle \phi(\tau, \xi) \phi(\tau, \xi + \sigma) \rangle = \frac{\int \int_{-\infty}^{+\infty} \frac{d\bar{k}d\bar{k}'}{2\pi} e^{i(\bar{k}+\bar{k}')\xi} e^{i\bar{k}'\sigma} \int \prod_{k''} d\phi_{k''}^R \prod_{k>0} |(\Psi_k^M)_0|^2 \phi_k^R \phi_{\bar{k}'}^R}{\int \prod_{k''} d\phi_{k''}^R \prod_{k>0} |(\Psi_k^M)_0|^2}. \quad (6.156)$$

The probability distribution  $|(\Psi^M)_0|^2 = \prod_{k>0} |(\Psi_k^M)_0|^2$  is proportional to  $e^{-2\int_0^\infty k \Re[f_k(\tau)] \phi_k^R \phi_{-k}^R}$  (see equation (6.120)), with  $\phi_k^{R*} = \phi_{-k}^R$ . So, if we define the operator

$$\mathcal{O}(k, k') \equiv -(|k||k'| \Re[f_k(\tau)] \Re[f_{k'}(\tau)])^{1/2} \delta(k + k'), \quad (6.157)$$

the integral in the exponential is conveniently written as

$$-2 \int_0^{+\infty} dk k \Re[f_k(\tau)] \phi_k^R \phi_{-k}^R = \int_{-\infty}^{+\infty} \int_{-\infty}^{+\infty} dk dk' \phi_k^R \mathcal{O}(k, k') \phi_{k'}^R. \quad (6.158)$$

The advantage of such definition is that it permits us to evaluate the integral in the Rindler modes in terms of the generating functional

$$Z[j_k] = \int \prod_k d\phi_k^R \exp \left( \int_{-\infty}^{+\infty} \int_{-\infty}^{+\infty} dk dk' \phi_k^R \mathcal{O}(k, k') \phi_{k'}^R + \int_{-\infty}^{+\infty} dk \phi_k^R j_k \right). \quad (6.159)$$

In fact,

$$\left. \frac{\delta^2 Z[j_{k''}]}{\delta j_{\bar{k}} \delta j_{\bar{k}'}} \right|_{j_{k''}=0} = \int \prod_{k''} d\phi_{k''}^R \exp \left( \int_{-\infty}^{+\infty} \int_{-\infty}^{+\infty} dk dk' \phi_k^R \mathcal{O}(k, k') \phi_{k'}^R \right) \phi_{\bar{k}}^R \phi_{\bar{k}'}^R. \quad (6.160)$$

Thus, the two-point function is simplified to

$$\langle \phi(\tau, \xi) \phi(\tau, \xi + \sigma) \rangle = \frac{\int_{-\infty}^{+\infty} \int_{-\infty}^{+\infty} \frac{d\bar{k}d\bar{k}'}{2\pi} e^{i(\bar{k}+\bar{k}')\xi} e^{i\bar{k}'\sigma} \left. \frac{\delta^2 Z[j_{k''}]}{\delta j_{\bar{k}} \delta j_{\bar{k}'}} \right|_{j_{k''}=0}}{Z[0]}. \quad (6.161)$$

The derivatives of the generating functional are determined by implementing the change of variables  $\phi_k^R = \tilde{\phi}_k^R - \frac{1}{2} \int dk' \mathcal{O}^{-1}(k, k') j_{k'}$ , where  $\mathcal{O}^{-1}$  is the inverse operator

$$\mathcal{O}^{-1}(k, k') = -\frac{\delta(k + k')}{|k| \Re[f_k(\tau)]}. \quad (6.162)$$

After simplification, we obtain that

$$\int \int dkdk' \phi_k^R \mathcal{O}(k, k') \phi_{k'}^R + \int dk \phi_k^R j_k = \int \int dkdk' \tilde{\phi}_k^R \mathcal{O}(k, k') \tilde{\phi}_{k'}^R - \frac{1}{4} \int dkdk' \mathcal{O}^{-1}(k, k') j_k j_{k'}, \quad (6.163)$$

where all the integrals are performed from minus infinity to infinity. Thus, the generating functional becomes

$$Z[j] = \mathcal{N} \exp \left( -\frac{1}{4} \int_{-\infty}^{+\infty} \int_{-\infty}^{+\infty} dkdk' \mathcal{O}^{-1}(k, k') j_k j_{k'} \right), \quad (6.164)$$

with  $\mathcal{N} = \int \prod_{k''} d\tilde{\phi}_{k''}^R \exp \left( \int_{-\infty}^{+\infty} \int_{-\infty}^{+\infty} dkdk' \tilde{\phi}_k^R \mathcal{O}(k, k') \tilde{\phi}_{k'}^R \right)$ . As a consequence,

$$\left. \frac{\delta^2 Z[j_{k''}]}{\delta j_{\bar{k}} \delta j_{\bar{k}'}} \right|_{j_{k''}=0} = -\frac{1}{2} Z[0] \mathcal{O}^{-1}(\bar{k}, \bar{k}'). \quad (6.165)$$

Inserting this expression into equation (6.161) and using (6.162), we derive the simplified form of the two-point function:

$$\langle \phi(\tau, \xi) \phi(\tau, \xi + \sigma) \rangle = \frac{1}{2\pi} \int_{-\infty}^{+\infty} dk \frac{e^{-ik\sigma}}{2|k| \Re[f_k(\tau)]}. \quad (6.166)$$

With this result at our disposal, we can finally calculate the power spectrum (6.153) by setting  $\xi + \sigma = 0$ , yielding

$$P_k(\tau) = \frac{1}{2k \Re[f_k(\tau)]} = \frac{\cosh\left(\frac{\pi k}{a}\right) - \cos(2k\tau)}{2k \sinh\left(\frac{\pi k}{a}\right)} = \frac{2}{k^2} \langle V_k \rangle_{dB B}. \quad (6.167)$$

Therefore, the correlations between the field modes appear to be closely connected to the average classical potential, raising the possibility that this could be a purely classical effect, without any contribution coming from the quantum potential. This suggests that this quantity may not be the ideal candidate for observing prominent quantum effects. Nonetheless, this result is a novelty since such conclusion was only possible because of the Bohmian interpretation's unique capability to separate the individual components of the energy, allowing us to distinguish between contributions of quantum and classical nature. Perhaps distributions outside the quantum equilibrium hypothesis may generate different outcomes. For example, in reference [197] is argued that quantum black holes can violate the Born rule, potentially impacting the Hawking radiation. So, the simple model we have explored here could serve as a starting point for further investigations into this intriguing possibility.

In the regime of high temperatures the power spectrum can be approximated by

$$P_k(\tau) \approx \frac{2T}{k^2} \sin^2(k\tau), \quad T \gg 1 \quad (6.168)$$

while for low temperatures it is independent of time, with

$$P_k(\tau) \approx \frac{1}{2k}. \quad T \ll 1 \quad (6.169)$$

It is important to highlight that the results presented in this section are specific to the scenario of a single spatial dimension. In cases involving two or more spatial dimensions, the wave functional displays different dependencies on longitudinal and transverse momenta with respect to the acceleration direction, as indicated in [191, 181]. While the Bose-Einstein distribution remains applicable, it is notable that certain quantities lose their rotational invariance in this context, such as the Bogoliubov coefficients [181] and even the wave functional itself [191]. In the next section we will start the complete manifold analysis.

## 6.4 The complete manifold problem

In the last section, we presented the Bohmian description of the Minkowski vacuum in Rindler variables obtained for region I in the spacetime diagram shown in Figure 6.1 ( $-x < t < x$  and  $x > 0$ ), involving a half-Fourier transform of the scalar field in terms of Minkowski variables (equation (6.71)). To describe the vacuum associated with the entire Minkowski space, we introduce a new set of Rindler variables that covers the left side as well, providing an analytical extension for the Rindler modes. These two-wedge coordinates are

$$\begin{aligned} \text{RR-wedge } (x > 0): \quad & \text{LR-wedge } (x < 0): \\ x = \frac{e^{a\xi_R}}{a} \cosh(a\tau) \quad & x = -\frac{e^{a\xi_L}}{a} \cosh(a\tau) \\ t = \frac{e^{a\xi_R}}{a} \sinh(a\tau) \quad & t = -\frac{e^{a\xi_L}}{a} \sinh(a\tau). \end{aligned} \quad (6.170)$$

In Figure 6.5 bellow, we represent this set of coordinates. Region I, where  $-x < t < x$  and  $x > 0$ , corresponds to the right-wedge problem studied in the last section. As we saw, in this region  $\partial_\tau$  is the timelike Killing vector associated with temporal translations. On the other hand, in region IV of the diagram, where  $x < t < -x$  and  $x < 0$ , the associated timelike Killing vector is  $\partial_{-\tau} = -\partial_\tau$ , which is past-directed. This means that

as  $\tau$  increases, the temporal variable  $t$  decreases, with this region referred as left-Rindler wedge.

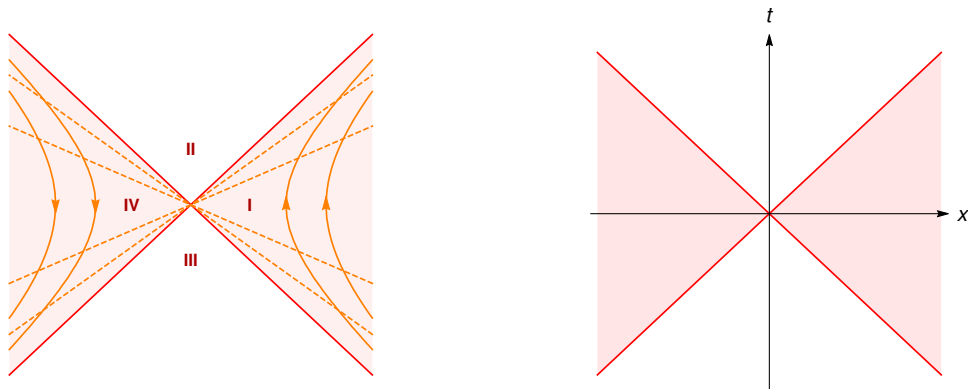


Figure 6.5: Diagram for the two-wedges problem. The right-Rindler wedge (region I) is the same one presented in the last section. The left-Rindler wedge (region IV) is a time-reversed copy of region I, with past-directed evolution (thick curves). The dashed lines represent the hypersurfaces of constant time.

The diagram of the two-wedge geometry is quite similar to what occurs in the black hole situation, since the time evolves in opposite directions in the timelike regions I and IV, which exhibit similar characteristics to those observed in the extended Schwarzschild geometry. Additionally, regions II and III are causally analogous to a black hole and a white hole, respectively, with the horizons identified as  $t = \pm x$ . Therefore, the study of the de Broglie-Bohm analysis of the two-wedge problem can pave the way to the understanding of quantum effects associated with black holes according to this interpretation. Moreover, the two-wedge perspective introduces novel characteristics to the Unruh effect, with manifestation also in Hawking radiation. For example, it establishes a non-local connection between the fields defined in distinct wedges [198]. Given that the Bohmian mechanics is inherently non-local, this alternative perspective offers an intriguing point of view that holds potential for future investigations. In this section we will address the Unruh effect for the complete manifold problem, focusing on the two-wedge scalar massless field in  $(1 + 1)$ -dimensions, giving the de Broglie-Bohm's description.

#### 6.4.1 The vacuum wave functional for the two-wedge problem

We will follow the steps presented in the first part of section 6.3 and derive the wave functional of the Minkowski vacuum in Rindler variables considering the right and left wedges. In section 6.2, we saw that the ground state wave functional is (equation (6.64))

$$(\Psi^M)_0[\phi_k^M, \phi_k^{M*}, t] = \left\{ \prod_k \left( \frac{\omega_k}{\pi} \right)^{1/4} \right\} \exp \left( -\frac{1}{2} \int_{-\infty}^{\infty} |k| |\phi_k^M|^2 dk \right) e^{-i\Omega_0 t}, \quad (6.171)$$

where, this time, we have assumed the complete Fourier decomposition of the field, that is,

$$\phi(t, x) = \int_{-\infty}^{\infty} \frac{dk}{\sqrt{2\pi}} e^{ikx} \phi_k^M(t), \quad (6.172)$$

with  $\phi_k^{M*} = \phi_{-k}^M$  because the reality of  $\phi$ . So, in an effort to obtain the Rindler description of the Minkowski vacuum, we must provide the appropriate expansion of the scalar field in Rindler modes, where it is essential to consider both wedges to cover the right and left sides. Specifically, we have that

$$\phi(\tau, \xi) = \theta(x) \int_{-\infty}^{\infty} \frac{dk}{\sqrt{2\pi}} e^{ik\xi_R} \phi_k^R(\tau) + \theta(-x) \int_{-\infty}^{\infty} \frac{dk}{\sqrt{2\pi}} e^{ik\xi_L} \phi_k^L(\tau), \quad (6.173)$$

with  $\xi_R$  and  $\xi_L$  the Rindler coordinates defined in (6.170).

Inverting equation (6.172) allows us to express  $\phi_k^M$  in terms of  $\phi$ . Thus, the field expansion with respect to the Rindler modes implicates that

$$\phi_k^M = \int_{-\infty}^{\infty} dk' A^R(k, k') \phi_{k'}^R + \int_{-\infty}^{\infty} dk' A^L(k, k') \phi_{k'}^L. \quad (6.174)$$

For  $\tau = 0$ , the coefficients  $A^R(k, k')$  and  $A^L(k, k')$  are

$$\begin{aligned} A^R(k, k') &= \frac{1}{2\pi} \int_{-\infty}^{\infty} dx e^{-ikx} e^{ik'\xi_R(x)} \theta(x) = -\frac{i}{2\pi a} \Gamma\left(1 + \frac{ik'}{a}\right) \left| \frac{k}{a} \right|^{-1 - \frac{k'}{a}} \left( \theta(k) e^{\frac{\pi k'}{2a}} - \theta(-k) e^{-\frac{\pi k'}{2a}} \right), \\ A^L(k, k') &= \frac{1}{2\pi} \int_{-\infty}^{\infty} dx e^{-ikx} e^{ik'\xi_L(x)} \theta(-x) = -\frac{i}{2\pi a} \Gamma\left(1 + \frac{ik'}{a}\right) \left| \frac{k}{a} \right|^{-1 - \frac{k'}{a}} \left( \theta(-k) e^{\frac{\pi k'}{2a}} - \theta(k) e^{-\frac{\pi k'}{2a}} \right), \end{aligned} \quad (6.175)$$

therefore satisfying  $A^L(k, k') = A^R(-k, k')$  and  $A^L(-k, k') = A^R(k, k')$ . The Minkowski vacuum is, then,

$$(\Psi^M)_0[\phi_k^R, \phi_k^{R*}, 0] = N_0 \exp\left(-\frac{I}{2}\right), \quad (6.176)$$

with the integral  $I$  given by

$$I = \int_{-\infty}^{\infty} dk |k| |\phi_k^M|^2 = \int_{-\infty}^{\infty} dk |k| \sum_{i,j=R,L} \int_{-\infty}^{\infty} \int_{-\infty}^{\infty} dk' dk'' \mathcal{I}^{ij}(k, k', k'') \phi_{k'}^i \phi_{k''}^j. \quad (6.177)$$

The coefficients  $\mathcal{I}^{ij}(k, k', k'')$  are identified as

$$\begin{aligned}\mathcal{I}^{ij}(k, k', k'') &\equiv A^i(k, k')A^j(-k, k'') \\ &= \frac{1}{4\pi^2 a^2} \Gamma\left(1 + \frac{ik'}{a}\right) \Gamma\left(1 + \frac{ik''}{a}\right) \left|\frac{k}{a}\right|^{-2 - \frac{i}{a}(k'+k'')} M^{ij}(k, k', k''),\end{aligned}\quad (6.178)$$

with the  $M^{ij}(k, k', k'')$  elements such that

$$\begin{aligned}M^{RR}(k, k', k'') &= \theta(k)e^{\frac{\pi}{2a}(k'-k'')} + \theta(-k)e^{-\frac{\pi}{2a}(k'-k'')}, \\ M^{RL}(k, k', k'') &= -\theta(k)e^{\frac{\pi}{2a}(k'+k'')} - \theta(-k)e^{-\frac{\pi}{2a}(k'+k'')}, \\ M^{LR}(k, k', k'') &= -\theta(k)e^{-\frac{\pi}{2a}(k'+k'')} - \theta(-k)e^{\frac{\pi}{2a}(k'+k'')}, \\ M^{LL}(k, k', k'') &= \theta(k)e^{-\frac{\pi}{2a}(k'-k'')} + \theta(-k)e^{\frac{\pi}{2a}(k'-k'')}.\end{aligned}\quad (6.179)$$

As we did in the last section, it is convenient to solve the integrals in  $k$  first. Hence, it is interesting to rearrange equation (6.177) in the following form

$$I = \sum_{i,j=R,L} \int_{-\infty}^{\infty} \int_{-\infty}^{\infty} dk' dk'' \Gamma\left(1 + \frac{ik'}{a}\right) \Gamma\left(1 + \frac{ik''}{a}\right) \phi_{k'}^i \phi_{k''}^j \times J^{ij}(k', k''),\quad (6.180)$$

with

$$J^{ij}(k', k'') = \frac{1}{4\pi^2 a^2} \int_{-\infty}^{\infty} dk |k| \left|\frac{k}{a}\right|^{-2 - \frac{i}{a}(k'+k'')} M^{ij}(k, k', k'').\quad (6.181)$$

Using the expressions for the  $M^{ij}$  in equation (6.179), we can reformulated these integrals in terms of delta functions in such manner that

$$\begin{aligned}J^{RR} = J^{LL} &= \frac{a}{\pi} \left(\frac{1}{a}\right)^{-\frac{i}{a}(k'+k'')} \cosh\left[\frac{\pi}{2a}(k' - k'')\right] \delta(k' + k''), \\ J^{RL} = J^{LR} &= -\frac{a}{\pi} \left(\frac{1}{a}\right)^{-\frac{i}{a}(k'+k'')} \cosh\left[\frac{\pi}{2a}(k' + k'')\right] \delta(k' + k'').\end{aligned}\quad (6.182)$$

Then, using this result and the same properties concerning the gamma functions we used in the single-wedge problem, we finally obtain

$$I = \int_{-\infty}^{\infty} dk' \left[ k' \coth\left(\frac{\pi k'}{a}\right) \left(|\phi_{k'}^R|^2 + |\phi_{k'}^L|^2\right) - k' \operatorname{csch}\left(\frac{\pi k'}{a}\right) \left(\phi_{k'}^R \phi_{k'}^{L*} + \phi_{k'}^L \phi_{k'}^{R*}\right) \right].\quad (6.183)$$

As a result, the Minkowski vacuum (6.176) in the hypersurface  $t = \tau = 0$  admits the

following expression in terms of Rindler variables:

$$(\Psi^M)_0 = N_0 \exp \left\{ -\frac{1}{2} \int_{-\infty}^{\infty} \left[ -k \coth \left( \frac{\pi k}{a} \right) \left( |\phi_k^R|^2 + |\phi_k^L|^2 \right) + k \operatorname{csch} \left( \frac{\pi k}{a} \right) \left( \phi_k^R \phi_k^{L*} + \phi_k^L \phi_k^{R*} \right) \right] \right\}. \quad (6.184)$$

Therefore, in addition to the individual contributions of each wedge given by the terms  $|\phi_k^R|^2$  and  $|\phi_k^L|^2$  inside the exponential, there are also mixed terms involving  $\phi_k^R \phi_k^{L*}$  and  $\phi_k^L \phi_k^{R*}$ , indicating a non-trivial correlation between  $\phi_k^R$  and  $\phi_k^L$ . In other words, the vacuum is not composed simply by the sum of the contributions from each individual wedge, but it also contains a kind of mixture concerning the field modes from both sides. In fact, is precisely this second contribution the responsible for the entanglement between the right and left wedges observed in [198]. In the regime of low accelerations,  $\coth(\pi k/a) \approx 1$  and  $\operatorname{csch}(\pi k/a) \approx 0$ , implying that, in this limit, this wave functional is the product of the individual ground states corresponding to the right and left sides and does not exhibit entanglement properties. This occurs because, as  $a$  approaches to zero, the Minkowski and Rindler spaces become equivalent.

Notably, the wave functional (6.184) aligns with the normal mode decomposition given in (6.61). So, it can be decomposed as a product of the form  $(\Psi^M)_0 = \prod_{k>0} (\Psi_k^M)_0$ , where is possible to identify that

$$(\Psi_k^M)_0[\phi_k^R, \phi_k^{R*}, \phi_k^L, \phi_k^{L*}, 0] = N_k \exp \left[ -k \coth \left( \frac{\pi k}{a} \right) \left( |\phi_k^R|^2 + |\phi_k^L|^2 \right) + k \operatorname{csch} \left( \frac{\pi k}{a} \right) \left( \phi_k^R \phi_k^{L*} + \phi_k^L \phi_k^{R*} \right) \right]. \quad (6.185)$$

As such, a suitable ansatz for the ground state wave functional at a generic time  $\tau$  is

$$(\Psi_k^M)_0 = \mathcal{N}_k \exp \left( -k F_k(\tau) \left( |\phi_k^R|^2 + |\phi_k^L|^2 \right) + k G_k(\tau) \left( \phi_k^{R*} \phi_k^L + \phi_k^R \phi_k^{L*} \right) + \Theta_k(\tau) \right), \quad (6.186)$$

with  $F_k(\tau)$ ,  $G_k(\tau)$ , and  $\Theta_k(\tau)$  coefficients to be determined. The Rindler Hamiltonian in this case is the sum of the Hamiltonians in each wedge (see equation (6.77)), that is,

$$H^R = \int_0^\infty dk \left( -\frac{\partial^2}{\partial \phi_k^R \partial \phi_k^{R*}} + k^2 |\phi_k^R|^2 \right) + \int_0^\infty dk \left( -\frac{\partial^2}{\partial \phi_k^L \partial \phi_k^{L*}} + k^2 |\phi_k^L|^2 \right). \quad (6.187)$$

Since each  $(\Psi_k^M)_0$  satisfies an independent Schrödinger equation, we obtain that

$$i \frac{\partial (\Psi_k^M)_0}{\partial \tau} = \left( -\frac{\partial^2}{\partial \phi_k^{R*} \partial \phi_k^R} - \frac{\partial^2}{\partial \phi_k^{L*} \partial \phi_k^L} + k^2 \left( |\phi_k^R|^2 + |\phi_k^L|^2 \right) \right) (\Psi_k^M)_0, \quad (6.188)$$

which leads to the set of differential equations

$$\frac{i}{k} \frac{\partial F_k}{\partial \tau} - (F_k^2 + G_k^2) + 1 = 0, \quad \frac{i}{k} \frac{\partial G_k}{\partial \tau} - 2F_k G_k = 0, \quad \frac{i}{k} \frac{\partial \Omega_k}{\partial \tau} - 2F_k = 0, \quad (6.189)$$

with  $F_k(0) = \coth\left(\frac{\pi k}{a}\right)$ ,  $G_k(0) = \operatorname{csch}\left(\frac{\pi k}{a}\right)$ , and  $\Omega_k(0) = 0$  as the initial conditions. The solution is,

$$F_k(\tau) = \coth\left(\frac{\pi k}{a} + 2ik\tau\right), \quad G_k(\tau) = \operatorname{csch}\left(\frac{\pi k}{a} + 2ik\tau\right), \quad (6.190)$$

and

$$\Theta_k(\tau) = -\ln \left[ \sinh\left(\frac{\pi k}{a} + 2ik\tau\right) \right], \quad (6.191)$$

where we absorb the integration constant coming from  $\Theta_k$  in the normalization factor. Note the similarity with the solution for the right-wedge case (equations (6.96) and (6.97)). The value of  $\mathcal{N}_k$  is determined through the requirement that  $\int |(\Psi_k^M)_0|^2 d\phi_k^R d\phi_k^{R*} d\phi_k^L d\phi_k^{L*} = 1$ , implying that

$$\mathcal{N}_k(\tau) = \frac{k}{\pi} \sinh\left(\frac{\pi k}{a}\right). \quad (6.192)$$

In what follows, we will give the de Broglie-Bohm's approach concerning the wave functional (6.185).

## 6.4.2 Bohmian interpretation for the two wedges

Because of the non-trivial correlation between the field modes in both wedges observed in the wave functional, the field on the right side depends on the field on the left side, even without an interaction between them. This mutual dependence is evident when we look at the dBB guidance equations. So, turning to the Bohmian theory and expressing the wave functional in the polar form  $(\Psi_k^M)_0 = R_k e^{iS_k}$  reveals that

$$\begin{aligned} R_k &= \mathcal{N}_k \exp\left(-k\Re[F_k(\tau)] (|\phi_k^R|^2 + |\phi_k^L|^2) + k\Re[G_k(\tau)] (\phi_k^R \phi_k^{L*} + \phi_k^L \phi_k^{R*}) + \Re[\Theta_k(\tau)]\right) \\ S_k &= -k\Im[F_k(\tau)] (|\phi_k^R|^2 + |\phi_k^L|^2) + k\Im[G_k(\tau)] (\phi_k^R \phi_k^{L*} + \phi_k^L \phi_k^{R*}) + \Im[\Theta_k(\tau)], \end{aligned} \quad (6.193)$$

with the real and imaginary parts of  $F_k(\tau)$  and  $G_k(\tau)$  being

$$\Re[F_k(\tau)] = \frac{\sinh\left(\frac{2\pi k}{a}\right)}{\cosh\left(\frac{2\pi k}{a}\right) - \cos(4k\tau)}, \quad \Im[F_k(\tau)] = \frac{-\sin(4k\tau)}{\cosh\left(\frac{2\pi k}{a}\right) - \cos(4k\tau)}, \quad (6.194)$$

$$\Re[G_k(\tau)] = \frac{2\sinh\left(\frac{\pi k}{a}\right)\cos(2k\tau)}{\cosh\left(\frac{2\pi k}{a}\right) - \cos(4k\tau)}, \quad \Im[G_k(\tau)] = \frac{-2\cosh\left(\frac{\pi k}{a}\right)\sin(2k\tau)}{\cosh\left(\frac{2\pi k}{a}\right) - \cos(4k\tau)}, \quad (6.195)$$

whereas for  $\Theta_k(\tau)$ ,

$$\Re[\Theta_k(\tau)] = -\frac{1}{2}\ln\left[\cosh^2\left(\frac{\pi k}{a}\right) - \cos^2(2k\tau)\right], \quad \Im[\Theta_k(\tau)] = -\tan^{-1}\left(\coth\left(\frac{\pi k}{a}\right)\tan(2k\tau)\right). \quad (6.196)$$

Inserting the polar decomposition of  $(\Psi_k^M)_0$  into Schrödinger equation (6.188) leads to the usual dBB equations,

$$\frac{\partial S_k}{\partial \tau} + \sum_{i=R,L} \left[ \left( \frac{\partial S_k}{\partial \phi_k^{i*}} \frac{\partial S_k}{\partial \phi_k^i} \right) + k^2 |\phi_k^i|^2 \right] - \frac{1}{R_k} \sum_{i=R,L} \left( \frac{\partial^2 R_k}{\partial \phi_k^i \partial \phi_k^{i*}} \right) = 0 \quad (6.197)$$

and

$$\frac{\partial R_k^2}{\partial \tau} + \sum_{i=R,L} \left[ \frac{\partial}{\partial \phi_k^i} \left( R_k^2 \frac{\partial S_k}{\partial \phi_k^{i*}} \right) + \frac{\partial}{\partial \phi_k^{i*}} \left( R_k^2 \frac{\partial S_k}{\partial \phi_k^i} \right) \right] = 0, \quad (6.198)$$

which consist of the Hamilton-Jacobi and continuity equations. While  $R_k^2$  is interpreted as the field probability distribution,  $\frac{\partial S_k}{\partial \phi_k^R}$  and  $\frac{\partial S_k}{\partial \phi_k^L}$  correspond to the velocity fields, yielding the dBB guidance equations

$$\frac{\partial \phi_k^R}{\partial \tau} = \frac{\partial S_k}{\partial \phi_k^{R*}} = -k\Im[F_k(\tau)]\phi_k^R + k\Im[G_k(\tau)]\phi_k^L, \quad (6.199)$$

$$\frac{\partial \phi_k^L}{\partial \tau} = \frac{\partial S_k}{\partial \phi_k^{L*}} = -k\Im[F_k(\tau)]\phi_k^L + k\Im[G_k(\tau)]\phi_k^R. \quad (6.200)$$

Hence, according to these, a change in  $\phi_k^R$  has an immediate effect on  $\phi_k^L$  and vice-versa, indicating a non-local connection between them, which, in this case, is not an exclusive feature of Bohmian interpretation but rather a characteristic of the two-wedge problem. In this regard, Bohmian Mechanics effectively addresses this issue due to its non-local nature. This is further supported by the effective Klein-Gordon equations for the Bohmian fields,

since

$$\frac{\partial^2 \phi_k^R}{\partial \tau^2} + k^2 \phi_k^R = k^2 (\Re^2[f_k] + \Re^2[g_k]) \phi_k^R - 2k^2 \Re[f_k] \Re[g_k] \phi_k^L \quad (6.201)$$

$$\frac{\partial^2 \phi_k^L}{\partial \tau^2} + k^2 \phi_k^L = k^2 (\Re^2[f_k] + \Re^2[g_k]) \phi_k^L - 2k^2 \Re[f_k] \Re[g_k] \phi_k^R. \quad (6.202)$$

As in the previous section, we can identify the total energy and its components from the Hamilton-Jacobi equation (6.197):

$$\begin{aligned} E_k(\tau) &\equiv -\frac{1}{2} \left( \frac{\partial S_k}{\partial \tau} \right), & K_k(\tau) &\equiv \frac{1}{2} \left[ \left( \frac{\partial S_k}{\partial \phi_k^{R*}} \frac{\partial S_k}{\partial \phi_k^R} \right) + \left( \frac{\partial S_k}{\partial \phi_k^{L*}} \frac{\partial S_k}{\partial \phi_k^L} \right) \right], \\ V_k(\tau) &\equiv \frac{k^2}{2} (|\phi_k^R|^2 + |\phi_k^L|^2), & Q_k(\tau) &\equiv -\frac{1}{2R_k} \left( \frac{\partial^2 R_k}{\partial \phi_k^R \partial \phi_k^{R*}} - \frac{\partial^2 R_k}{\partial \phi_k^L \partial \phi_k^{L*}} \right), \end{aligned} \quad (6.203)$$

with each part being the sum of the contributions coming from the right and left wedges. From equation (6.193), we obtain the corresponding expressions in terms of  $F_k(\tau)$ ,  $G_k(\tau)$  and  $\Theta_k(\tau)$ , which are

$$\begin{aligned} E_k(\tau) &= \frac{1}{2} \left[ k \frac{\partial \Im[F_k]}{\partial \tau} (|\phi_k^R|^2 + |\phi_k^L|^2) - k \frac{\partial \Im[G_k]}{\partial \tau} (\phi_k^R \phi_k^{L*} + \phi_k^L \phi_k^{R*}) - \frac{\partial \Im[\Theta_k]}{\partial \tau} \right], \\ K_k(\tau) &= \frac{1}{2} \left[ k^2 (\Im^2[F_k] + \Im^2[G_k]) (|\phi_k^R|^2 + |\phi_k^L|^2) - 2k^2 \Im[F_k] \Im[G_k] (\phi_k^R \phi_k^{L*} + \phi_k^L \phi_k^{R*}) \right], \\ V_k(\tau) &= \frac{1}{2} (k^2 |\phi_k^R|^2 + k^2 |\phi_k^L|^2), \\ Q_k(\tau) &= -\frac{1}{2} \left[ k^2 (\Re^2[F_k] + \Re^2[G_k]) (|\phi_k^R|^2 + |\phi_k^L|^2) - 2k^2 \Re[F_k] \Re[G_k] (\phi_k^R \phi_k^{L*} + \phi_k^L \phi_k^{R*}) - 2k \Re[F_k] \right]. \end{aligned} \quad (6.204)$$

Despite the rather complicated form due to the cross terms present in the last equalities and its non-local effect in dBB guidance equations, these expressions simplify considerably when we introduce the field variables

$$\chi_{1,k} = \frac{\phi_k^R + \phi_k^L}{\sqrt{2}}, \quad \chi_{2,k} = \frac{\phi_k^R - \phi_k^L}{\sqrt{2}}. \quad (6.205)$$

In fact, these variables have the capacity to decouple the system into two independent states, so that the wave functional can be written as the product

$$\begin{aligned} (\Psi_k^M)_0 &= \frac{k}{\pi} e^{\Theta_k(\tau)} \sinh \left( \frac{\pi k}{a} \right) e^{-kH_{1,k}(\tau) |\chi_{1,k}|^2} e^{-kH_{2,k}(\tau) |\chi_{2,k}|^2} \\ &\equiv \Psi_{1,k}[\chi_{1,k}, \chi_{1,k}^*, \tau] \otimes \Psi_{2,k}[\chi_{2,k}, \chi_{2,k}^*, \tau], \end{aligned} \quad (6.206)$$

with

$$H_{1,k} \equiv F_k - G_k = \tanh\left(\frac{\pi k}{2a} + ik\tau\right), \quad H_{2,k} \equiv F_k + G_k = \coth\left(\frac{\pi k}{2a} + ik\tau\right), \quad (6.207)$$

in such a wise that

$$\Re[H_{1,k}(\tau)] = \frac{\sinh\left(\frac{\pi k}{a}\right)}{\cosh\left(\frac{\pi k}{a}\right) + \cos(2k\tau)}, \quad \Im[H_{1,k}(\tau)] = \frac{\sin(2k\tau)}{\cosh\left(\frac{\pi k}{a}\right) + \cos(2k\tau)}, \quad (6.208)$$

$$\Re[H_{2,k}(\tau)] = \frac{\sinh\left(\frac{\pi k}{a}\right)}{\cosh\left(\frac{\pi k}{a}\right) - \cos(2k\tau)}, \quad \Im[H_{2,k}(\tau)] = -\frac{\sin(2k\tau)}{\cosh\left(\frac{\pi k}{a}\right) - \cos(2k\tau)}. \quad (6.209)$$

So,  $\Psi_{1,k}$  and  $\Psi_{2,k}$  represent two separated states, with  $\Psi_{2,k}$  corresponding to a squeezed state [199], characterized by a squeezing parameter  $r_k$  such that  $\tanh r_k = e^{-\pi k/a}$ , and a squeezing angle  $\alpha_k = -k\tau$ . Similarly,  $\Psi_{1,k}$  can be viewed in the same manner but with the squeezing angle rotated by  $\pi/2$ . With this parameterization, we obtain that

$$\Psi_{A,k}[\chi_{A,k}] \propto \exp\left(-k \frac{1 + e^{2i\alpha_k} \tanh r_k}{1 - e^{2i\alpha_k} \tanh r_k} |\chi_{A,k}|^2\right), \quad (6.210)$$

with  $A = 1, 2$ . Note that  $H_{2,k}$  has the same expression as  $f_k(\tau)$  in equation (6.96). Then,  $\Psi_{2,k}$  can be understood in the same manner as the right-wedge wave functional, but with  $\phi_k^R$  substituted for  $\chi_{2,k}$ . Analogously,  $\Psi_{1,k}$  corresponds to the left-wedge version of the ground state (6.93). Therefore, the decomposition (6.206) can be interpreted as the product of two decoupled Minkowski wave functionals in Rindler-like variables.

In terms of  $\chi_{1,k}$  and  $\chi_{2,k}$ , the energy components of the Hamilton-Jacobi equation and the total energy itself are simplified to

$$\begin{aligned} E_k(\tau) &= \frac{1}{2} \left[ k \frac{\partial \Im[H_{1,k}]}{\partial \tau} |\chi_{1,k}|^2 + k \frac{\partial \Im[H_{2,k}]}{\partial \tau} |\chi_{2,k}|^2 - \frac{\partial \Im[\Theta_k]}{\partial \tau} \right], \\ K_k(\tau) &= \frac{1}{2} \left[ k^2 \Im^2[H_{1,k}(\tau)] |\chi_{1,k}|^2 + k^2 \Im^2[H_{2,k}(\tau)] |\chi_{2,k}|^2 \right], \\ V_k(\tau) &= \frac{1}{2} \left[ k^2 |\chi_{1,k}|^2 + k^2 |\chi_{2,k}|^2 \right], \\ Q_k(\tau) &= \frac{1}{2} \left[ k \left( \Re[H_{1,k}(\tau)] + \Re[H_{2,k}(\tau)] \right) - k^2 \left( \Re^2[H_{1,k}(\tau)] |\chi_{1,k}|^2 + \Re^2[H_{2,k}(\tau)] |\chi_{2,k}|^2 \right) \right], \end{aligned} \quad (6.211)$$

with no presence of crossed terms. Furthermore, the guidance equations are decoupled

into two independent equations

$$\frac{\partial \chi_{1,k}}{\partial \tau} = -k \Im[H_{1,k}(\tau)] \chi_{1,k}, \quad \frac{\partial \chi_{2,k}}{\partial \tau} = -k \Im[H_{2,k}(\tau)] \chi_{2,k}, \quad (6.212)$$

a property that also extends to the effective Klein-Gordon equations,

$$\frac{\partial^2 \chi_{1,k}}{\partial \tau^2} + k^2 \chi_{1,k} = k^2 \Re^2[H_{1,k}(\tau)] \chi_{1,k}, \quad (6.213)$$

$$\frac{\partial^2 \chi_{2,k}}{\partial \tau^2} + k^2 \chi_{2,k} = k^2 \Re^2[H_{2,k}(\tau)] \chi_{2,k}, \quad (6.214)$$

which, as before, are Klein-Gordon-type equations supplemented by a linear source of quantum origin. In the forthcoming subsections, we will proceed to derive Bohmian averages, investigate the limits of low and high accelerations, and subsequently compute the field trajectories.

### 6.4.3 Mean values for the extended geometry

The Bohmian averages related to the field trajectories considering the two wedges are calculated as follows:

$$\langle \mathcal{O}(\tau) \rangle_{dBB} = \int \mathcal{D}\phi_k \left| \Psi_k[\phi_k^R, \phi_k^{R*}, \phi_k^L, \phi_k^{L*}, \tau] \right|^2 \mathcal{O}(\phi_k^R, \phi_k^{R*}, \phi_k^L, \phi_k^{L*}, \tau), \quad (6.215)$$

with  $\mathcal{D}\phi_k = d\phi_k^R d\phi_k^{R*} d\phi_k^L d\phi_k^{L*}$  the integration measure. However, due the complexity of the wave functional (6.186), it is more straightforward to compute the mean values in terms of  $\chi_{1,k}$  and  $\chi_{2,k}$ , which provides

$$\langle \mathcal{O}(\tau) \rangle_{dBB} = \int D\chi_k \left| \Psi_k[\chi_{1,k}, \chi_{1,k}^*, \chi_{2,k}, \chi_{2,k}^*, \tau] \right|^2 \mathcal{O}(\chi_{1,k}, \chi_{1,k}^*, \chi_{2,k}, \chi_{2,k}^*, \tau), \quad (6.216)$$

with  $D\chi_k = d\chi_{1,k} d\chi_{1,k}^* d\chi_{2,k} d\chi_{2,k}^*$ .

In those variables,

$$|\Psi_k|^2 = \frac{k^2}{\pi^2} \Re[H_{1,k}(\tau)] \Re[H_{2,k}(\tau)] e^{-2k \Re[H_{1,k}(\tau)] |\chi_{1,k}|^2} e^{-2k \Re[H_{2,k}(\tau)] |\chi_{2,k}|^2}. \quad (6.217)$$

So, according to the relations (6.211) and the previous form of the probability density, the average values of the kinetic energy  $K_k$ , the classical potential  $V_k$ , and the quantum

potential  $Q_k$  are

$$\langle K_k \rangle_{dBB} = \frac{k}{4} \left( \frac{\Im^2[H_{1,k}(\tau)]}{\Re[H_{1,k}]} + \frac{\Im^2[H_{2,k}(\tau)]}{\Re[H_{2,k}]} \right) = \frac{k \coth\left(\frac{\pi k}{a}\right) \sin^2(2k\tau)}{\cosh\left(\frac{2\pi k}{a}\right) - \cos(4k\tau)}, \quad (6.218)$$

$$\langle V_k \rangle_{dBB} = \frac{k}{4} \left( \frac{1}{\Re[H_{1,k}(\tau)]} + \frac{1}{\Re[H_{2,k}(\tau)]} \right) = \frac{k}{2} \coth\left(\frac{\pi k}{a}\right), \quad (6.219)$$

$$\langle Q_k \rangle_{dBB} = \frac{k}{4} (\Re[H_{1,k}(\tau)] + \Re[H_{2,k}(\tau)]) = \frac{k \sinh\left(\frac{2\pi k}{a}\right)}{2 \left[ \cosh\left(\frac{2\pi k}{a}\right) - \cos(4k\tau) \right]}, \quad (6.220)$$

while for the total energy, we have that

$$\langle E_k \rangle_{dBB} = k \coth\left(\frac{\pi k}{a}\right) = 2k \left( \frac{1}{2} + \frac{1}{e^{\frac{2\pi}{a}k} - 1} \right). \quad (6.221)$$

which is twice the value obtained for the right-wedge case. This result is consistent with the fact that each wedge should contribute with the same amount of energy, as we can see by equation (6.187). Note that, in this case, the average of the classical potential is time-independent, being half the value of the total mean energy. In Figure (6.6), we examine the behavior of the Bohmian averages for different values of the acceleration parameter. For  $\tau = 0$ , we have an equivalence between quantum and classical contributions, since  $\langle Q_k \rangle_{dBB} = \langle V_k \rangle_{dBB}$ . Conversely, for  $\tau = \pi/4$ , this equality is valid only for low accelerations, with  $\langle Q_k \rangle_{dBB}$  dropping to zero as  $a$  increases.

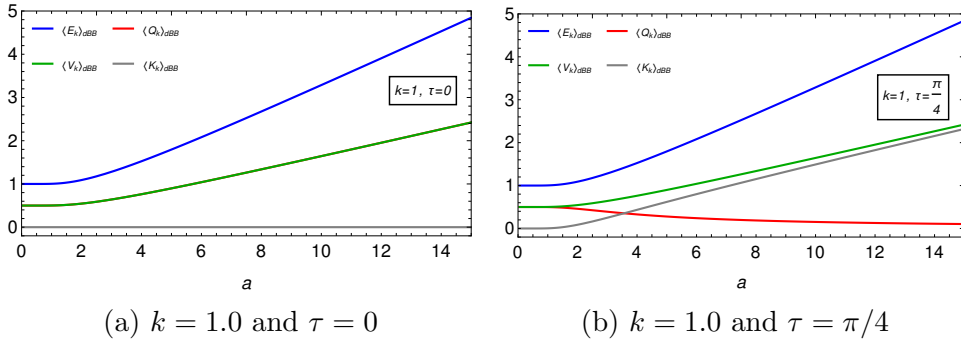


Figure 6.6: The mean values as functions of the parameter  $a$  for  $\tau = 0$  and  $\tau = \pi/4$ . Note that for  $\tau = 0$ ,  $\langle Q_k \rangle_{dBB} = \langle V_k \rangle_{dBB}$ .

As we did in section (6), it is possible to determine the mean number of Rindler particles in the Minkowski vacuum through the Hamiltonian operator  $\hat{H}_k = (2\hat{n}_k + 1)k$ , since we have two massless non-interacting scalar fields. Thus,  $\langle n_k \rangle_{dBB} = (\frac{1}{k} \langle E_k \rangle_{dBB} - 1)/2$ , which implies that

$$\langle n_k \rangle_{dBB} = \frac{1}{e^{\frac{2\pi}{a}k} - 1}, \quad (6.222)$$

being precisely the Bose-Einstein distribution with Unruh temperature  $T = a/2\pi$ .

#### 6.4.4 Low and high acceleration regimes

##### Low acceleration limit:

Let us suppose a regime of low accelerations in such wise that  $\frac{\pi k}{a} \gg 1$ . In this limit, the following expansions for the wave functional coefficients are valid

$$\Re[H_{1,k}(\tau)] \approx \Re[H_{2,k}(\tau)] \approx 1, \quad \Im[H_{1,k}(\tau)] \approx \Im[H_{2,k}(\tau)] \approx 0, \quad (6.223)$$

$$\Re[\Theta_k(\tau)] \approx -\frac{k}{2T}, \quad \Im[\Theta_k(\tau)] \approx -2k\tau,$$

with  $(\Psi_k^M)_0$  becoming

$$\begin{aligned} (\Psi_k^M)_0[\chi_{1,k}, \chi_{2,k}, \tau] &\approx \frac{k}{\pi} e^{-k|\chi_{1,k}|^2 - k|\chi_{2,k}|^2 - 2ik\tau} \\ &\approx \left( \sqrt{\frac{k}{\pi}} e^{-k|\phi_k^R|^2 - ik\tau} \right) \left( \sqrt{\frac{k}{\pi}} e^{-k|\phi_k^L|^2 - ik\tau} \right). \end{aligned} \quad (6.224)$$

This is precisely the product of the Rindler vacuums in equation (6.79) for the right and left wedges, indicating that in this limit the vacuum defined in the entire Minkowski space and in the extended Rindler geometry are equivalent.

The energy components of the Hamilton-Jacobi equation are approximately equal to those associated with the ground state of two non-interacting fields in Minkowski space, that is,  $E_k = k$ ,  $K_k \approx 0$ , and  $Q_k = k - V_k$ . Moreover, the guidance equations  $\partial_\tau \chi_{k,1} \approx 0$  and  $\partial_\tau \chi_{k,2} \approx 0$  lead to static solutions in terms of the  $\chi$  variables,  $\chi_{k,1}(\tau) = \chi_{k,1}(0)$  and  $\chi_{k,2}(\tau) = \chi_{k,2}(0)$ , characteristic also present in the original fields  $\phi_k^R(\tau) = \phi_k^R(0)$  and  $\phi_k^L(\tau) = \phi_k^L(0)$ , reflecting the equivalence between Minkowski and Rindler vacuums in this limit. Regarding the mean values we have that

$$\langle K_k \rangle_{dBB} \approx 2k \sin^2(2k\tau) e^{-k/T} \approx 0, \quad (6.225)$$

$$\langle V_k \rangle_{dBB} \approx \frac{k}{2} + k e^{-k/T} \approx \frac{k}{2}, \quad (6.226)$$

$$\langle Q_k \rangle_{dBB} \approx \frac{k}{2} + k \cos(4k\tau) e^{-k/T} \approx \frac{k}{2}, \quad (6.227)$$

$$\langle E_k \rangle_{dBB} \approx k. \quad (6.228)$$

Once more, we recover the familiar de Broglie-Bohm representation of the Minkowski vacuum state, with the field energy equally distributed between the classical and quantum potentials, while its kinetic energy remains negligible.

**High acceleration limit:**

Now, let us consider the expansions for the wave functional coefficients in the limit when  $\frac{\pi k}{a} \ll 1$ , that is to say, the regime of high accelerations. As before, we have two distinct scenarios for this situation:

**i)  $\tau \neq n\pi/(2k)$ , with  $n$  a an integer (classical dominance)**

This first case is characterized by a classical dominance, where

$$\begin{aligned}\Re[H_{1,k}(\tau)] &\approx \frac{k}{4T \cos^2(k\tau)}, & \Im[H_{1,k}(\tau)] &\approx \tan(k\tau), \\ \Re[H_{2,k}(\tau)] &\approx \frac{k}{4T \sin^2(k\tau)}, & \Im[H_{2,k}(\tau)] &\approx -\cot(k\tau), \\ \Re[\Omega_k(\tau)] &\approx \ln \sqrt{2} - \frac{1}{2} \ln(1 - \cos(4k\tau)), & \Im[\Omega_k(\tau)] &\approx -\frac{\pi}{2} \text{sign}(\tan(2k\tau)),\end{aligned}\tag{6.229}$$

with the Minkowski wave functional being

$$\begin{aligned}(\Psi_k^M)_0[\chi_{1,k}, \chi_{1,k}^*, \chi_{2,k}, \chi_{2,k}^*, \tau] &\approx \frac{k^2}{2\pi T} \frac{1}{|\sin(2k\tau)|} \exp \left\{ -\frac{k^2}{4T \cos^2(k\tau)} |\chi_{1,k}|^2 - \frac{k^2}{4T \sin^2(k\tau)} |\chi_{2,k}|^2 \right\} \times \\ &\exp \left\{ i \left[ -k \tan(k\tau) |\chi_{1,k}|^2 + k \cot(k\tau) |\chi_{2,k}|^2 - \frac{\pi}{2} \text{sign}(\tan(k\tau)) \right] \right\}.\end{aligned}\tag{6.230}$$

As a consequence, the mean values are such that

$$\langle K_k \rangle_{dBB} \approx T,\tag{6.231}$$

$$\langle V_k \rangle_{dBB} \approx T,\tag{6.232}$$

$$\langle Q_k \rangle_{dBB} \approx \frac{k^2}{4T \sin^2(2k\tau)} \approx 0,\tag{6.233}$$

$$\langle E_k \rangle_{dBB} \approx 2T.\tag{6.234}$$

In this regime, the classical components, the kinetic and classical potential energies, account for the entire total energy of  $2T$ , while we have a negligible contribution from the quantum potential.

**ii)  $\tau = n\pi/(2k)$ , with  $n$  a an integer (quantum transition)**

Similar to the right-wedge case, the classical components predominantly influence the average energy  $\langle E_k \rangle_{dBB}$  for most part of the time. Nevertheless, a significant shift occurs

in the vicinity of  $\tau = n\pi/(2k)$ . In this case, we have that

$$\begin{aligned}\Re[H_{1,k}(\tau)] &\approx \frac{k}{4T}, & \Im[H_{1,k}(\tau)] &\approx 0, \\ \Re[H_{2,k}(\tau)] &\approx \frac{4T}{k}, & \Im[H_{2,k}(\tau)] &\approx 0, \\ \Re[\Omega_k(\tau)] &\approx \ln\left(\frac{4T}{k}\right), & \Im[\Omega_k(\tau)] &\approx 0,\end{aligned}\tag{6.235}$$

implying in a wave functional of the form

$$(\Psi_k^M)_0[\chi_{1,k}, \chi_{1,k}^*, \chi_{2,k}, \chi_{2,k}^*, \tau] \approx \frac{k}{\pi} \exp\left\{-\frac{k^2}{4T}|\chi_{1,k}|^2 - 4T|\chi_{2,k}|^2\right\}.\tag{6.236}$$

Regarding the Bohmian averages we obtain

$$\langle K_k \rangle_{dBB} \approx 0,\tag{6.237}$$

$$\langle V_k \rangle_{dBB} \approx T,\tag{6.238}$$

$$\langle Q_k \rangle_{dBB} \approx T,\tag{6.239}$$

$$\langle E_k \rangle_{dBB} \approx 2T,\tag{6.240}$$

meaning that the energy now is shared between the classical and quantum potentials, with no contribution of the kinetic component.

As previously stated, the average of the classical potential remains constant over time and always contributes with half of the total mean energy. The remaining part is now furnished by the mean kinetic energy, marked by sudden transitions to the dominance of the mean quantum potential occurring periodically around  $\tau = n\pi/(2k)$ . Consequently, in the two-wedges case, the periodic spikes involve solely the mean kinetic and quantum potential energies, interchanging half of the total energy.

It is interesting to examine the behavior of the Bohmian averages in relation to  $\chi_{1,k}$  and  $\chi_{2,k}$  separately. Since the coefficient  $H_{2,k}$  that accompanies  $\chi_{2,k}$  is equal to  $f_k$  of the right-wedge case (equation (6.96)), the contributions of  $\chi_{2,k}$  to the total energy and its components exhibit the same patterns as previously discussed in the non-extended case. Hence, this mode is responsible for the abrupt spikes occurring at  $\tau = n\pi/k$  in the high temperature regime, marking the transitions from classical to quantum dominance. For the  $\chi_{1,k}$ , on the other hand, the coefficient  $H_{1,k}$  can be derived from  $H_{2,k}$  substituting the denominator  $\cosh\left(\frac{\pi k}{a}\right) - \cos(2k\tau)$  for  $\cosh\left(\frac{\pi k}{a}\right) + \cos(2k\tau)$  (as delineated in equations (6.208, 6.209)). Thus, the properties are similar but the jumps between classical and

quantum predominance attributable to  $\chi_{1,k}$  occur in the vicinity of  $\tau = \left(n + \frac{1}{2}\right) \frac{\pi}{k}$ .

In Figure 6.7 we plot two graphics of the average values  $\langle K_k \rangle_{dBB}$ ,  $\langle V_k \rangle_{dBB}$ , and  $\langle Q_k \rangle_{dBB}$ : the first corresponds to an intermediate acceleration ( $a = 1$ ), while the second relates to a high value of the acceleration parameter ( $a = 100$ ). We observe that  $\langle K_k \rangle_{dBB}$  and  $\langle Q_k \rangle_{dBB}$  exhibit opposite behaviors. When one reaches its maximum amplitude, the other have a minimum value, with both periodically interchanging their contribution to the total energy. For higher accelerations, abrupt transitions occur, as illustrated in the right plot. The difference between the two-wedges problem illustrated bellow and the single-wedge in Figure 6.3 lies precisely in the presence of spikes at  $\pi/2$  and  $3\pi/2$ , representing the moments when  $\tau = \left(n + \frac{1}{2}\right) \frac{\pi}{k}$ . As a result of the wave functional decomposition (6.206),  $(\Psi_k^M)_0 = \Psi_{1,k} \Psi_{2,k}$  can be regarded as the product of two single-wedge wave functionals for the field modes  $\chi_{1,k}$  and  $\chi_{2,k}$ , respectively, with the right-wedge represented by  $\Psi_{2,k}$  and the left-wedge by  $\Psi_{1,k}$ . In this sense, the additional spikes result from considering the left version of the single-wedge problem in the wave functional.

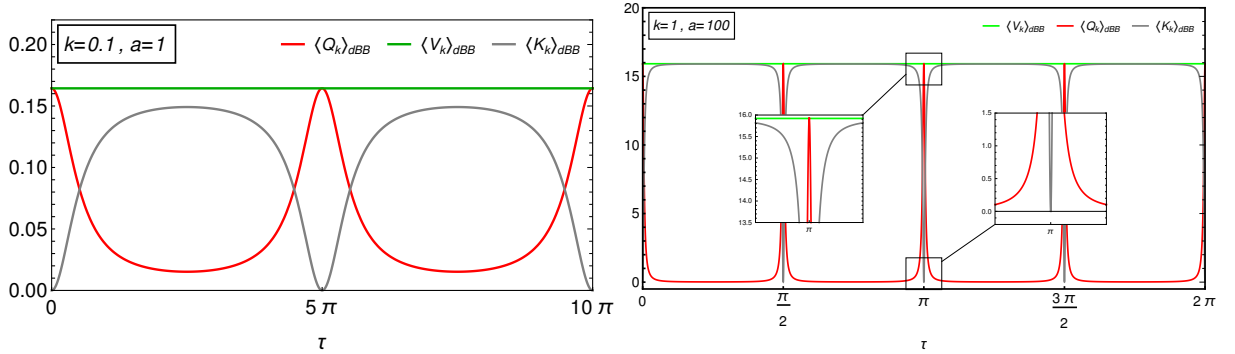


Figure 6.7: *Left*: Plot of the Bohmian averages for  $a = 1$  and  $k = 0.1$ . *Right*: The same plot, but considering  $a = 100$  and  $k = 1$ . Notice the sudden transitions in the neighborhood of  $\tau = n\pi/(2k)$ . The spikes at  $\tau = n\pi/k$  are a consequence of  $\chi_{2,k}$ , while the spikes at  $\tau = \left(n + \frac{1}{2}\right) \pi/k$  are attributed to  $\chi_{1,k}$ .

Similar to the right-wedge case, this effect is also evident from the effective Klein-Gordon equations for  $\chi_{1,k}$  and  $\chi_{2,k}$ , namely the expressions (6.213) and (6.214). Concerning the field  $\chi_{2,k}$ , we have the same relations presented in the previous section, hence yielding the same limits for  $\phi_k^R$  in (6.145) and (6.146). Concerning the mode  $\chi_{1,k}$ , however, the high temperature limit implies that

$$\frac{\partial^2 \chi_{1,k}}{\partial \tau^2} + k^2 \chi_{1,k} \approx \frac{k^4}{16T^2 \cos^2(k\tau)} \chi_{1,k} \approx 0; \quad \tau \neq \left(n + \frac{1}{2}\right) \frac{\pi}{k}, \quad (6.241)$$

indicating a negligible quantum force for  $\tau \neq \left(n + \frac{1}{2}\right) \frac{\pi}{k}$ , with the Bohmian field obeying a classical Klein-Gordon equation, while

$$\frac{\partial^2 \chi_{1,k}}{\partial \tau^2} + k^2 \chi_{1,k} \approx 16T^2 \chi_{1,k}; \quad \tau = \left(n + \frac{1}{2}\right) \frac{\pi}{k}, \quad (6.242)$$

revealing an effective mass that drives the field dynamics when  $\tau = (n + \frac{1}{2}) \frac{\pi}{k}$ . As a consequence, the abrupt changes at  $\tau = n\pi/(2k)$  are not an exclusive property of the Bohmian averages, but also occurring in the field equations of motion. In fact, this effect is observable even at the wave function level, suggesting that it may not be an exclusive attribute of the Bohmian interpretation. However, the significance of this effect becomes distinctly evident when viewed through this alternative perspective.

### 6.4.5 Extended field trajectories

Like the situation in the non-extended Rindler geometry, we encounter a particular field configuration, solution to dBB guidance equations (6.212), exhibiting analogous properties of the average values to those discussed in the previous subsection. Specifically, we obtain that

$$\chi_{1,k}(\tau) = \frac{D_{1,k}}{\sqrt{2k\Re[H_{1,k}(\tau)]}}, \quad \chi_{2,k}(\tau) = \frac{D_{2,k}}{\sqrt{2k\Re[H_{2,k}(\tau)]}}. \quad (6.243)$$

The trajectories probability density assumes a very simplified form, resembling a Gaussian shape:  $|\Psi_k|^2 \propto e^{-|D_{1,k}(a)|^2 - |D_{2,k}(a)|^2}$ . Just as discussed in section (6), field configurations with  $|D_{1,k}| = |D_{2,k}| = 1$  represent the exclusive scenario for Bohmian fields with time-independent energy, mirroring the average value outlined in equation (6.221). Moreover, for these specific Bohmian trajectories each component of the total energy precisely matches its respective average, meaning that  $K_k = \langle K_k \rangle_{dBB}$ ,  $V_k = \langle V_k \rangle_{dBB}$ , and  $Q_k = \langle Q_k \rangle_{dBB}$ . Hence, the asymptotic limits established in the previous subsection hold true for every individual Bohmian field characterized by the phases  $D_{1,k}(a) = \exp(i\theta_{1,k}(a))$ ,  $D_{2,k}(a) = \exp(i\theta_{2,k}(a))$ , including the periodic abrupt transitions from classical kinetic to quantum potential dominance discussed earlier.

The asymptotic tendencies of these specific Bohmian fields, without considering their phase, can be expressed as

$$\chi_{1,k} = \frac{1 + \cos(2k\tau)e^{-k/(2T)}}{\sqrt{2k}}, \quad \chi_{2,k} = \frac{1 - \cos(2k\tau)e^{-k/(2T)}}{\sqrt{2k}}, \quad T \ll 1. \quad (6.244)$$

$$\chi_{1,k} = \frac{\sqrt{2T}|\cos(k\tau)|}{k}, \quad \chi_{2,k} = \frac{\sqrt{2T}|\sin(k\tau)|}{k}, \quad T \gg 1. \quad (6.245)$$

In Figure 6.8, we show the field trajectories (6.243) for the original fields  $\phi_k^R$  and  $\phi_k^L$  as functions of the Rindler time, assuming  $\theta_{1,k} = \theta_{2,k} = 0$ . We investigate different situations ranging from low ( $a = 0.1$ ) to high ( $a = 100$ ) temperature regimes. For each case, we plot distinct trajectories considering different values of the parameter  $k$ , revealing a non-trivial behavior. We have static trajectories in the low-temperature domain, consistent with the predictions of Bohmian Mechanics. In contrast, at elevated temperatures, the field trajectories present intricate patterns. Therefore, with the increase of the temperature,

the field trajectories become more dynamic.

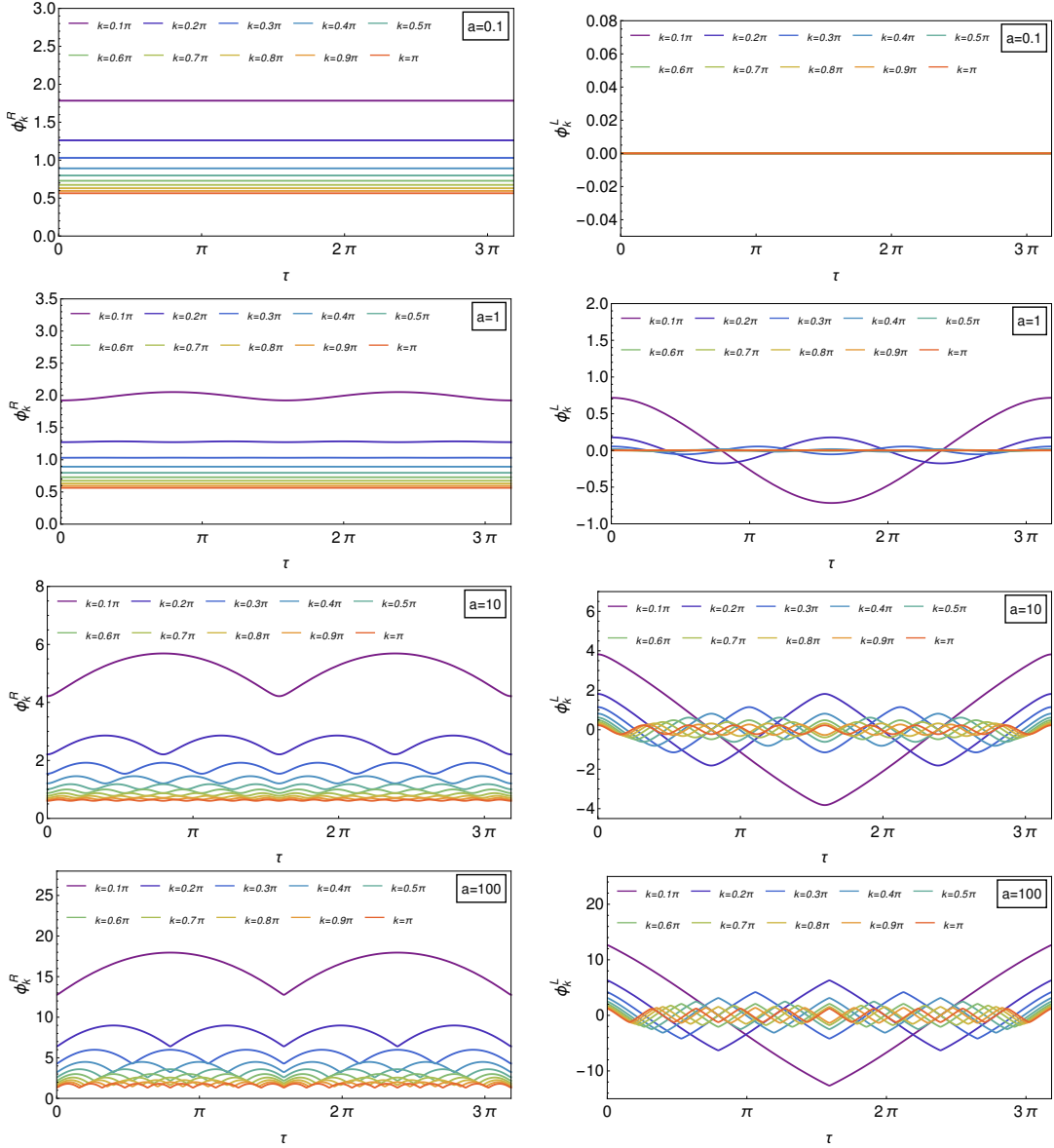


Figure 6.8: The field trajectories, plotted as functions of time, with  $\theta_{1,k} = \theta_{2,k} = 0$ . Each curve represents a distinct value of  $k$ . Within the low-temperature domain, both  $\phi_k^R$  and  $\phi_k^L$  exhibit static trajectories. As we approach the high-temperature conditions the field dynamics become considerably more complex.

#### 6.4.6 Power Spectrum for the complete manifold problem

Addressing the two-wedge scenario, our goal in this last part is to derive the power spectrum for the right and left modes. In order to consider the correlations of  $\phi_k^R$  and  $\phi_k^L$  with themselves, besides the crossed correlations regarding the right and left sides as

well, we define

$$(P^{ij})_k(\tau) = \int_{-\infty}^{\infty} d\xi e^{-ik\xi} \langle \phi^i(\xi) \phi^j(0) \rangle_{dBB}, \quad (6.246)$$

with  $\phi^i$  representing the inverse Fourier transform of  $\phi_k^i$ , where  $i, j = R, L$ . Additionally, in terms of the field variables  $\chi_{1,k}$  and  $\chi_{2,k}$ , we have that

$$(P_{AB})_k(\tau) = \int_{-\infty}^{\infty} d\xi e^{-ik\xi} \langle \chi_A(\xi) \chi_B(0) \rangle_{dBB}, \quad (6.247)$$

where  $\chi_A$  is the inverse Fourier transform associated with  $\chi_{A,k}$ , and  $A, B = 1, 2$ . Through a straightforward implementation of the steps presented in subsection [6.3.5](#), we obtain the correlations among  $\chi_1$  and  $\chi_2$ , having, as a result

$$\langle \chi_A(\xi) \chi_B(0) \rangle_{dBB} = \frac{1}{2\pi} \int_{-\infty}^{\infty} dk e^{ik\xi} \frac{\delta_{AB}}{2|k| \Re[H_{A,k}(\tau)]}. \quad (6.248)$$

This indicates a null crossed correlation, a consequence of the wave functional be a direct product of two independent states (equation [\(6.206\)](#)). The nonzero components of the associated power spectrum are

$$(P_{11})_k(\tau) = \frac{1}{2k \Re[H_{1,k}(\tau)]} = \frac{\cosh\left(\frac{\pi k}{a}\right) + \cos(2k\tau)}{2k \sinh\left(\frac{\pi k}{a}\right)}, \quad (6.249)$$

$$(P_{22})_k(\tau) = \frac{1}{2k \Re[H_{2,k}(\tau)]} = \frac{\cosh\left(\frac{\pi k}{a}\right) - \cos(2k\tau)}{2k \sinh\left(\frac{\pi k}{a}\right)}, \quad (6.250)$$

The expansion in the high temperature regime give us a very simple expression, with

$$(P_{11})_k(\tau) \simeq \frac{2T}{k^2} \cos^2(k\tau), \quad (P_{22})_k(\tau) \simeq \frac{2T}{k^2} \sin^2(k\tau), \quad T \gg 1. \quad (6.251)$$

For low temperatures, on the other hand, we have a constant power spectrum,

$$(P_{11})_k(\tau) \simeq (P_{22})_k(\tau) \simeq \frac{1}{2k}, \quad T \ll 1. \quad (6.252)$$

These findings exhibit a remarkable parallel with the results obtained in the right-wedge scenario, primarily because the wave functional [\(6.206\)](#) behaves like two independent Minkowski ground states. As a matter of fact,  $(P^{11})_k$  and  $(P^{22})_k$  are closely related with the respective classical potential contributions attributable to  $\chi_{1,k}$  and  $\chi_{2,k}$ . Specifically,

$$(P_{11})_k(\tau) = \frac{2}{k^2} \langle V_{1,k} \rangle_{dBB}, \quad (P_{22})_k(\tau) = \frac{2}{k^2} \langle V_{2,k} \rangle_{dBB}, \quad (6.253)$$

where  $V_{1,k} = \frac{1}{2}k^2|\chi_{1,k}|^2$  and  $V_{2,k} = \frac{1}{2}k^2|\chi_{2,k}|^2$ .

The original correlations  $\langle \phi^i(\xi)\phi^j(0) \rangle_{dBB}$  can be expressed in terms of  $\langle \chi_A(\xi)\chi_b(0) \rangle_{dBB}$ , resulting in the following power spectrum

$$(P^{RR})_k(\tau) = (P^{LL})_k(\tau) = \frac{1}{4k} \left( \frac{1}{\Re[H_{1,k}(\tau)]} + \frac{1}{\Re[H_{2,k}(\tau)]} \right) = \frac{\coth\left(\frac{\pi k}{a}\right)}{2k}, \quad (6.254)$$

$$(P^{RL})_k(\tau) = (P^{LR})_k(\tau) = \frac{1}{4k} \left( \frac{1}{\Re[H_{1,k}(\tau)]} - \frac{1}{\Re[H_{2,k}(\tau)]} \right) = \frac{\cos(2k\tau)}{2k \sinh\left(\frac{\pi k}{a}\right)}, \quad (6.255)$$

with the presence of non-null correlations between the right and left modes. Intriguingly, the power spectrum associated with modes in the same side are related to the mean value of the total classical potential,

$$(P^{RR})_k(\tau) = (P^{LL})_k(\tau) = \frac{1}{k^2} \langle V_k \rangle_{dBB}, \quad (6.256)$$

suggesting that such correlations could have a classical nature.

For high-temperature conditions,

$$(P^{RR})_k(\tau) = (P^{LL})_k(\tau) \simeq \frac{T}{k^2}, \quad (P^{RL})_k(\tau) = (P^{LR})_k(\tau) \simeq \frac{T}{k^2} \cos(2k\tau). \quad (6.257)$$

It's worth noting that on the common spacelike hypersurfaces at  $t = \tau = 0$ , the findings derived above align with the power spectrum of a classical field at a finite temperature in Minkowski space, as obtained in references [\[200\]](#), [\[201\]](#).

Conversely, for low accelerations the power spectrum becomes

$$(P^{RR})_k(\tau) = (P^{LL})_k(\tau) \simeq \frac{1}{2k}, \quad (P^{RL})_k(\tau) = (P^{LR})_k(\tau) \simeq 0, \quad (6.258)$$

with negligible correlations between the right and left sides. In such regime, the effect of the horizon is notably weak, in such manner that the correspondent non-local connection between the left and right wedges can be disregarded.

# Chapter 7

## Concluding Remarks

In this second part, we explored the dynamics of a massless scalar field in the context of Rindler spacetime, adopting the de Broglie-Bohm (dBB) framework. Our investigation had the primary goal of comprehending Bohmian aspects related to the Unruh effect. Initially, we focused on the right Rindler wedge, further extending our analysis to include the left side as well. In both scenarios, we derived Hamilton-Jacobi-like equations for the Bohmian fields, along with their corresponding guidance equations. This approach allowed us to recover the well-established results associated with a Bohmian scalar field in the Minkowski vacuum in the context of low accelerations.

By applying dBB methods to scenarios involving arbitrary accelerations, we computed the average energy, deriving the Bose-Einstein distribution with the Unruh temperature as the mean value of the total energy. Since the initial field configuration satisfies the Born rule, the final results obtained through the dBB approach should be identical to that achieved using the standard techniques. So, on the surface, it may seem like there's nothing fundamentally new. However, the dBB approach, utilizing the Hamilton-Jacobi-like equation for the Bohmian fields, provides a different perspective on this phenomenon. It enables the separation of the total mean energy into classical and quantum components, which is not possible with the standard approach. Specifically, the total energy is the sum of a kinetic and a classical potential contributions, together with the quantum potential term.

Inspecting these terms, we observed a periodic interchange between the quantum and classical components as the leading cause of temperature-related effects, more pronounced for large accelerations. To be exact, in the regime where  $a/k \gg 1$ , this alternation between quantum and classical behaviors exhibits sudden, sharp transitions around  $\tau = n\pi/(2k)$ , with  $n$  an integer. It remains uncertain whether these effects can be experimentally observed. It's worth noting that, assuming the Born rule, the statistical predictions of the dBB quantum theory align with those of the conventional approach. However, exploring a quantum phenomenon from an alternative perspective may provide insights into novel experimental consequences that are challenging to discern using the traditional viewpoint

[202]. In our current scenario, the abrupt shifts from classical to quantum dominance do not seem to be mere artifacts of the dBB approach, since they also manifest at the wave functional level (see equations (6.100) and (6.186) for  $a/k \gg 1$ ), suggesting the possibility of experimental observations.

We addressed the guidance equations, leading to the discovery of a rather unique Bohmian field configuration where individual total energy, classical potential, classical kinetic energy, and quantum potential all coincided precisely with their respective mean values, also leading to an effective Unruh temperature. Intriguingly, this configuration also unveiled a time-independent energy with the effective Unruh temperature. So, the presence of the Unruh temperature is not limited to an averaged property of the quantum state, but it is manifest even with an individual field configuration. Additionally, we demonstrate that the Bohmian field in the Rindler space obeys an effective Klein-Gordon equation, with a temperature-dependent effective mass, according to equations (6.145), (6.146), (6.241) and (6.242). Given their resemblance to quantum fields, these equations may offer opportunities for constructing analog models of the Unruh effect.

In our exploration of the complete manifold scenario, we have uncovered the non-local characteristics inherent to the guidance equations governing the Bohmian field modes localized in the right and left wedges (equations (6.199) and (6.200)). It is notable that the behavior of the right (left) mode is influenced by the left (right) mode, despite their spatial separation by a horizon. This analysis may provide valuable insights into comprehending the entanglement between these two field modes and exploring potential ramifications. Such findings may serve as a stepping stone for conducting further analysis within the context of black hole phenomena.

As a final speculative consideration, we have commented that the dBB approach may yield distinct outcomes compared to standard quantum theory under certain circumstances. Particularly, when the distribution of initial field configurations deviates from the Born rule, the dBB approach might exhibit different behaviors before eventually reaching quantum equilibrium. Given the ensemble of field configurations as described in equations (6.148) and (6.243) and considering distributions of the integration constants  $D_{A,k}(a)$  that differ from  $|\Psi_k|^2$  at some initial time, it would be interesting to investigate what kind of particle distribution would emerge, any possible associated temperature, and the time required to reach the quantum equilibrium. In a related context, reference [197] has proposed the possibility of quantum black holes violating the Born rule, potentially affecting the Hawking radiation. The simplified model we have examined here may serve as a point of departure for conducting more precise investigations into this intriguing prospect.

# Bibliography

- [1] M. M. A. Paixão and H. S. Lima *Numerical validation of Ehrenfest theorem in a Bohmian perspective for non-conservative systems*. Eur. Phys. J. Plus 138, 549 (2023)
- [2] M. M. A. Paixão and H. S. Lima, Wolfram Community, *Numerical validation of Ehrenfest theorem in a Bohmian perspective for non-conservative systems*, 2023, available at: <https://community.wolfram.com/groups/-/m/t/2954181>.
- [3] H. S. Lima, M. M. A. Paixão, and C. Tsallis, *de Broglie-Bohm analysis of a nonlinear membrane: From quantum to classical chaos*, arXiv:2308.07178 [quant-ph], submitted for publication.
- [4] M. M. A. Paixão, O. Galkina, and N. Pinto-Neto, *Unruh effect under the de Broglie-Bohm perspective*. Phys. Rev. D 108, 083514 (2023)
- [5] M. M. A. Paixão and O. Piguet, *Five dimensional Chern-Simons gravity for the expanded (anti)-de Sitter gauge group  $C_5$* , Eur. Phys. J. C 80, 138 (2020).
- [6] L. de Broglie, *Interference and Corpuscular Light*. Nature 118, 441 (1926).
- [7] D. Bohm, *A Suggested Interpretation of the Quantum Theory in Terms of "Hidden" Variables. I*. Phys. Rev. 85, 166 (1952).
- [8] D. Bohm, *A Suggested Interpretation of the Quantum Theory in Terms of "Hidden" Variables. II*. Phys. Rev. 85, 180 (1952).
- [9] A. C. Tzemos and G. Contopoulos, *Chaos and ergodicity in an entangled two-qubit Bohmian system*, Phys. Scr. 95, 065225 (2020).
- [10] A. C. Tzemos and G. Contopoulos, *Chaos and ergodicity in entangled non-ideal Bohmian qubits*, Chaos Solit. Fractals. 156, 111827 (2022).
- [11] C. Efthymiopoulos and G. Contopoulos, *Chaos in Bohmian quantum mechanics*, J. Phys. A: Math. Gen. 39, 1819 (2006).
- [12] Tzemos, A.C.; Contopoulos, G. *Bohmian quantum potential and chaos*, Chaos Solit. Fractals. 160, 112151 (2022).

- [13] A. Ivanov, et al, *Quantum chaos in strong field ionization of hydrogen*, J. Phys. B: At. Mol. Opt. Phys. 52, 225002 (2019).
- [14] W. Li, *Analyzing quantum synchronization through Bohmian trajectories*, Phys. Rev. A 106, 023512 (2022).
- [15] A. C. Tzemos, G. Contopoulos, *Born's rule in multiqubit Bohmian systems*, Chaos Solit. Fractals. 164, 112650 (2022).
- [16] M. Bonilla-Licea and D. Schuch, *Quantum hydrodynamics with complex quantities*, Phys. Lett. A 392, 127171 (2021).
- [17] M. Bonilla-Licea, D. Schuch, and M. B. Estrada, *Diffusion Effect in Quantum Hydrodynamics*, Axioms 11, 552 (2022).
- [18] M. Bonilla-Licea and D. Schuch *Uncertainty Relations in the Madelung Picture*. Entropy 24, 20 (2022).
- [19] F. Avanzini and G. J. Moro, *Quantum Stochastic Trajectories: The Fokker-Planck-Bohm Equation Driven by the Reduced Density Matrix*, J. Phys. Chem. A 122, 2751 (2018).
- [20] R. Sawada, T. Sato, and K. L. Ishikawa, *Analysis of strong-field enhanced ionization of molecules using Bohmian trajectories*, Phys. Rev. A 90, 023404 (2014).
- [21] E. Schrödinger *An Undulatory Theory of the Mechanics of Atoms and Molecules*, Phys. Rev. 28, 1049 (1926).
- [22] Ehrenfest, P. *Bemerkung über die angenäherte Gültigkeit der klassischen Mechanik innerhalb der Quantenmechanik*, Zeitschrift für Physik. 45, 455 (1927).
- [23] W. R. Hamilton, *On a General Method of Expressing the Paths of Light, & of the Planets, by the Coefficients of a Characteristic Function* (PD Hardy, 1833).
- [24] W. R. Hamilton *On the application to dynamics of a general mathematical method previously applied to optics*, British Association Report 513, (1834).
- [25] C. G. J. Jacobi *C.G.J. Jacobi's Vorlesungen über Dynamik* (G. Reimer, Berlin, 1884)
- [26] L. Landau and E. Lifshitz, *The Classical Theory of Fields* (Addison-Wesley, Reading, MA, 2002).
- [27] V. I. Arnold, *Mathematical Methods of Classical Mechanics - 2nd ed* (Springer, New York, 2002).

- [28] H. Goldstein, C. Poole, and J. Safko, *Classical Mechanics. 3rd ed* (Addison-Wesley, Reading, MA, 1989).
- [29] N. A. Lemos, *Mecânica analítica - 2nd ed* (Livraria da Física, São Paulo, 2007).
- [30] A. Valentini, *Signal-locality, uncertainty, and the subquantum H-theorem. I* , Phys. Lett. A 156, 5 (1991).
- [31] D. Bohm and B. J. Hiley, *The undivided universe: an ontological interpretation of quantum theory* (Routledge, London, 1993).
- [32] P. R. Holland, *The quantum theory of motion: An Account of the de Broglie-Bohm Interpretation of Quantum Mechanics* (Cambridge University Press, Cambridge, 1993).
- [33] J. von Neumann, *Mathematical Foundations of Quantum Mechanics* (Princeton University Press, Princeton, 1955).
- [34] B. S. DeWitt, *Quantum mechanics and reality* , Phys. Today 23, 30 (1970).
- [35] H. D. Zeh, *On the interpretation of measurement in quantum theory*, Found. Phys. 1, 69 (1970).
- [36] W. H. Zurek, *Pointer basis of quantum apparatus: Into what mixture does the wave packet collapse?* , Phys. Rev. D 24, 1516 (1981).
- [37] W. H. Zurek, *Decoherence and the transition from quantum to classical* , Phys. Rev. D 26, 1862 (1982).
- [38] W. H. Zurek, *Decoherence and the transition from quantum to classical* , Phys. Today 44, 36 (1991).
- [39] N. Pinto-Neto, *Teorias e interpretações da mecânica quântica* (Livraria da Física, São Paulo, 2010).
- [40] W. E. Schiesser, *The numerical method of lines: integration of partial differential equations* (Elsevier, 2012).
- [41] Wolfram Research, Inc., *Mathematica, Version 13.2*, Champaign, IL, 2022, <https://reference.wolfram.com/language/tutorial/NDSolveMethodOfLines.html>.
- [42] D. Griffiths and D. Schroeter *Introduction to Quantum Mechanics 3rd ed.* (Cambridge University Press, Cambridge, 2018).
- [43] C. Cohen-Tannoudji, B. Diu, F. Laloë, and S. R. Hemley, *Quantum mechanics* (Wiley, New York, 1977).

- [44] J. J. Sakurai, *Modern quantum mechanics rev. ed.* (Addison-Wesley, Reading MA, 1994).
- [45] B. C. Hall, *Quantum Theory for Mathematicians* (Springer-Verlag, New York, 2013).
- [46] D. Vitali, S. Mancini, and P. Tombesi, *Optomechanical scheme for the detection of weak impulsive forces*, Phys. Rev. A 64, 051401(R) (2001).
- [47] J. S. Bennett and W. P. Bowen, *Rapid mechanical squeezing with pulsed optomechanics*, New J. Phys. 20, 113016 (2018).
- [48] D. F. Coker and L. Xiao, *Methods for molecular dynamics with nonadiabatic transitions*, J. Chem. Phys. 102, 496 (1995).
- [49] Z. Huang and M. Sarovar, *Smoothing of Gaussian quantum dynamics for force detection*, Phys. Rev. A 97, 042106 (2018).
- [50] S. Fishman, I. Guarneri, and L. Rebuzzini, *Stable Quantum Resonances in Atom Optics* Phys. Rev. Lett. 89, 084101 (2002).
- [51] V. V. Egorov, *Quantum–Classical Mechanics: Nano-Resonance in Polymethine Dyes*, Mathematics 10, 1443 (2022).
- [52] S. Duque, P. Brumer, and L. A. Pachón, *Classical Approach to Multichromophoric Resonance Energy Transfer*, Phys. Rev. Lett. 115, 110402 (2015).
- [53] A. J. Silenko, *General classical and quantum-mechanical description of magnetic resonance: an application to electric-dipole-moment experiments*, Eur. Phys. J. C 77, 341 (2017).
- [54] I. Dana, V. Ramareddy, I. Talukdar, and G. S. Summy, *Experimental Realization of Quantum-Resonance Ratchets at Arbitrary Quasimomenta*, Phys. Rev. Lett. 100, 024103 (2008).
- [55] G. Duffing, *Erzwungene Schwingung bei veränderlicher Eigenfrequenz und ihre technische Bedeutung*, Vieweg, Braunschweig (1918).
- [56] H. J. Korsch, H. Jodl, and T. Hartmann, *Chaos: A Program Collection for the PC*, Springer, Berlin (2008).
- [57] R. Zivieri, S. Vergura, and M. Carpentieri, *Analytical and numerical solution to the nonlinear cubic Duffing equation: An application to electrical signal analysis of distribution lines*, Am. J. Phys. 40, 9152 (2016).
- [58] B. K. Jones and G. Trefan, *The Duffing oscillator: A precise electronic analog chaos demonstrator for the undergraduate laboratory*, Appl. Math. Model. 69, 464 (2001).

- [59] N. Q. Hu, and X. S. Wen, *The application of Duffing oscillator in characteristic signal detection of early fault*, J. Sound Vib. 268, 917 (2003).
- [60] S. Novak and R. G. Frehlich, *Transition to chaos in the Duffing oscillator*, Phys. Rev. A 26, 3660 (1982).
- [61] S. Wiggins, *Chaos in the quasiperiodically forced Duffing oscillator*, Phys. Lett. A 124, 138 (1987).
- [62] Y. Ueda, *Survey of regular and chaotic phenomena in the forced Duffing oscillator*, Chaos Solit. Fractals 1, 199 (1991).
- [63] W. Y. Liu, W. Q. Zhu, and Z. L. Huang, *Effect of bounded noise on chaotic motion of duffing oscillator under parametric excitation*, Chaos Solit. Fractals 12, 527 (2001).
- [64] H. G. E. Kadji, J. B. C. Orou, R. Yamapi, and P. Wofo, *Nonlinear dynamics and strange attractors in the biological system*, Chaos Solit. Fractals 32, 862 (2007).
- [65] M. Laurent, J. Deschatrette, C. M. Wolfrom, *Unmasking chaotic attributes in time series of living cell populations*, PLoS One 5, e9346 (2010).
- [66] S. K. Behera, R. A. Ranjan, D. Kumar, and S. Sarangi, and R. Bhattacharyya, *Dynamic modelling and analysis of a biological circular membrane*, Int. J. Eng. Sci. 188, 103864 (2023).
- [67] E. Ott, *Dynamical Systems and Chaos* (Cambridge University Press, Cambridge, 2002)
- [68] H. Broer and F. Takens, *Chaos in Dynamical Systems* (Springer, New York, 2011).
- [69] S. H. Strogatz, *Nonlinear Dynamics and Chaos: With Applications to Physics, Biology, Chemistry, and Engineering (Studies in Nonlinearity)* (CRC Press, 2018).
- [70] P. Holmes, *Poincaré, celestial mechanics, dynamical-systems theory and “chaos”*, Phys. Rep. 193, 137 (1990).
- [71] G. Contopoulos, *Order and chaos in dynamical astronomy* (Springer, Berlin, 2002).
- [72] G. J. Sussman and J. Wisdom, *Chaotic evolution of the solar system*, Science 257, 56 (1992).
- [73] M. Lecar, F. A. Franklin, M. J. Holman, and N. W. Murray, *Chaos in the Solar System*, Annu. Rev. Astron. Astrophys. 39, 581 (2001).
- [74] J. M. Ottino, *Mixing, chaotic advection, and turbulence*, Annu. Rev. Fluid Mech. 22, 207 (1990).

- [75] T. M Schneider, B. Eckhardt, and J. A. Yorke, *Turbulence transition and the edge of chaos in pipe flow*, Phys. Rev. Lett. 99, 034502 (2007).
- [76] N. Fournier, M. Hauray, and S. Mischler, *Propagation of chaos for the 2D viscous vortex model*, J. Eur. Math. Soc. 16, 1423 (2014).
- [77] K. Ikeda, H. Daido, and O. Akimoto, *Optical turbulence: chaotic behavior of transmitted light from a ring cavity*, Phys. Rev. Lett. 45, 709 (1980).
- [78] J. Liu, H. Chen, and S. Tang, *Synchronized chaotic optical communications at high bit rates*, IEEE J. Quantum Electron. 38, 1184 (2002).
- [79] J. Chen and P. J. Palmadesso, *Chaos and nonlinear dynamics of single-particle orbits in a magnetotaillike magnetic field*, J. Geophys. Res. Space Phys. 91, 1499 (1986).
- [80] T. Klinger et al., *Chaos control and taming of turbulence in plasma devices*, Phys. Plasmas 8, 1961 (2001).
- [81] C. Tsallis, *Possible generalization of Boltzmann-Gibbs statistics*, J. Stat. Phys. 52, 479 (1988)
- [82] Y. S. Weinstein, S. Lloyd, and C. Tsallis, *Border between regular and chaotic quantum dynamics*, Phys. Rev. Lett. 89, 214101 (2002)
- [83] Y. S. Weinstein, S. Lloyd, and C. Tsallis, *On the emergence of nonextensivity at the edge of quantum chaos*, In: H. T. Elze (eds), *Decoherence and Entropy in Complex Systems. Lecture Notes in Physics* (Springer, Berlin, Heidelberg, 2004)
- [84] A. Peres, *Stability of quantum motion in chaotic and regular systems*. Phys. Rev. A 30, 1610-1615 (1984).
- [85] F. M. Izrailev, *Simple models of quantum chaos: Spectrum and eigenfunctions*. Phys. Rep. 196, 299 (1990).
- [86] M. C. Gutzwiller, *Chaos in Classical and Quantum Mechanics*. (Springer-Verlag, New York, 1990).
- [87] K. Nakamura, *Quantum chaos: a new paradigm of nonlinear dynamics*. (Cambridge University Press, Cambridge, 1994).
- [88] H. Stöckmann, *Quantum chaos: an introduction*. (American Association of Physics Teachers, 2000).
- [89] S. Wimberger, *Nonlinear dynamics and quantum chaos*. (Springer, Cham, 2014).

- [90] O. Bohigas and H. A. Weidenmüller *Aspects of chaos in nuclear physics*, Annu. Rev. Nucl. Sci., 38, 421-453 (1988).
- [91] G. E. Mitchell, A. Richter, and H. A. Weidenmüller *Random matrices and chaos in nuclear physics: Nuclear reactions*, Rev. Mod. Phys., 82, 2845-2901 (2010).
- [92] S. Lüscher, T. Heinzl, K. Ensslin, W. Wegscheider and M. Bichler *Signatures of Spin Pairing in Chaotic Quantum Dots*, Phys. Rev. Lett., 86, 2118–2121 (2001).
- [93] L. A. Ponomarenko et al. *Chaotic Dirac billiard in graphene quantum dots*, Science, 320, 356-358 (2008).
- [94] B. Georgeot and D. L. Shepelyansky *Quantum chaos border for quantum computing*, Phys. Rev. E, 62, 3504 (2000).
- [95] D. L. Shepelyansky *Quantum chaos and quantum computers*, Phys. Scr., 2001, 112 (2001).
- [96] B. Georgeot and D. L. Shepelyansky *Exponential gain in quantum computing of quantum chaos and localization*, Phys. Rev. Lett., 86, 2890–2893 (2001).
- [97] T. Prosen and M. Znidaric *Can quantum chaos enhance the stability of quantum computation?*, J. Phys. A Math. Gen., 34, L681 (2001).
- [98] J. M. Magan *Black holes, complexity and quantum chaos*, J. High Energy Phys., 2018, 1-34 (2018).
- [99] A. Valentini, *Signal-locality, uncertainty, and the subquantum H-theorem. I*, Phys. Lett. A, 156(1–2),5-11 (1991).
- [100] A. Valentini, *Signal-locality, uncertainty, and the subquantum H-theorem. II*, Phys. Lett. A, 158(1–2),1-8 (1991).
- [101] A. C. Tzemos and G. Contopoulos, *The role of chaotic and ordered trajectories in establishing Born's rule*, Phys. Scr., 96, 065209 (2021).
- [102] P. Šeba, *Quantum chaos in optical systems: The annular billiard*, Phys. Rev. Lett. 64, 1855 (1990).
- [103] M. Hentschel and K. Richter, *Wave chaos in singular quantum billiard*, Phys. Rev. E 66, 056207 (2002).
- [104] R. Crook et al., *Imaging fractal conductance fluctuations and scarred wave functions in a quantum billiard*, Phys. Rev. Lett. 91, 246803 (2003).

- [105] Y. H. Kim, M. Barth, H. J. Stöckmann, and J. P. Bird , *Wave function scarring in open quantum dots: A microwave-billiard analog study*. Phys. Rev. B 65, 165317 (2002).
- [106] K. Nakamura and T. Harayama, *Quantum chaos and quantum dots*. (Oxford University Press, New York, 2004).
- [107] F. Haake, *Quantum Signatures of Chaos*. (Springer-Verlag, Berlin, 2001).
- [108] R. Jensen, *Quantum chaos*, Nature 355, 311 (1992).
- [109] M. C. Gutzwiller, *Periodic orbits and classical quantization conditions*, J. Math. Phys. 12, 343 (1971).
- [110] E. P. Gross, *Structure of a quantized vortex in boson systems*, Nuovo Cim. 20, 454 (1961).
- [111] L. P. Pitaevskii, *Vortex lines in an imperfect Bose gas*, Sov. Phys. JETP. 13, 451 (1961).
- [112] D. T. Mihailovic, G. Mimic and I. Arsenic *The chaos and complexity in climate models*, Adv. Meteorol., 2014, 878249 (2014).
- [113] C. Ma, S. Meyers and B. Sageman, *Theory of chaotic orbital variations confirmed by Cretaceous geological evidence*, Nature, 542, 468–470 (2017).
- [114] S. Bo-Wen, et al. *Is weather chaotic?: Coexistence of chaos and order within a generalized lorenz model*, BAMS, 102, E148-E158 (2021).
- [115] D. Dürr, S. Goldstein, and N. Zanghi, *Quantum chaos, classical randomness, and Bohmian mechanics*, J. Stat. Phys., 68, 259 (1992).
- [116] G. Iacomelli and M. Pettini, *Regular and chaotic quantum motions*, Phys. Lett. A 212, 29 (1996).
- [117] S. Sengupta and P. K. Chattaraj, *The quantum theory of motion and signatures of chaos in the quantum behaviour of a classically chaotic system*, Phys. Lett. A 215, 119 (1996).
- [118] H. Wu and D. W. L. Sprung, *Quantum chaos in terms of Bohm trajectories*, Phys. Lett. A 261, 150 (1999).
- [119] J. T. Cushing and G. E. Bowman *Bohmian mechanics and chaos* (Cambridge University Press, Cambridge, 1999).
- [120] J. T. Cushing, *Bohmian insights into quantum chaos*, Philos. Sci. 67, S430 (2000).

- [121] G. Contopoulos and C. Efthymiopoulos, *Ordered and chaotic Bohmian trajectories*, Celest. Mech. Dyn. Astr. 102, 219 (2008).
- [122] G. Contopoulos and A. C. Tzemos, *Chaos in Bohmian quantum mechanics: A short review*, Regul. Chaotic Dyn. 25, 476 (2020).
- [123] R. H. Parmenter and R. W. Valentine, *Deterministic chaos and the causal interpretation of quantum mechanics*, Phys. Lett. A 201, 1 (1995).
- [124] F. H. M. Faisal and U. Schwengelbeck, *Unified theory of Lyapunov exponents and a positive example of deterministic quantum chaos*, Phys. Lett. A 207, 31 (1995).
- [125] G. G. de Polavieja, *Exponential divergence of neighboring quantal trajectories*, Phys. Rev. A 53, 2059 (1996).
- [126] F. Borondo, A. Luque, J. Villanueva, and D. A. Wisniacki, *A dynamical systems approach to Bohmian trajectories in a 2D harmonic oscillator*, J. Phys. A Math. Theor. 42, 495103 (2009).
- [127] S. Sengupta, M. Khatua and P.K. Chattaraj, *Bohmian trajectory from the "classical" Schrödinger equation*, Chaos 24, 043123 (2014).
- [128] A. C. Tzemos, G. Contopoulos, and C. Efthymiopoulos, *Bohmian trajectories in an entangled two-qubit system*, Phys. Scr. 94, 105218 (2019).
- [129] A. C. Tzemos and G. Contopoulos, *Ergodicity and Born's rule in an entangled two-qubit Bohmian system*, Phys. Rev. E **102**, 042205 (2020).
- [130] P. A. M. Dirac, *Quantised singularities in the electromagnetic field*, Proc. R. Soc. Lond. A 133, 60 (1931).
- [131] I. Bialynicki-Birula and Z. Bialynicka-Birula, *Magnetic monopoles in the hydrodynamic formulation of quantum mechanics*, Phys. Rev. D 3, 2410 (1971).
- [132] I. Bialynicki-Birula, Z. Bialynicka-Birula, and C. 'Sliwa, *Motion of vortex lines in quantum mechanics*, Phys. Rev. A 61, 032110 (2000).
- [133] D. A. Wisniacki and E. R. Pujals, *Motion of vortices implies chaos in Bohmian mechanics*, Europhys. Lett. 71, 159 (2005).
- [134] D. A. Wisniacki, E. R. Pujals, and F. Borondo, *Vortex interaction, chaos and quantum probabilities*, Europhys. Lett. 73, 671 (2006).
- [135] D. A. Wisniacki, E. R. Pujals and F. Borondo, *Vortex dynamics and their interactions in quantum trajectories*, J. Phys. A Math. Theor. 40, 14353 (2007).

- [136] A. Cesa, J. Martin, and W. Struyve, *Chaotic Bohmian trajectories for stationary states*, J. Phys. A: Math. Theor. 49, 395301 (2016).
- [137] H. Frisk, *Properties of the trajectories in Bohmian mechanics*, Phys. Lett. A 227, 139 (1997).
- [138] A. Valentini and H. Westman, *Dynamical origin of quantum probabilities*, Proc. R. Soc. A 461, 253 (2005).
- [139] C. Efthymiopoulos and G. Contopoulos, *Chaos in Bohmian quantum mechanics*, J. Phys. A: Math. Gen. 39, 1819 (2006).
- [140] P. Falsaperla and G. Fonte, *On the motion of a single particle near a nodal line in the de Broglie-Bohm interpretation of quantum mechanics*, Phys. Lett. A 316, 382 (2003).
- [141] C. Efthymiopoulos, C. Kalapotharakos, and G. Contopoulos, *Nodal points and the transition from ordered to chaotic Bohmian trajectories*, J. Phys. A: Math. Theor. 40, 12945 (2007).
- [142] C. Efthymiopoulos, C. Kalapotharakos, and G. Contopoulos, *Origin of chaos near critical points of quantum flow*, Phys. Rev. E 79, 036203 (2009).
- [143] A. C. Tzemos, G. Contopoulos, and C. Efthymiopoulos, *Origin of chaos in 3-d Bohmian trajectories*, Phys. Lett. A 380, 3796 (2016).
- [144] A. C. Tzemos, C. Efthymiopoulos, and G. Contopoulos, *Origin of chaos near three-dimensional quantum vortices: A general Bohmian theory*, Phys. Rev. E 97, 042201 (2018).
- [145] S. Konkel and A. J. Makowski, *Regular and chaotic causal trajectories for the Bohm potential in a restricted space*, Phys. Lett. A 238, 95 (1998).
- [146] T. J. Ypma *Historical development of the Newton-Raphson method*, SIAM Rev. 37, 531 (1995).
- [147] Wolfram Research, Inc., *Mathematica, Version 13.2*, Champaign, IL, 2022, <https://reference.wolfram.com/language/ref/FindRoot.html>.
- [148] Wolfram Research, Inc., *Mathematica, Version 13.2*, Champaign, IL, 2022, <https://reference.wolfram.com/language/tutorial/UnconstrainedOptimizationMethodsForSolvingNonlinearEquations.html>.
- [149] H. Poincaré, *Les méthodes nouvelles de la mécanique céleste: Méthodes de MM. Newcomb, Gylden, Linstadt et Bohlin Vol. 2.* (Gauthier-Villars et fils, imprimeurs-libraires, 1893).

- [150] A. A. Andronov and A. Witt, *Sur la théorie mathématique des auto-oscillations*, CR Acad. Sci. Paris 190, 256 (1930).
- [151] E. Hopf, *Abzweigung einer periodischen Lösung von einer stationären Lösung eines Differentialsystems.*, Ber. Math.-Phys. Kl Sächs. Akad. Wiss. Leipzig 94, 1 (1942).
- [152] J. E. Marsden and M. McCracken, *The Hopf bifurcation and its applications* (Springer Science & Business Media, 2012).
- [153] G. Benettin, L. Galgani, and J. M. Strelcyn, *Kolmogorov entropy and numerical experiments*, Phys. Rev. A 14, 2338 (1976).
- [154] G. Benettin, L. Galgani, A. Giorgilli, and J. M. Strelcyn, *Lyapunov characteristic exponents for smooth dynamical systems and for Hamiltonian systems; a method for computing all of them. Part 1: Theory*, Meccanica 15, 9 (1980).
- [155] C. Runge, *Über die numerische Auflösung von Differentialgleichungen*, Math. Ann., 46, 167-178 (1895).
- [156] W. Kutta, *Beitrag zur näherungsweise Integration totaler Differentialgleichungen*, Z. Math. Phys., 46, 435-453 (1901).
- [157] Wolfram Research, Inc., *Mathematica, Version 13.2*, Champaign, IL, 2022, <https://reference.wolfram.com/language/tutorial/NDSolveExplicitRungeKutta.html>.
- [158] K. Bathe, "Finite Element Method," in *Wiley Encyclopedia of Computer Science and Engineering*, (John Wiley & Sons, 2008)
- [159] Wolfram Research, Inc., *Mathematica, Version 13.2*, Champaign, IL, 2022, <https://reference.wolfram.com/language/FEMDocumentation/tutorial/FiniteElementOverview.html>.
- [160] Wolfram Research, Inc., *Mathematica, Version 13.2*, Champaign, IL, 2022, <https://reference.wolfram.com/language/FEMDocumentation/tutorial/FiniteElementBestPractice.html>
- [161] H. A. Van der Vorst, *Bi-CGSTAB: A fast and smoothly converging variant of Bi-CG for the solution of nonsymmetric linear systems*, SIAM J. Sci. Statist. Comput. 13, 631 (1992)
- [162] H. A. Van der Vorst, *Iterative Krylov methods for large linear systems*, (Cambridge University Press, Cambridge, 2003)

- [163] S. A. Fulling, *Nonuniqueness of Canonical Field Quantization in Riemannian Space-Time*. Phys. Rev. D 7, 2850 (1973).
- [164] P. C. W. Davies, *Scalar production in Schwarzschild and Rindler metrics*. J. Phys. A 8, 609 (1975).
- [165] W. G. Unruh, *Notes on black-hole evaporation*. Phys. Rev. D 14, 870 (1976).
- [166] S. W. Hawking, *Black hole explosions?*. Nature 248, 30 (1974).
- [167] S. W. Hawking, *Particle Creation by black-holes*. Commun. Math. Phys. 43, 199 (1975).
- [168] M. Horibe, *Thermal Radiation of Fermions by an Accelerated Wall*. Prog. Theor. Phys. 61, 661 (1979).
- [169] D. Roy, *The Unruh thermal spectrum through scalar and fermion tunneling*. Phys. Lett. B 681, 185 (2009).
- [170] H. C. Rosu, *On the estimates to Measure Hawking Effect and Unruh Effect in the Laboratory*. Int. J. Mod. Phys. D 03, 545 (1994).
- [171] J. Hu, L. Feng, Z. Zhang, et al. *Quantum simulation of Unruh radiation*. Nat. Phys. 15, 785 (2019).
- [172] E. T. Akhmedov and D. Singleton, *On the physical meaning of the Unruh effect*. JETP Letters 86, 615 (2008).
- [173] E. M. Martínez, I. Fuentes, and R. B. Mann, *Using Berry's Phase to Detect the Unruh Effect at Lower Accelerations*. Phys. Rev. Lett. 107, 131301 (2011).
- [174] C. Gooding, S. Biermann, S. Erne, J. Louko, W. G. Unruh, J. Schmiedmayer, and S. Weinfurtner, *Interferometric Unruh Detectors for Bose-Einstein Condensates*. Phys Rev Lett. 125, 213603 (2020).
- [175] V. I. Kolobov, K. Golubkov, J. R. Muñoz de Nova, and J. Steinhauer, *Observation of stationary spontaneous Hawking radiation and the time evolution of an analogue black hole*. Nat. Phys. 17, 362 (2021).
- [176] J. R. Muñoz de Nova, K. Golubkov, V. I. Kolobov, and J. Steinhauer, *Observation of thermal Hawking radiation and its temperature in an analogue black hole*. Nature 569, 688 (2019).
- [177] J. Steinhauer, *Observation of quantum Hawking radiation and its entanglement in an analogue black hole*. Nature Phys. 12, 959 (2016).

- [178] R. Balbinot, A. Fabbri, S. Fagnocchi, A. Recati, and I. Carusott, *Nonlocal density correlations as a signature of Hawking radiation from acoustic black holes*. Phys. Rev. A 78, 021603(R) (2008).
- [179] F. Belgiorno, S. L. Cacciatori, M. Clerici, V. Gorini, G. Ortenzi, L. Rizzi, E. Rubino, V. G. Sala, and D. Faccio *Hawking Radiation from Ultrashort Laser Pulse Filaments*. Phys. Rev. Lett. 105, 203901 (2010).
- [180] Mera, G. *A review on the Unruh Effect and the Thermofield-double state*. arXiv-hep-th: 2001.09869v1.
- [181] Crispino, L. C. B.; Higuchi, A.; Matsas, G. E. A. *The Unruh effect and its applications*. Rev. Mod. Phys. 2008, 80, 787–838.
- [182] Frodden, E.; Valdés, N. *Unruh Effect: Introductory notes to quantum effects for accelerated observers*. Int. J. Mod. Phys. A 2018, 33, 1830026.
- [183] W. G. Unruh and R. M. Wald, *What happens when an accelerating observer detects a Rindler particle*, Phys. Rev. D **29**, 1047 (1984).
- [184] Struyve, W. *Pilot-wave approaches to quantum field theory*. J. Phys. Conf. Ser. 2011, 306, 012047.
- [185] Duerr, D.; Goldstein, S.; Tumulka, R.; Zanghi, N. *Bohmian mechanics and quantum field theory*. J. Phys. A 2005, 38 R1.
- [186] Hatfield, B., *Quantum Field Theory of Point Particles and Strings* (Frontier in Physics)(Addison-Wesley Publishing Company, Redwood City, California,1992).
- [187] Bohm, D.; Hiley, B. J.; Kaloyerou, P.N *An ontological basis for the quantum theory*. Phys. Rep. 1987, 144, 321-375;
- [188] Bohm, D.; Hiley, B. J.; Kaloyerou, P.N. *An ontological basis for the quantum theory Pt 2.* Phys. Rep. 1987, 144, 349-375;
- [189] Kaloyerou, P.N. *The causal interpretation of the electromagnetic field*. Phys. Rep. 1994, 244, 287;
- [190] Kaloyerou, P.N. *The causal interpretation of quantum fields and the vacuum*. Found. Phys. Lett. 2000, 13, 41–54;
- [191] Freese, K.; Hill, C.T.; Mueller, M. *Covariant Functional Schrödinger Formalism and Application to the Hawking Effect*. Nucl.Phys.B 1985, 255, 693-716.
- [192] Rindler, W. *Hyperbolic Motion in Curved Space Time*, Phys. Rev. 1960, 119, 2082.

- [193] Rindler, W. *Kruskal Space and the Uniformly Accelerated Frame*, American Journal of Physics 1966, 34, 1174.
- [194] N. N. Bogoliubov, *On a new method in the theory of superconductivity*. Nuovo Cim. 7, 794 (1958);
- [195] J. G. Valatin, *Comments on the theory of superconductivity*. Nuovo Cim. 7, 843 (1958);
- [196] N. Pinto-Neto, G. Santos, and W. Struyve, *Quantum-to-classical transition of primordial cosmological perturbations in de Broglie–Bohm quantum theory* Phys. Rev. D 85, 083506 (2012).
- [197] A. Valentini, *Beyond the Born rule in quantum gravity*, Found. Phys. **53**, 6 (2023).
- [198] Unruh, W. G.; Wald, R. M.; *What happens when an accelerating observer detects a Rindler particle* Phys. Rev. D 1984, 29, 1047-1056.
- [199] C. Kiefer, *Hawking radiation from decoherence*, Class. Quantum Gravity **18**, L151 (2001).
- [200] Aarts, G.; Smit, J. *Classical approximation for time dependent quantum field theory: Diagrammatic analysis for hot scalar fields*. Nucl.Phys.B 1998, 511, 451-478.
- [201] Aarts, G. The Classical approximation for real time scalar field theory at finite temperature. Contribution to 5th International Workshop on Thermal Field Theories and Their Applications. hep-ph/9809339.
- [202] X. Oriols and J. Mompart, *Applied Bohmian Mechanics: from Nanoscale Systems to Cosmology* (Singapore: PanStanford Publishing, 2019)
- [203] R. Omnès, *The Interpretation of Quantum Mechanics* (Princeton University Press: Princeton, NJ, USA, 1994).
- [204] N. Pinto-Neto *The de Broglie-Bohm Quantum Theory and Its Applications to Quantum Cosmology*. Universe 7, 134 (2021).
- [205] N. Pinto-Neto and J. C. Fabris, *Quantum cosmology from the de Broglie-Bohm perspective*. Class. Quant. Grav. 30, 143001 (2013).
- [206] J. A. Barros, N. Pinto-Neto, and M. A. Sagiolo-Leal, *The causal interpretation of dust and radiation fluid non-singular quantum cosmologies*, Phys. Lett. A 241, 229 (1998).
- [207] N. Pinto-Neto, *Bouncing Quantum Cosmology* Universe 241, 110 (2021).

- [208] D. Dürr and S. Teufel, *Bohmian Mechanics* ( Springer: Berlin, Germany, 2009).
- [209] S. Colin and A. Valentini, *Primordial quantum nonequilibrium and large-scale cosmic anomalies*. Phys. Rev. D 2015, 92, 043520.